Cluster Model Analysis of Exotic Decay in Actinide Nuclei

by

Erasmus Johannes du Toit

Thesis presented in partial fulfilment of the requirements for the degree of Master of Science in Physics in the Faculty of Science at Stellenbosch University

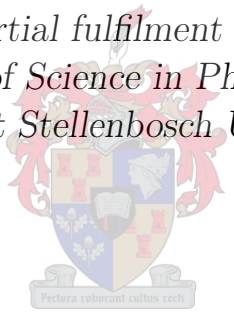

Department of Physics,
University of Stellenbosch,
Private Bag X1, Matieland 7602, South Africa.

Supervisors:

Prof. S.M. Wyngaardt
Prof. S.M. Perez

December 2014

Declaration

By submitting this thesis electronically, I declare that the entirety of the work contained therein is my own, original work, that I am the sole author thereof (save to the extent explicitly otherwise stated), that reproduction and publication thereof by Stellenbosch University will not infringe any third party rights and that I have not previously in its entirety or in part submitted it for obtaining any qualification.

Signature: .....
E.J. du Toit

Date: December 2014 .....

Abstract

Cluster Model Analysis of Exotic Decay in Actinide Nuclei

E.J. du Toit

Department of Physics,
University of Stellenbosch,
Private Bag X1, Matieland 7602, South Africa.

Thesis: MSc (Physics)

December 2014

The binary cluster model is used to investigate the properties of exotic structures and decays in various nuclei. A simple method is described to choose the possible clusters forming within the nucleus, by assuming the nucleus consists of a mixture of up to four different core-cluster pairs. A phenomenological potential is then used, with optimized parameters, to describe the even-even $^{222-232}Th$ nuclei within the binary cluster model, by calculating exotic decay half-lives, reduced electromagnetic transition probabilities, and energy spectra. After finding that all experimentally observed heavy ion emissions are predicted with the model and calculated structure observables are reproduced within good agreement of the experimentally measured values, the model was extended to include the even-even $^{230-234}U$, $^{236-240}Pu$ and $^{222-224}Ra$ nuclei. We found that almost all experimentally observed heavy ion emissions are predicted within the model with reasonable accuracy in the calculated half-lives, and found good agreement in the other calculated structure observables.

Uittreksel

Bondel Model Analise van Eksotiese Verval in Aktinied Nuklides

("Cluster Model Analysis of Exotic Decay in Actinide Nuclei")

E.J. du Toit

Departement Fisika,
Universiteit van Stellenbosch,
Privaatsak X1, Matieland 7602, Suid Afrika.

Tesis: MSc (Fisika)

Desember 2014

Die binêre bondel model is gebruik om die eienskappe van eksotiese strukture en verval in verskeie nukliedes te ondersoek. 'n Eenvoudige metode is gebruik om die moontlike bondels wat binne die nuklied vorm te kies, deur die aanname te maak dat die nuklied uit 'n mengsel van tot vier verskillende kern-bondel pare bestaan. 'n Fenomenologiese potensiaal is dan gebruik, met optimale parameters, om die ewe-ewe $^{222-232}Th$ nukliedes met die binêre bondel model te beskryf, deur eksotiese verval halfleeftye, verminderde elektromagnetiese oorgangswaarskynlikhede, en energie spektra te bereken. Nadat daar gevind is dat alle vrygestelde swaar ione wat eksperimenteel waargeneem is deur die model voorspel word, en berekende struktuur waarneembares tot goeie ooreenstemming met die eksperimentele waardes produseer is, is die model uitgebrei om die ewe-ewe $^{230-234}U$, $^{236-240}Pu$ en $^{222-224}Ra$ nukliedes in te sluit. Daar is gevind dat byna alle vrygestelde swaar ione wat eksperimenteel waargeneem is deur die model voorspel word met redelike akkuraathied in die berekening van hul halfleeftye, asook dat daar goeie ooreenstemming tussen die berekende en eksperimentele waardes van ander struktuur waarneembares was.

Acknowledgements

This thesis would not have been possible without the support of certain people. My heartfelt thanks goes out in particular to my supervisors, Prof. S. M. Wyngaardt and Prof. S. M. Perez, for their guidance, encouragement and support. Our conversations have broadened my mind and helped me on my path to completing this work, teaching me several valuable lessons along the way.

I gratefully acknowledge the support of the National Institute of Theoretical Physics (NITheP), in particular for the financial support without which this work would not have been possible.

I would also like to thank Dr. T. T. Ibrahim and Ms. A. Kamblawe for their input and support during the course of this work, and the Physics Department at the University of Stellenbosch for providing me with the opportunity and necessary infrastructure.

Contents

List of Figures

List of Tables

Chapter 1

Exotic Decay in Actinide Nuclei

1.1 Introduction

It is a well established fact that unstable nuclei can decay to stable nuclei via the emission of a particle, with common modes of decay involving the emission of electrons in β decay, ^{4}He nuclei in α-decay, as well as the emission of neutrons, or via the emission of a γ-ray. Up until the 1980's, only α-decay and spontaneous fission were known modes of decay where nuclei were emitted, but theorists began predicting the existence of a further mode of decay: exotic decay [1].

The positive Q-values in many heavy particle decays implied that the decay of nuclei via the emission of a heavy particle should be possible, even though, up until that time, such a decay had not been observed. The decay of ^{228}Th for example,

$$^{228}Th \rightarrow ^{208}Pb + ^{20}O \tag{1.1.1}$$

has a Q-value of 44.723 MeV, and should therefore be a possible mode of decay for ^{228}Th.

The first experimental evidence for exotic decay came in 1984, when Rose and Jones [2] observed the emission of a particle heavier than the α-particle. They found that, in certain cases, the emission of such a particle might be observable in competition with the α-particle. Such decay was observed in ^{223}Ra, which occurs in the natural radioactive decay series from ^{235}U.

Two decay modes seemed likely: the emission of ^{14}C to ^{209}Pb with a Q-value of 32 MeV, and the emission of ^{12}C to ^{211}Pb with a Q-value of 28 MeV. When they investigated the branching ratios, emission rates and energies of the exotic decays, they concluded that the emitted particles were ^{14}C rather than other carbon isotopes [2].

After the initial discovery was made by Rose and Jones, several experimental groups at Berkeley, Dubna, Orsay and Milan developed experimental techniques to investigate the extremely rare decay modes of heavy nuclei. Even

though this was not the only motivation, the experimental investigation did yield the observation and measurement of some twenty trans-lead exotic emitters of clusters with mass numbers in the range $14 - 34$ over the course of about twenty years [3].

Indeed, an important aspect of this exciting time in nuclear physics, was the collaboration between different theoretical and experimental groups. Although there exists a vast number of exotic decay modes of heavy nuclei with positive Q-values, which are therefore all possible, most of these decays are extremely unlikely, and experimentalists required the theoreticians to develop models which could predict the more probable decays, and thus provide a guide to the experiments.

Detecting exotic emitters had its own difficulties, even with these theoretical guides. These difficulties include [3]

1. The vanishingly small branching ratios of exotic decay relative to α-decay.

2. Preparing a high enough number of mother nuclei in order to compensate for the small value of the partial decay probability. In particular, using the mother nucleus as a member of a natural radioactive series, as was done in initial experiments, rather than using artificially synthesized mother nuclei.

3. The pile-up of α-particles made it increasingly difficult to distinguish between exotic decay modes and α-decay.

4. The increasing competition from fission fragments in addition to the well-known competition from α-decay, made observing exotic decay even more difficult.

1.1.1 Experiments on Cluster Radioactivity

Cluster radioactivity occupies an intermediate position between α-particle decay and spontaneous fission. Theoretical formalisms for both α-decay and fission are well established within their particular modes, and even seem to reproduce data for exotic decay to reasonable accuracy, making it impossible to decide in favour of one or the other, or developing a successful cluster decay theoretical model, at least until more experimental data is acquired.

From an experimental point of view, the gap between α-decay and fission remains far from filled, and observation of heavier and heavier clusters is important in this respect. Some of the more important recent experiments listed by Bonetti involve the following [3].

1. ^{34}Si decay of ^{242}Cm
   This experiment analyses the cluster decay of ^{242}Cm, the heaviest mother

nucleus studied in this respect. All models predict the cluster emission of ^{34}Si and ^{208}Pb, which maximizes the decay Q-value due to strong shell effects.

2. Ne-isotope decay of ^{230}U
   This experiment is aimed at measuring a light cluster emitted by the lightest isotope of the uranium isotopic series, ^{230}U. Experiments showed that the partial half-lives for both spontaneous fission and cluster decay are of similar order of magnitude. For fission it stays about constant for all mass numbers of the parent, but it tends to vary rapidly for cluster decay. It would therefore be interesting to extend the systematics from both the light and heavy sides, and for this reason the cluster decay of ^{238}U by means of ^{34}Si is also under investigation.

3. ^{14}C decay of ^{225}Ac
   Through experiments, the sensitivity of the partial half-life of cluster decay on the microscopic properties of the mother-daughter nuclei has been shown. Even though ^{225}Ac is an odd-Z nucleus, its partial decay width and branching ratios relative to α-decay does not seem to exhibit any special behaviour, unlike other odd-A exotic emitters, making this decay of particular interest.

4. ^{15}N decay of ^{223}Ac
   The emission of ^{15}N seems to be particularly favoured when considering shell effects in the residual ^{208}Pb nucleus. From a structural point of view, it bears the same interest as the exotic decay of ^{225}Ac, but the detection of an odd-Z cluster, like ^{15}N, allows further studies in the even-odd effects in light clusters.

These experiments are just some of the interesting developments still being made in the field of experimental work on exotic decay. Even though the progress made in this field since 1984 is impressive, there is room for further progress, especially from a theoretical point of view. Although more experimental data is needed to successfully build a universal model, more work needs to be done in order to guide experiments in detecting and observing exotic decay.

1.2 Existing Theoretical Models

Since the early 1980's several theoretical models have been developed to test and predict exotic cluster radioactivity, but as mentioned in the previous section, more work needs to be done in this area. A brief overview of some of these theoretical models is given in [1], and also mentioned here.

1.2.1 Asymmetric two-centre shell model

In order to describe the formation of separate fragments forming within a nucleus, the potential is considered to consist of a superposition of two oscillators, a so-called two-centre shell model. A major drawback of the initially introduced method was that analytical solutions were only practical for the special case of semi-symmetric shapes, and not complete asymmetric shapes, as required in exotic decay [4].

The Asymmetric Two-Centre Shell Model (ATCSM) generalizes these ideas by introducing asymmetric shapes with a smooth joining of the fragments. This allows the nucleus to be considered as consisting of two fragments which are joined with a variable height of potential barrier, as shown in figure (1.1). Numerical results have shown that this model is able to generate reasonable single particle spectra [4].

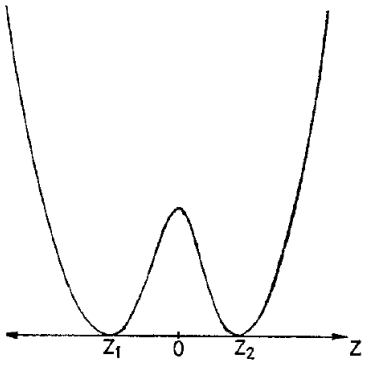

Figure 1.1: Graphical representation of the asymmetric two-centre shell model potential along the z-axis. The centre-of-mass of each fragment is indicated by z_1 and z_2 [4]

1.2.2 Fragmentation Theory

The idea was presented that the fragmentation of a nucleus could be a complete process, where the separate fragments are not joined. In order to describe this process, it is necessary to introduce the distance $\mathbf{R}$ between the centres of mass of the two fragments and the deformation tensors α_1 and α_2 which describe the excitation of the fragment surfaces as well as vibrations and rotations [5].

The most important aspect is the introduction of the collective fragmentation coordinate, $\eta = \frac{A_1 - A_2}{A_1 + A_2}$, which gives an indication of the asymmetry of the fragmentation, where A_i refers to either fragment 1 or 2. Furthermore, this relation is only useful for separated fragments, with overlapping fragments treated in the framework of the ATCSM.

The collective Hamiltonian is described as $H(\mathbf{R}, \alpha_1, \alpha_2, \eta)$, with the corresponding collective potential energy surface calculated within the ATCSM. Once the Hamiltonian is appropriately renormalized, calculations can be done [5].

1.2.3 Numerical and Analytical Superasymmetric Fission Model

Since theoretical models for fission were well established, the idea of extending these models to allow the description of superasymmetric fission, or cluster decay, seemed a likely method of describing exotic decay. However, based on experimental evidence of superasymmetric fission, fission models overestimated the height of the fission barrier. Within the Numerical (NuSAF) and Analytical (ASAF) Superasymmetric Fission Models, the fission barrier is adjusted by the inclusion of a phenomenological correction [6].

Due to the large amount of computations, the ASAF was introduced by using an analytical relationship for the half-life, while both models have been extremely successful in reproducing known experimental half-lives and predicting further possibilities [7].

1.2.4 Binary Cluster Model

The Binary Cluster Model (BCM) is the simplest choice of clustering scheme within a wider set of cluster models. Within the model, the parent nucleus consists of a cluster orbiting a core (figure 1.2), seperated by a distance r, with the two bodies interacting via some central potential. The BCM has been used to good effect across many nuclei, reproducing energy spectra, $B(E2)$ values and decay widths, and will be focused on in this work.

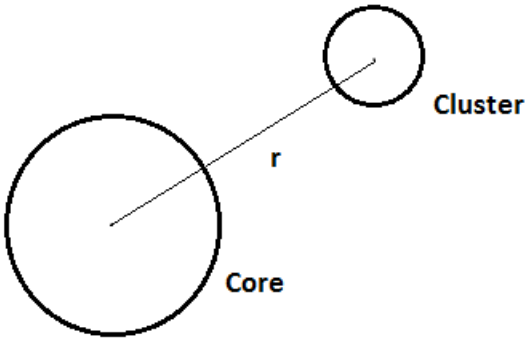

Figure 1.2: Graphical representation of the Binary Cluster Model, showing the core and cluster with separation distance r.

Chapter 2

Binary Cluster Model

The Cluster Model was first introduced by Wildermuth and Kanellopoulos in 1958 [8] in order to describe well-established models such as the shell model and α-particle-model in the frame of a general shell-like model. Later work [9] explained the usefulness of a cluster model; in that it can be easily visualized due to its similarity to molecular systems, while at the same time help solve the problem of nuclear structure.

The Binary Cluster Model (BCM) represents the simplest choice of clustering scheme within the cluster model, namely one of a core consisting of (Z_1, N_1) protons and neutrons being orbited by a cluster of (Z_2, N_2) protons and neutrons as a description of the nucleus consisting of (Z, N) protons and neutrons, where $Z = Z_1 + Z_2$ and $N = N_1 + N_2$. This simplified model has been successfully employed to describe α-cluster states in light nuclei by Buck *et al.* [10].

The major advantage of the BCM follows from the fact that a nuclear state which decays into two composite particles has a natural description as a two-cluster configuration involving these two particles, with the nuclear properties of the system determined by the internal composition and interaction of the system.

2.1 Cluster-Core Interaction

In the BCM, it is assumed that the cluster and core interact via some central potential $V(r)$. The Schrödinger equation (SE) for the relative motion of the cluster-core system is given by

$$\left(-\frac{\hbar^2}{2\mu}\nabla^2 + V(r)\right)\psi(\mathbf{r}) = E\psi(\mathbf{r}) \tag{2.1.1}$$

where r is the separation distance of the core and cluster (figure 1.2) and $\mu = \frac{A_1 A_2}{A_1 + A_2}$ is the reduced mass.

For a central potential $V(r)$ a bound state wavefunction $\psi_{nLM}(\mathbf{r})$ of the relative motion separates into radial and angular components, thus

$$\psi_{nLM}(\mathbf{r}) = \frac{\varphi_{nL}(r)}{r} Y_{LM}(\theta, \phi). \tag{2.1.2}$$

Substituting (2.1.2) into (2.1.1) results in

$$\left(-\frac{\hbar^2}{2\mu}\nabla^2 + V(r)\right) \frac{\varphi_{nL}(r)}{r} Y_{LM}(\theta, \phi) = E_{nL} \frac{\varphi_{nL}(r)}{r} Y_{LM}(\theta, \phi) \tag{2.1.3}$$

where the angular component is given by the spherical harmonics, $Y_{LM}(\theta, \phi)$, and the radial part by the wavefunction $\varphi_{nL}(r)$. The quantum number L refers to the orbital angular momentum, M to the orbital angular momentum's projection onto the z-axis and n is known as the principal quantum number.

Equation (2.1.3) separates into equations for the radial and angular parts. The radial Schrödinger Wave Equation (SWE) then reads

$$\left(-\frac{\hbar^2}{2\mu}\frac{d^2}{dr^2} + V(r)\right) \varphi_{nL}(r) = E_{nL}\varphi_{nL}(r). \tag{2.1.4}$$

The potential $V(r)$ in the radial equation consists of the nuclear potential $V_N(r)$, the Coulomb potential $V_C(r)$ and the centrifugal potential $V_L(r)$, such that

$$V(r) = V_N(r) + V_C(r) + V_L(r). \tag{2.1.5}$$

2.1.1 Coulomb Potential

The Coulomb potential is taken as a point charge Z_2 interacting with a uniformly charged spherical core Z_1 with radius R_C. It is then given by:

$$V_C(r) = \begin{cases} \dfrac{Z_1 Z_2 e^2}{r} & , \quad r \geq R_C \\ \dfrac{Z_1 Z_2 e^2}{2R_C}\left(3 - \left|\dfrac{r}{R_C}\right|^2\right) & , \quad r \leq R_C \end{cases} \tag{2.1.6}$$

For simplicity, the Coulomb radius R_C is often assumed to be equal to the nuclear potential radius R_0 in order to minimize the number of free parameters. There exists no *a priori* reason for the Coulomb radius to equal the nuclear potential radius, but this method was introduced by Buck *et al.* to good effect [11].

2.1.2 Centrifugal Potential

The centrifugal potential is associated with the orbital angular momentum L. This potential is given by

$$V_L(r) = \frac{L(L+1)\hbar^2}{2\mu r^2}. \tag{2.1.7}$$

An approximate solution to the time-independent radial SWE (2.1.4) can be obtained by utilizing the Wentzel-Kramers-Brillouin (WKB) method, described in Section (2.2). Langer [12] considered the solution under the influence of the Coulomb potential, and discovered that it gives an incorrect phase unless the number $L(L+1)$ is replaced by $(L+\frac{1}{2})^2$, if the wave function is to vanish to the proper degree at $r=0$. Langer argued that this error does not lie in the method, but rather in its application, since the commonly accepted solution is not applicable in an interval which reaches the point $r=0$, but by replacing $L(L+1)$ with $(L+\frac{1}{2})^2$, this discrepancy is fixed precisely. This replacement is commonly referred to as the Langer modification.

Since Langer only considered this modification for the Coulomb potential, Sun tested it against other potentials, and found that it applies to all translationally shape invariant potentials [13]. Within the Bohr-Sommerfeld Quantization Rule (See Section 2.2), the Langer modification also generates a contribution from the $L=0$ state, and is therefore used in all approximate calculations.

The Langer modified centrifugal potential is then given by:

$$V_L(r) = \frac{(L+\frac{1}{2})^2\hbar^2}{2\mu r^2}. \tag{2.1.8}$$

2.1.3 Nuclear Potential

An assumption often made when considering the nuclear potential is that it has some simple geometric form which depends on a certain number of parameters. From investigations into energy levels and/or elastic scattering data, these parameters can be optimized in order to reproduce experimental data [14].

Several different forms of the nuclear potential have been tested in the BCM, with varying success, and some of them are mentioned here:

1. **Square-Well Potential**
   The simplest form of the nuclear potential is that of the square-well

$$V_N(r) = \begin{cases} -V_0 & , \quad r < R_0 \\ 0 & , \quad r > R_0 \end{cases}$$

   where V_0 is the depth of the square-well and R_0 its radius.

   Used in conjuction with a surface-charge Coulomb potential, this potential successfully reproduced α-decay half-lives for heavy even-even nuclei to within a factor of ~ 2 using a fixed depth V_0 throughout [15].

   This form of the potential provided a very useful benchmark for the level of success which can be expected from the calculated α-decay half-lives when comparing them to experimental values, with the only nuclear

structure information required being the Q-value for each individual decay. The Square-Well potential, however, is unrealistic, and the calculated half-lives may somehow just be a result of the simplified geometry employed [11].

2. *Cosh*-**Potential**
   A more realistic form of the nuclear potential was that of the "*cosh*" potential
   $$V_N(r) = -V_0 \frac{1 + cosh(R_0/a)}{cosh(r/a) + cosh(R_0/a)}$$
   with potential depth V_0, diffuseness a and radius R_0.

   Buck *et al.* employed this potential, together with a Coulomb potential of the form (2.1.6), and reproduced α-decay half-lives similar to those found with the Square-Well potential [11], as well as the α- and γ-decay properties of low-lying positive parity states [16].

   Following the success of the BCM in reproducing α-decay widths, the model was extended to treat exotic decay as well. The first attempt kept the potential depth constant, and managed to reproduce exotic decay half-lives for several nuclei, using the "*cosh*"-potential [17].

   A better approach involved varying the potential depth smoothly with emitted ion mass, while keeping all other parameters constant. The exotic decay data for even-even nuclei was found to agree with experimental values to within a factor of 3, and also reproduced decay data for even-even nuclei where two different isotopes may be emitted with comparable probabilities. The only drawback was the inability to reproduce exotic decay data from odd-A nuclei [18].

   Despite the success of reproducing both α- and exotic-decay half-lives, the use of the Square-Well and "*cosh*" potential resulted in inverted spectra compared to the experimentally observed $J^\pi = 0^+, 2^+, 4^+, \cdots$ sequences [19]. Energy spectra calculations were thus found to require a more careful description of the interior of the core-cluster potential.

3. **Saxon-Woods and Saxon-Woods Cubed Potential**
   The nuclear potential has the simple form
   $$V_N = -V_0 f(r, R_0, a, x)$$
   where the depth V_0, diffuseness a and other parameters x are kept constant, but the radius R_0 is fitted separately for each nucleus.

   After a fair amount of trial and error in using different geometric forms for the nuclear potential, a form was settled on which reproduced α-decay half-lives, energy spectra and $B(E2)$ transition strengths for low-lying

positive parity states. This potential has the form

$$\begin{aligned} V_N &= -V_0 f(r, R_0, a, x) \\ &= -V_0 \left(\frac{x}{1 + exp\left[(r - R_0)/a\right]} + \frac{1 - x}{\left(1 + exp\left[(r - R_0)/3a\right]\right)^3} \right) \end{aligned} \tag{2.1.9}$$

where the parameter x indicates the relative contributions made by the Woods-Saxon and cubic Woods-Saxon terms [19].

This potential gave a good description of ^{20}Ne, ^{44}Ti and ^{212}Po, reproducing energy spectra, $B(E2)$ transition strengths, elastic scattering data and the α-decay half-life of ^{212}Po [20, 21], and is the form assumed by the core-cluster potential throughout this thesis.

Extending the BCM to incorporate the existence of larger clusters so as to describe exotic decay, certain parameters, such as the potential depth, only have to be rescaled while keeping all other parameters fixed from their best-fit values obtained from α-decay. This approach was successful in reproducing energy spectra, ground state exotic decays and $B(E2)$ transition strengths by introducing a modest effective charge [22].

The parameters used in this case were

$$V_0 = 56.6A_2 \quad x = 0.36 \quad a = 0.75 \tag{2.1.10}$$

Further exotic-cluster studies were successful in reproducing energy spectra, $B(E2)$ transition strengths and exotic-decay half-lives for nearly all even-even nuclei involving a ^{208}Pb core and even for ^{24}Mg, considered as a $^{12}C - ^{12}C$ system [14, 23].

2.2 Bohr-Sommerfeld Quantization Rule

The Bohr-Sommerfeld Quantization Rule (BS Rule) provides a semi-classical approximation to solving the one-dimensional SWE, equation (2.1.4), by utilizing the semi-classical Wentzel-Kramers-Brillouin (WKB) approximation. This procedure is described in several textbooks such as those by Zettili [24] and Griffiths [25], and only the main points will be mentioned here.

Consider the one-dimensional time-independent Schrödinger equation

$$\left[-\frac{\hbar^2}{2\mu} \frac{d^2}{dr^2} + V(r) \right] \psi = E\psi.$$

By introducing the classical momentum $p(r) = \sqrt{2\mu(E - V(r))}$, with the reduced mass $\mu = \frac{A_1 A_2}{A_1 + A_2}$, this equation becomes

$$\frac{d^2}{dr^2}\psi(r) + \frac{p^2(r)}{\hbar^2}\psi(r) = 0. \tag{2.2.1}$$

The WKB approximation aims to find an approximate treatment for slow-varying potentials, and attempts to find a solution of the form

$$\psi(r) = A(r)e^{i\phi(r)/\hbar}$$

where $A(r)$ is the amplitude and $\phi(r)$ is the phase, and both functions are real.

Assuming this form of solution, an approximate solution of (2.2.1) would be

$$\psi_{\pm}(r) \approx \frac{C_{\pm}}{\sqrt{|p(r)|}} \exp\left[\pm\frac{i}{\hbar}\int^{r} p(r')dr'\right]. \tag{2.2.2}$$

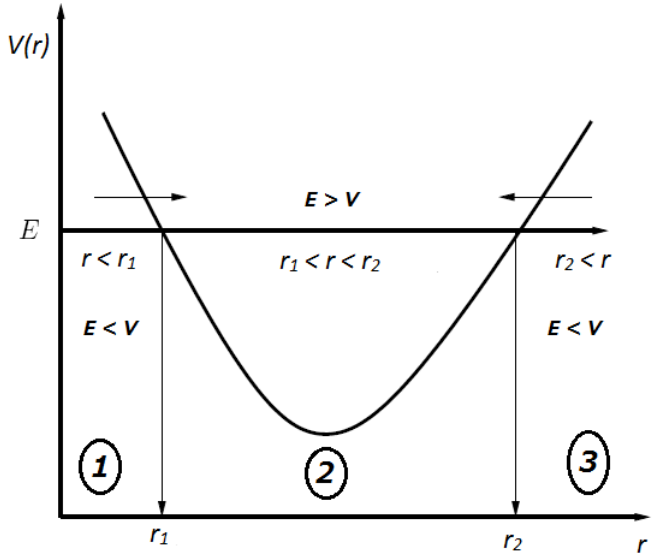

Figure 2.1: A one-dimensional potential $V(r)$ indicates the different regions and turning points r_1 and r_2. The arrows indicate the connection rule.

Considering the two separate cases corresponding to the classically forbidden regions where $V(r) > E$ and the classically allowed region where $V(r) < E$ leads to two separate equations.

Firstly, consider the classically allowed region where $E > V(r)$, $r_1 < r < r_2$ and $p(r)$ is a real function. The most general solution of equation (2.2.1) is a linear combination of $\psi_+(r)$ and $\psi_-(r)$

$$\psi(r) = \frac{C_+}{\sqrt{p(r)}} \exp\left[\frac{i}{\hbar}\int^{r} p(r')dr'\right] + \frac{C_-}{\sqrt{p(r)}} \exp\left[-\frac{i}{\hbar}\int^{r} p(r')dr'\right] \tag{2.2.3}$$

while in the classically forbidden region, $E < V(r)$, $r < r_1$ or $r > r_2$ and $p(r)$ is an imaginary function,

$$\psi(r) = \frac{C'_+}{\sqrt{|p(r)|}} \exp\left[-\frac{1}{\hbar}\int_{r} |p(r')|dr'\right] + \frac{C'_-}{\sqrt{|p(r)|}} \exp\left[\frac{1}{\hbar}\int_{r} |p(r')|dr'\right]. \tag{2.2.4}$$

The WKB approximation is valid if the wavelength $\bar{\lambda}$ of the particle is slowly varying over distances of the order of its size, i.e.

$$\left|\frac{d\bar{\lambda}}{dr}\right| \ll 1 \tag{2.2.5}$$

where $\bar{\lambda} = \frac{\lambda}{2\pi}$ and $\lambda(r)$ is the de Broglie wavelength given by

$$\lambda(r) = \frac{\hbar}{p(r)} = \frac{\hbar}{\sqrt{2\mu(E - V(r))}}. \tag{2.2.6}$$

The condition (2.2.5) is always satisfied for classical systems, and therefore the condition for validity of the WKB approximation is given by

$$\left|\frac{d\bar{\lambda}}{dr}\right| = \left|\frac{d}{dr}\left(\frac{\hbar}{p}\right)\right| \ll 1 \tag{2.2.7}$$

which breaks down at the turning points $r = r_1$ and $r = r_2$ where $E = V(r)$ and the momentum vanishes. As $p(r) \to 0$, $\lambda \to \infty$ and condition (2.2.7) is violated, which implies that the WKB approximation is valid in the classically forbidden and allowed regions, but not at the turning points. It is therefore necessary to determine the exact wavefunction at the turning points and to find a method of connecting the forbidden and allowed regions.

The solutions in the classically forbidden regions are expected to decay exponentially, while the solution must be oscillatory in the classically allowed region. This leads to three separate solutions, corresponding to the three regions (figure 2.1)

$$\begin{aligned}
\psi_1(r) &= \frac{C_1}{\sqrt{|p(r)|}} \exp\left[-\frac{1}{\hbar}\int_r^{r_1} |p(r')|dr'\right] \\
\psi_2(r) &= \frac{C_2}{\sqrt{p(r)}} \sin\left(\frac{1}{\hbar}\int_r^{r_2} p(r')dr' + \alpha\right) \\
\psi_3(r) &= \frac{C_3}{\sqrt{|p(r)|}} \exp\left[\frac{1}{\hbar}\int_{r_2}^{r} |p(r')|dr'\right]
\end{aligned} \tag{2.2.8}$$

where C_1, C_2 and C_3 are constants to be determined from connecting the solutions ψ_1, ψ_2 and ψ_3 when moving from one region to the next through the turning points $r = r_1$ and $r = r_2$, and α is some phase to be determined.

In order to connect the solutions on either side of the turning point $r = r_2$, the wavefunction at the turning point needs to be determined. The Schrödinger equation can be solved approximately near $r = r_2$, by assuming that the potential can be approximated by a straight line whose slope is equal to that of the potential at the classical turning point when $|r - r_2|$ is small enough. Expanding $V(r)$ to first order then gives

$$V(r) \approx V(r_2) + (r - r_2)\left(\frac{dV(r)}{dr}\right)_{r=r_2}$$

where $V(r_2) = E$. In this way, $V(r)$ is approximated by a straight line $(r - r_2)F_0$ with $F_0 = \left(\frac{dV(r)}{dr}\right)_{r=r_2}$ the slope of $V(r)$ at $r = r_2$.

Inserting this relation into the Schrödinger equation and changing variables to $y = \left(\frac{2mF_0}{\hbar^2}\right)^{1/3}(r - r_2)$ leads to the differential equation

$$\frac{d^2\psi(y)}{dy^2} - y\psi(y) = 0$$

for which the solution is the well-known Airy functions $Ai(y)$

$$\psi(y) = A'Ai(y) = \frac{A'}{\pi}\int_0^\infty \cos\left(\frac{z^3}{3} + yz\right)dz$$

with A' a normalization constant.

From the properties of the Airy function, the asymptotic behaviour of $Ai(y)$ and therefore $\psi(y)$ for large positive and negative values of y is

$$\psi(y) = \begin{cases} \dfrac{A'}{\sqrt{\pi}|y|^{1/4}} \sin\left[\dfrac{2}{3}(-y)^{3/2} + \dfrac{\pi}{4}\right] & , y \ll 0 \\ \dfrac{A'}{2\sqrt{\pi}y^{1/4}} \exp\left[-\dfrac{2}{3}y^{3/2}\right] & , y \gg 0 \end{cases}$$

By investigating the relationship of the limits $y \gg 0$ and $y \ll 0$ to r, and using the relation

$$\frac{1}{\hbar}\int_r^{r_2} p(r')dr' = \frac{2}{3}(-y)^{3/2}$$

the solution becomes

$$\psi(r) = \begin{cases} \dfrac{A}{\sqrt{p(r)}} \sin\left(\dfrac{1}{\hbar}\displaystyle\int_r^{r_2} p(r')dr' + \dfrac{\pi}{4}\right) & , r \ll r_2 \\ \dfrac{A}{2\sqrt{|p(r)|}} \exp\left[-\dfrac{1}{\hbar}\displaystyle\int_r^{r_2} |p(r')|dr'\right] & , r \gg r_2 \end{cases} \tag{2.2.9}$$

and on comparing equation (2.2.9) to equation (2.2.8), it is clear that $\alpha = \frac{\pi}{4}$ and $C_2 = 2C_3$.

A similar procedure for connecting the solutions on either side of the turning point $r = r_1$ gives the solution

$$\psi(r) = \begin{cases} \dfrac{A'}{2\sqrt{|p(r)|}} \exp\left[-\dfrac{1}{\hbar}\displaystyle\int_{r_1}^{r} |p(r')|dr'\right] & , r \ll r_1 \\ \dfrac{A'}{\sqrt{p(r)}} \sin\left(\dfrac{1}{\hbar}\displaystyle\int_{r_1}^{r} p(r')dr' + \dfrac{\pi}{4}\right) & , r \gg r_1 \end{cases} \tag{2.2.10}$$

The oscillatory solutions of equations (2.2.9) and (2.2.10) describe the same region, and must therefore be equal, i.e.

$$\psi_2(r) = \frac{A'}{\sqrt{p(r)}} \sin\left(\frac{1}{\hbar}\int_{r_1}^{r} p(r')dr' + \frac{\pi}{4}\right) = \frac{A}{\sqrt{p(r)}} \sin\left(\frac{1}{\hbar}\int_{r}^{r_2} p(r')dr' + \frac{\pi}{4}\right) \tag{2.2.11}$$

which has the simplified form $A' \sin\theta_1 = A \sin\theta_2$. Its solutions must therefore satisfy two relations:

$$\theta_1 + \theta_2 = (n+1)\pi \tag{2.2.12}$$

$$A' = (-1)^n A \tag{2.2.13}$$

where the first relation (2.2.12) leads to the well-known Bohr-Sommerfeld Quantization Rule

$$\int_{r_1}^{r_2} \sqrt{\frac{2\mu}{\hbar^2}(E_n - V(r))}dr = (2n+1)\frac{\pi}{2} \tag{2.2.14}$$

which can be used to determine the quantized (WKB) energy levels E_n of the bound states of a semi-classical system.

2.3 Global Quantum Number

The BCM adopts the most extreme form of the cluster model, considering a point-like cluster in an orbit around an inert core. The orbit is specified by an internal node number n and an orbital quantum number L. According to the Pauli Exclusion Principle, two nucleons cannot occupy the same state, and therefore the nucleons which make up the cluster have to be placed above the Fermi surface of the core nucleons. The values of n and L are then related to the n_i and l_i of each cluster nucleon by

$$2n + L = \sum_{i=1}^{n_c}(2n_i + l_i) \tag{2.3.1}$$

where n_c is the number of nucleons in the cluster. The values of n_i and l_i correspond to the filling of the shell-model orbitals above the closed core, satisfying the Pauli principle by hand [10].

The global quantum number is defined as

$$G = 2n + L. \tag{2.3.2}$$

This relation gives rise to a band of states, corresponding to all states which share a common value of G. For an even number G, the states form a positive parity band with $L = 0, 2, 4, ...$ up until $L = G$, while for an odd G, the states form a negative parity band with $L = 1, 3, 5, ...$ [19].

Much of the success of the BCM lies in the choice of G. The assumption is made that the cluster-core relative motion wavefunction contains many nodes, such that the motion is characterized by a large value of the global quantum number G. This value is not fixed *a priori*, but rather treated as a free parameter, for which several values are admissable, given the appropriate changes are made in other parameters [11].

For exotic decay, it is assumed that good fits to exotic-decay half-lives can be obtained from the best-fit potentials for α-decay simply by scaling certain parameters. The global quantum number is then taken to be proportional to the emitted ion mass number A_2, such that

$$G \sim A_2 G_\alpha / 4$$

where G_α is the quantum number of the best-fit α-decay potential. This scaling is consistent with placing more nucleons outside the core, forming heavier clusters [22].

After fine-tuning the parameters to fit exotic-decay data, the optimal value in the actinide region was found to be [18, 22]

$$G = 5A_2. \tag{2.3.3}$$

Substituting the relation of the global quantum number (2.3.2) into the BS Rule (2.2.14) gives

$$\int_{r_1}^{r_2} \sqrt{\frac{2\mu}{\hbar^2}\left(E_L - V_L(r)\right)}dr = (G - L + 1)\frac{\pi}{2} \tag{2.3.4}$$

which can be used to calculate the energy levels of the band if the potential $V_L(r)$ is known and the global quantum number G specified. The energy E_L associated with different values of the angular momentum L and therefore the energy levels of the band, can then be calculated.

Chapter 3

Measurable Structure Observables

Several properties of a nucleus can be measured experimentally. Apart from the energy spectra, transitions between different states lead to the emission of electromagnetic waves, while particles such as nucleons, β- and α-particles, and heavier ions can also be emitted. It is the aim of this chapter to establish theoretical expressions to calculate these properties of nuclei in order to compare the predictions of our model with experimentally observed quantities.

3.1 Electromagnetic Transitions

Nuclei left in an excited state can decay to a lower state via the emission of a quantum of radiation. Electromagnetic transitions refer to the nuclear decay through the emission of a γ-ray, caused by the interaction of the nucleus with an external electromagnetic field [27].

The nucleus has inherent electromagnetic properties when considered as a collection of point nucleons, each with a magnetic dipole moment and net charge. "Electric" transitions are caused by the coupling of the charge distribution with the external field, while "magnetic" transitions are caused by the interaction of the intrinsic magnetism of each nucleon with the magnetism created by current loops due to the orbital motion of protons.

Electromagnetic (EM) transitions, by the emission of a γ-ray, form the dominant mode of decay for low-lying excited states in nuclei, since the emission of nucleons is not possible until the excitation energy is above nucleon seperation energies. The emission of β- and α-particles, as well as heavier ions, however, occur on a much longer timescale. The energy of any such transition can be measured, as well as a transition probability, which is of interest here.

The transition probability is taken as a constant of proportionality, assuming the number of decays taking place in a given time interval is proportional to the number of radioactive nuclei, $N(t)$, and that the probability of any one radioactive nucleus to decay is not influenced by the status of any other nuclei.

This can be written as

$$\frac{dN}{dt} = -\mathcal{W}N(t) \tag{3.1.1}$$

where $\mathcal{W}$ is the constant of proportionality: the transition probability. While the wavefunctions of nuclear states are taken as the eigenfunctions of a Hamiltonian where the only interaction is nuclear, transitions are caused by perturbations. The transition probability then depends on the particular nature of the perturbation, which was investigated by S.M. Wong [27], and briefly discussed here.

3.1.1 Fermi's Golden Rule

The transition probability is defined as the probability of emission per unit time of a quantum of radiation with angular momentum (ℓ, m) from an initial state (J_i, M_i) to a final state (J_f, M_f), caused by some perturbation.

Consider a time-dependent Hamiltonian

$$H(t) = H_0 + H'(t) \tag{3.1.2}$$

where all the time-dependence is contained in the sufficiently weak term $H'(t)$, such that it may be considered as a perturbation.

Let $\phi_n(\mathbf{r})$ represent an eigenfunction of the time independent Hamiltonian H_0,

$$H_0\phi_n(\mathbf{r}) = E_n\phi_n(\mathbf{r})$$

where $\phi_n(\mathbf{r})$ forms a complete set of orthonormal functions. The eigenfunctions $\psi(\mathbf{r}, t)$ form solutions to the time-dependent Schrödinger Equation (SE) for H_0 alone,

$$i\hbar\frac{\partial\psi(\mathbf{r}, t)}{\partial t} = H_0\psi(\mathbf{r}, t)$$

and may be expressed in terms of $\phi_n(\mathbf{r})$,

$$\psi(\mathbf{r}, t) = \sum_n c_n\phi_n(\mathbf{r})e^{-iE_nt/\hbar}$$

with expansion coefficients

$$c_n = \int \phi_n^*(\mathbf{r})e^{iE_nt/\hbar}\psi(\mathbf{r}, t)dV$$

which are independent of time, since the perturbation $H'(t)$ has not yet been included.

For the complete Hamiltonian, the eigenfunctions can be expressed in terms of time-dependent expansion coefficients,

$$\Psi(\mathbf{r}, t) = \sum_n c_n(t)\phi_n(\mathbf{r})e^{-iE_nt/\hbar} \tag{3.1.3}$$

where the expansion coefficient $c_n(t)$ can be interpreted as the probability amplitude for finding the system in the unperturbed state ϕ_n at time t.

Substituting these results into the time-dependent SE for the time-dependent Hamiltonian $H(t)$ leads to a differential equation for $c_k(t)$,

$$i\hbar\frac{dc_k(t)}{dt} = \sum_n \langle\phi_k| H'(t) |\phi_n\rangle e^{i\omega_{kn}t} \tag{3.1.4}$$

where $\omega_{kn} = (E_k - E_n)/\hbar$ and the properties of an orthonormal set of functions have been used.

If it is assumed that the system is in a state $\phi_0(\mathbf{r})$ at time $t = 0$, the initial conditions can be written as,

$$c_n(0) = \begin{matrix} 1 & for & n = 0 \\ 0 & for & n \neq 0 \end{matrix}$$

and a similar result for $c_k(t)$ can be assumed for a sufficiently weak perturbation. As a result, equation (3.1.4) can be approximated by retaining only the $n = 0$ term, giving the result

$$i\hbar\frac{dc_k(t)}{dt} = \langle\phi_k| H'(t) |\phi_0\rangle e^{i\omega_{k0}t}$$

which can be solved explicitly by using a Taylor expansion, if it is assumed that the time variation of $H'(t)$ is slow compared with $\exp[i\omega_{k0}t]$, which implies that H' can be taken as constant. The result is given by

$$c_k(t) = \frac{\langle\phi_k| H' |\phi_0(t)\rangle}{E_k - E_0}(1 - e^{i\omega_{k0}t})$$

of which the square gives the total probability for finding the system in a state ϕ_k at time t if it evolved from a state ϕ_0 at time $t = 0$.

The total probability for a transition to a group of final states within an interval labeled by f, is given by the sum over all the final states k within the interval,

$$\begin{aligned}\sum_{k\in f} |c_k(t)| &= 2\sum_{k\in f} |\langle\phi_k(\mathbf{r})| H' |\phi_0(\mathbf{r})\rangle|^2 \frac{1 - \cos(\omega_{k0}t)}{(E_k - E_0)^2} \\ &= \frac{2}{\hbar^2}\int |\langle\phi_k(\mathbf{r})| H' |\phi_0(\mathbf{r})\rangle|^2 \frac{1 - \cos(\omega_{k0}t)}{\omega_{k0}^2}\rho(E_k)dE_k\end{aligned} \tag{3.1.5}$$

where the summation over all possible final states have been replaced by an integral over the energy multiplied by the density of final states $\rho(E_k)$.

The rate of finding the system in the group of final states labeled by f, is known as the transition probability per unit time, $\mathcal{W}$, and expressed as

$$\mathcal{W} = \frac{d}{dt}\sum_{k\in f} |c_k(t)| = \frac{2}{\hbar^2}\int |\langle\phi_k(\mathbf{r})| H' |\phi_0(\mathbf{r})\rangle|^2 \frac{\sin\omega_{k0}t}{\omega_{k0}}\rho(E_k)dE_k$$

The function $\sin(\omega_{k0}t)/\omega_{k0}$ oscillates rapidly except where $\omega_{k0} \approx 0$, and therefore only a small region around $E_k = E_0$ contributes to the integral. This allows the assumption that the matrix element $\langle\phi_k(\mathbf{r})| H' |\phi_0(\mathbf{r})\rangle$, and the state density $\rho(E_k) = \rho(E_f)$, can be taken as constants, and are therefore independent of E_0. Furthermore, the limits of the integral can be extended to $\pm\infty$ without sacrificing too much accuracy. The final form of the transition probability per unit time then takes on the form

$$\mathcal{W} = \frac{2\pi}{\hbar} |\langle\phi_f(\mathbf{r})| H' |\phi_0(\mathbf{r})\rangle|^2 \rho(E_f) \tag{3.1.6}$$

which is known as *Fermi's golden rule*, and forms the starting point for all calculations of transition probabilities.

3.1.2 Electromagnetic Field

The nuclear decay through the emission of a γ-ray is of main interest here. This mode of decay occurs when the nucleus decays from an excited state to a lower state, and is caused by the interaction of the nucleus with an external electromagnetic field. The aim of this section is to find an expression of the time-dependent perturbation (equation 3.1.6) which can be used to calculate transition probabilities.

The first step is to separate the perturbation Hamiltonian H' into a product of two operators, the first acting only on the nuclear part and the second acting only on the external electromagnetic field. The external electromagnetic field should be quantized and decomposed by multipole expansion into components with definite spherical tensor ranks, since each nuclear state has a definite angular momentum.

First consider a point particle carrying a charge q. In the absence of an external electromagnetic field, the particle is considered as free and the Hamiltonian consists of only the kinetic energy term,

$$H_0 = \frac{1}{2m}\mathbf{p}^2 \tag{3.1.7}$$

where $\mathbf{p}$ is the momentum. In the presence of an external electromagnetic field, the momentum gets modified,

$$\mathbf{p} \to \mathbf{p} + \frac{q}{c}\mathbf{A}$$

where $\mathbf{A}$ is the vector potential for the electromagnetic field.

The interaction of the electric charge of the protons in a nucleus creates a perturbation to the free Hamiltonian H_0. Apart from the electric charge, the intrinsic magnetic dipole moment of the nucleons can also interact with the external electromagnetic field, which can be expressed in the form of a current. The most general form of the perturbation H' then includes these

interactions, as well as the possibility for the charge distribution to interact with an external electrostatic field. The perturbation is then written in four-component notation,

$$H' = -\frac{1}{c}\sum_{\mu=1}^{4} A_\mu J_\mu \tag{3.1.8}$$

where $A_\mu = (\mathbf{A}, iV)$ and $J_\mu = (\mathcal{J}, i\rho c)$ and the current density $\mathcal{J} = q\frac{\mathbf{p}}{m}$. This notation includes a scalar potential V and charge distribution ρ for interactions with an electrostatic field, although these contributions are usually not important in nuclear transitions.

The electromagnetic field is obtained from the solution to Maxwell's equations,

$$\left(\nabla^2 - \frac{1}{c^2}\frac{\partial^2}{\partial t^2}\right)\mathbf{A}(\mathbf{r}, t) = 0. \tag{3.1.9}$$

The vector potential can be expanded in terms of components with definite wave number $\mathbf{k}$, indicating the direction of propagation of the wave. The time-dependence can then be written explicitly,

$$\mathbf{A}(\mathbf{r}, t) = \sum_{\mathbf{k}} \mathbf{A}_\mathbf{k}(\mathbf{r})e^{-i\omega t} \tag{3.1.10}$$

where $\omega = kc$ with k being the magnitude of $\mathbf{k}$. The spatial dependence of $\mathbf{A}$ is then given by the equation

$$\left(\nabla^2 + k^2\right)\mathbf{A}_\mathbf{k}(\mathbf{r}) = 0 \tag{3.1.11}$$

of which the solution is substituted back into the expansion of $\mathbf{A}$ to obtain

$$\mathbf{A}(\mathbf{r}, t) = \frac{1}{N}\sum_{\mathbf{k}}\sum_{\eta}\left(\mathbf{b}_{\mathbf{k}\eta}\epsilon_\eta e^{i(\mathbf{k}\cdot\mathbf{r}-\omega t)} + \mathbf{b}^\dagger_{\mathbf{k}\eta}\epsilon_\eta e^{-i(\mathbf{k}\cdot\mathbf{r}-\omega t)}\right). \tag{3.1.12}$$

From the condition $\nabla \cdot \mathbf{A} = 0$, only two of the three components of the vector field are independent. This is indicated by two unit vectors ϵ_η with $\eta = 1, 2$, indicating the polarization of the photons. The factors $\mathbf{b}_{\mathbf{k}\eta}$ and $\mathbf{b}^\dagger_{\mathbf{k}\eta}$ are seen as constants to be determined from the boundary conditions.

This expression of the vector potential allows a quantum-mechanical description of the electromagnetic field. $\mathbf{b}_{\mathbf{k}\eta}$ and $\mathbf{b}^\dagger_{\mathbf{k}\eta}$ can be interpreted as creation and annihilation operators, respectively, of photons with wavenumber $\mathbf{k}$ and polarization direction η. This leads to the physical interpretation that coupling between nuclear and electromagnetic fields enables the creation of a photon when the nucleus decays from an excited state to a lower state, and the absorption of a photon when it is excited to a higher state.

The expansion of $\mathbf{A}(\mathbf{r},t)$ in equation (3.1.12) is carried out explicitly in Cartesian coordinates, but for systems with spherical symmetry it is more convenient to express $\mathbf{A}(\mathbf{r},t)$ in terms of operators having definite spherical tensor ranks. In order to do this, consider the time-independent scalar differential equation

$$(\nabla^2 + k^2)\Phi(\mathbf{r}) = 0$$

where the time-dependence of the scalar function $\Phi(\mathbf{r},t)$ can be written as $\Phi(\mathbf{r},t) = \Phi(\mathbf{r})\exp[-i\omega t]$. The solution to the scalar function is given in spherical coordinates [28]

$$\begin{aligned}\Phi_{\lambda\mu}(\mathbf{r},t) &= \Phi_{\lambda\mu}(r,\theta,\phi,t)\\ &= f_\lambda(kr)Y_{\lambda\mu}(\theta,\phi)e^{-i\omega t}\end{aligned} \tag{3.1.13}$$

where the function $Y_{\lambda\mu}(\theta,\phi)$ is the usual spherical harmonics, and the radial function $f_\lambda(kr)$. For a spherical standing wave,

$$f_\lambda(kr) = j_\lambda(kr)$$

the radial function is the spherical Bessel function. For outgoing or incoming spherical waves, $f_\lambda(kr) = h_\lambda^{(1)}(kr)$ or $f_\lambda(kr) = h_\lambda^{(2)}(kr)$, it is spherical Hankel functions of the 1^{st} or 2^{nd} kind, respectively, such that the radial functions differ in singularity properties [28].

The solution to the vector wave equation (equation 3.1.11) must correspond to the scalar functions $\Phi_{\lambda\mu}(\mathbf{r})$ by applying vector-differential operations on the spherical scalar solutions, while still satisfying the identity $\nabla\cdot\mathbf{A} = 0$.

The orbital angular momentum operator is introduced in order to connect the spherical scalar solutions to the vector solutions,

$$\mathbf{L} = -i\mathbf{r}\times\nabla \tag{3.1.14}$$

which operates on the angular coordinates, θ and ϕ. By applying this operator to the spherical scalar solutions, two vector field solutions are found for the vector differential equation (equation 3.1.9), i.e.

$$\begin{aligned}\mathbf{L}\Phi_{\lambda\mu}(\mathbf{r},t) &= -i(\mathbf{r}\times\nabla)f_\lambda(kr)Y_{\lambda\mu}(\theta,\phi)e^{-i\omega t}\\ (\nabla\times\mathbf{L})\Phi_{\lambda\mu}(\mathbf{r},t) &= -i\nabla\times(\mathbf{r}\times\nabla)f_\lambda(kr)Y_{\lambda\mu}(\theta,\phi)e^{-i\omega t}\end{aligned} \tag{3.1.15}$$

which are transverse vector fields satisfying the condition $\nabla\cdot\mathbf{A} = 0$ [28].

These two solutions correspond to two different types of multipole fields, satisfying equation (3.1.11). Decays induced by them are called *electric* multipole transitions, $E\lambda$, and *magnetic* multipole transitions, $M\lambda$. They are written, in terms of spherical harmonics, as

$$\begin{aligned}\mathbf{A}_{\lambda\mu}(M\lambda,\mathbf{r},t) &= \frac{-i}{[\lambda(\lambda+1)]^{1/2}}(\mathbf{r}\times\nabla)\left(j_\lambda(kr)Y_{\lambda\mu}(\theta,\phi)\right)e^{-i\omega t}\\ \mathbf{A}_{\lambda\mu}(E\lambda,\mathbf{r},t) &= -\frac{-i}{k[\lambda(\lambda+1)]^{1/2}}\nabla\times(\mathbf{r}\times\nabla)\left(j_\lambda(kr)Y_{\lambda\mu}(\theta,\phi)\right)e^{-i\omega t}\end{aligned} \tag{3.1.16}$$

where $j_\lambda(kr)$ is the spherical Bessel function of order λ. A linear combination of both types of terms is the general solution of $\mathbf{A}(\mathbf{r},t)$.

Writing the perturbing Hamiltonian H' (Eq. 3.1.8) in terms of multipole operators allows the introduction of an electric and magnetic multipole operator [28],

$$\begin{aligned}\mathbf{O}_{\lambda\mu}(E\lambda) &= \frac{(2\lambda+1)!!}{ck^\lambda(\lambda+1)}[\lambda(\lambda+1)]^{1/2}\mathcal{J}(\mathbf{r})\cdot\mathbf{A}_{\lambda\mu}(E\lambda,\mathbf{r})\\ \mathbf{O}_{\lambda\mu}(M\lambda) &= -i\frac{(2\lambda+1)!!}{ck^\lambda(\lambda+1)}[\lambda(\lambda+1)]^{1/2}\mathcal{J}(\mathbf{r})\cdot\mathbf{A}_{\lambda\mu}(M\lambda,\mathbf{r})\end{aligned}$$

which are spherical tensors of rank λ.

Substituting the expressions for $\mathbf{A}_{\lambda\mu}(M\lambda,\mathbf{r})$ and $\mathbf{A}_{\lambda\mu}(E\lambda,\mathbf{r})$ into these expressions yields [27]

$$\begin{aligned}\mathbf{O}_{\lambda\mu}(E\lambda) &= -i\frac{(2\lambda+1)!!}{ck^{\lambda+1}(\lambda+1)}\mathcal{J}(\mathbf{r})\cdot\nabla\times(\mathbf{r}\times\nabla)\left(j_\lambda(kr)Y_{\lambda\mu}(\theta,\phi)\right)\\ \mathbf{O}_{\lambda\mu}(M\lambda) &= -\frac{(2\lambda+1)!!}{ck^\lambda(\lambda+1)}\mathcal{J}(\mathbf{r})\cdot(\mathbf{r}\times\nabla)\left(j_\lambda(kr)Y_{\lambda\mu}(\theta,\phi)\right)\end{aligned} \tag{3.1.17}$$

which are the multipole operators for electric and magnetic transitions, written in spherical coordinates.

Typical γ-rays involved in nuclear energies, E_γ, are less than 10 MeV, resulting in wave numbers $k = E_\gamma/\hbar c \approx 1/20fm^{-1}$ or less. The multipole operators only act on the nuclear wavefunctions, which cannot extend beyond the nucleus itself, and even heavy nuclei are smaller than $10fm$, which implies that the product kr is less than one. The Bessel function can then be approximated to its first term when expanded,

$$j_\lambda(kr) \approx \frac{(kr)^\lambda}{(2\lambda+1)!!}\left(1-\frac{1}{2}\frac{(kr)^2}{2\lambda+3}+\cdots\right) \tag{3.1.18}$$

which results in the long-wavelength limit.

Under the assumption that the electric charge in a nucleus originates from point charges carried by individual protons, and magnetization current originates from the magnetic dipole moments of individual nucleons and the orbital motion of protons, the electric and magnetic multipole operators simplify within the long-wavelength limit to

$$\begin{aligned}\mathbf{O}_{\lambda\mu}(E\lambda) &= \sum_{i=1}^{A} e(i)r_i^\lambda Y_{\lambda\mu}(\theta_i,\phi_i)\\ \mathbf{O}_{\lambda\mu}(M\lambda) &= \sum_{i=1}^{A}\left(g_s(i)s_i + g_\ell(i)\frac{2\ell_i}{\lambda+1}\right)\cdot\nabla_i(r_i^\lambda Y_{\lambda\mu}(\theta_i,\phi_i))\end{aligned} \tag{3.1.19}$$

where $e(i) = 1e$ for protons and $e(i) = 0$ for neutrons. A similar distinction is made for magnetic transitions, where $g_\ell(i) = 1\mu_N$ for protons and $g_\ell(i) = 0$ for neutrons, while $g_s(i) = 5.586\mu_N$ for protons and $g_s(i) = -3.826\mu_N$ for neutrons.

The multipole operators can now be inserted into the transition probability, equation (3.1.6). The density of states is obtained by considering the transition probability to be proportional to the nuclear matrix element, $\mathcal{M}_{fi}(\mu_f, \mu_i) = \langle \lambda_f \mu_f | \mathbf{O}_{\lambda\mu} | \lambda_i \mu_i \rangle$. By considering the wavefunctions and transition operator to be plane waves, the density of states can be approximated by the normalization obtained from a transformation from plane waves to spherical waves [28].

When inserting the density of final states and using the multipole operator (equation 3.1.19), the transition probability for multipole λ from an initial state $|J_i M_i\rangle$ to a final state $|J_f M_f\rangle$ can be written as

$$\mathcal{W}(\lambda; J_i \to J_f) = \frac{8\pi(\lambda+1)}{\lambda[(2\lambda+1)!!]^2} \frac{k^{2\lambda+1}}{\hbar} B(\lambda; J_i \to J_f) \tag{3.1.20}$$

where the reduced transition probability $B(\lambda; J_i \to J_f)$ can be written in terms of the reduced matrix element of the multipole operator,

$$\begin{aligned} B(\lambda; J_i \to J_f) &= \sum_{\mu M_f} |\langle J_f M_f | \mathbf{O}_{\lambda\mu} | J_i M_i \rangle|^2 \\ &= \frac{1}{2J_i + 1} |\langle J_f | \mathbf{O}_\lambda | J_i \rangle|^2 . \end{aligned} \tag{3.1.21}$$

3.2 Reduced Electromagnetic Transitions

The transition probability (equation 3.1.20) contains a factor $k^{2\lambda+1} = (E/\hbar c)^{2\lambda+1}$. Due to this high power of the energy, it is often more useful to calculate the reduced transition probability, equation (3.1.21). This form of the reduced transition probability, however, has to be simplified in order to be calculated within the BCM.

Of particular importance is the electric transition. Experimental values on electric transitions between positive parity states, especially low-lying states, such as $2^+ \to 0^+$ are abundant, and therefore more useful to investigate.

In order to do this, a change of notation is first introduced. Since λ refers to angular momentum, it is more appropriate to label this by ℓ, while μ refers to the projection of angular momentum and is therefore labeled by m. The reduced transition probability and electric multipole operator therefore takes on the form,

$$B(\ell; J_i \to J_f) = \frac{1}{2J_i + 1} |\langle J_f M_f | \mathbf{O}_\ell | J_i M_i \rangle|^2$$

$$\mathbf{O}_{\ell m}(E\ell) = \sum_{i=1}^{A} e(i) r_i^\ell Y_{\ell m}(\theta_i, \phi_i)$$

where the sum in the multipole operator is taken over all protons at position (r_i, θ_i, ϕ_i), since $e(i) = 0$ for neutrons. Within the BCM, this amounts to a sum taken over the two total charges Z_1 and Z_2 of the core and cluster [26],

$$\begin{aligned}
\mathbf{O}_{\ell m}(E\ell) &= \sum_{i=1}^{Z} e(i) r_i^\ell Y_{\ell m}(\theta_i, \phi_i) \\
&\approx Z_1 r_1^\ell Y_{\ell m}(\theta_1, \phi_1) + Z_2 r_2^\ell Y_{\ell m}(\theta_2, \phi_2) \\
&= Z_1 r_1^\ell Y_{\ell m}(\pi - \theta, \pi + \phi) + Z_2 r_2^\ell Y_{\ell m}(\theta, \phi) \\
&= \left[(-1)^\ell Z_1 r_1^\ell + Z_2 r_2^\ell\right] Y_{\ell m}(\theta, \phi) \\
&= \left[Z_1 \left(-\frac{A_2 r}{A}\right)^\ell + Z_2 \left(\frac{A_1 r}{A}\right)^\ell\right] Y_{\ell m}(\theta, \phi) \\
&= \left[Z_1 \left(-\frac{A_2}{A}\right)^\ell + Z_2 \left(\frac{A_2}{A}\right)^\ell\right] r^\ell Y_{\ell m}(\theta, \phi) \\
&= \beta_\ell r^\ell Y_{\ell m}(\theta, \phi)
\end{aligned} \tag{3.2.1}$$

where the behavior of the spherical harmonics under a parity change has been used, a change to centre of mass coordinates has been made, and the shorthand notation

$$\beta_\ell = \left[Z_1 \left(-\frac{A_2}{A}\right)^\ell + Z_2 \left(\frac{A_2}{A}\right)^\ell\right]$$

has been introduced.

The wavefunction for the cluster-core motion (equation 2.1.2), written in bra-ket notation for convenience,

$$|LM\rangle = \frac{\psi_L(r)}{r} Y_{LM}(\theta, \phi)$$

reduces the reduced transition probability for a transition from some initial state $|L_i M_i\rangle$ to the 0^+ ground state,

$$\begin{aligned}
B(E\ell; \ell \to 0^+) &= \sum_{m M_f} \left|\left\langle 0^+ \right| \mathbf{O}_{\ell m}(E\ell) \left| L_i M_i \right\rangle\right|^2 \\
&= \left|\left\langle \frac{\psi_0(r)}{r} Y_{00}(\theta, \phi) \right| \beta_\ell r^\ell Y_{\ell m}(\theta, \phi) \left| \frac{\psi_\ell(r)}{r} Y_{\ell m}(\theta, \phi) \right\rangle\right|^2 \\
&= \frac{1}{4\pi} \left| \beta_\ell \int_0^\infty \frac{\psi_0^*(r)}{r} r^\ell \frac{\psi_\ell(r)}{r} r^2 dr \right|^2
\end{aligned} \tag{3.2.2}$$

where the angular dependence and spherical harmonics have been integrated over.

3.2.1 Dipole Transitions

Dipole transitions involve transitions between states of opposite parities, with $\ell = 1$. The reduced transition probability, for a transition to the ground state, then takes on the form

$$B(E1; 1^- \to 0^+) = \frac{1}{4\pi} \left| \beta_1 \int_0^\infty \psi_0^*(r) r \psi_1(r) dr \right|^2 .$$

Experimental observations have revealed that dipole transitions between low-lying states are very weak in heavy nuclei [29]. This approximately requires the vanishing of the reduced transition probability, or the vanishing of the charge factor,

$$\begin{aligned} \beta_1 &= Z_1 \left(-\frac{A_2}{A} \right) + Z_2 \left(\frac{A_1}{A} \right) \\ &= \left(\frac{Z_2}{A_2} - \frac{Z_1}{A_1} \right) \frac{A_1 A_2}{A_1 + A_2} \\ &\approx 0 \end{aligned}$$

which leads to the no dipole condition, or dipole constraint

$$\frac{Z_1}{A_1} = \frac{Z_2}{A_2} = \frac{Z}{A} \tag{3.2.3}$$

where $A = A_1 + A_2$ and $Z = Z_1 + Z_2$.

3.2.2 Quadrupole Transitions

Quadrupole transitions involve transitions between states of the same parity, with $\ell = 2$. The reduced transition probability, for a transition to the ground state, then takes on the form

$$\begin{aligned} B(E2; 2^+ \to 0^+) &= \frac{1}{4\pi} \left| \left(Z_1 \left(-\frac{A_2}{A} \right)^2 + Z_2 \left(\frac{A_1}{A} \right)^2 \right) \int_0^\infty \psi_0^*(r) r^2 \psi_2(r) dr \right|^2 \\ &\approx \frac{1}{4\pi} \left| \frac{Z_1 Z_2}{Z} \int_0^\infty \psi_0^*(r) r^2 \psi_2(r) dr \right|^2 \end{aligned} \tag{3.2.4}$$

when applying the no dipole condition (equation 3.2.3).

3.2.3 Reduced Transition Probability for Arbitrary Transitions

For an electric multipole transition of order ℓ from an initial state $|L_i M_i\rangle$ to a final state $|L_f M_f\rangle$, a generalized transition probability is given by

$$\begin{aligned}
B(\ell; L_i \to L_f) &= \sum_{mM_f} |\langle L_f M_f| \mathbf{O}_{\ell m}(E\ell) |L_i M_i\rangle|^2 \\
&= \sum_{mM_f} \left|\langle L_f M_f| \beta_\ell r^\ell Y^*_{\ell m}(\theta,\phi) |L_i M_i\rangle\right|^2 \\
&= \sum_{mM_f} \left|(-1)^m \langle L_f M_f| \beta_\ell r^\ell Y^*_{\ell -m}(\theta,\phi) |L_i M_i\rangle\right|^2 \\
&= \sum_{mM_f} |\langle L_i M_i \ell - m | L_f M_f\rangle|^2 \left|\langle L_f||\beta_\ell r^\ell Y_\ell||L_i\rangle\right|^2 \\
&= \sum_{mM_f} \frac{2L_f+1}{2L_i+1} |\langle L_f M_f \ell m | L_i M_i\rangle|^2 \left|\langle L_f||\beta_\ell r^\ell Y_\ell||L_i\rangle\right|^2 \\
&= \frac{2L_f+1}{2L_i+1} \left|\langle L_f||\beta_\ell r^\ell Y_\ell||L_i\rangle\right|^2 \\
&= \left(\frac{\hat{L_f}}{\hat{L_i}}\right)^2 \left|\langle L_f||\beta_\ell r^\ell Y_\ell||L_i\rangle\right|^2
\end{aligned} \tag{3.2.5}$$

where the behaviour of spherical harmonics under parity changes, the Wigner-Eckart Theorem, and symmetry and completeness relations of Clebsch-Gordan coefficients [24, 30] have been used. The short-hand notation

$$\beta_\ell = \left[Z_1 \left(-\frac{A_2}{A}\right)^\ell + Z_2 \left(\frac{A_1}{A}\right)^\ell\right]$$

and

$$\hat{L} = \sqrt{2L+1}$$

has also been introduced.

It is interesting to note that, in the actinide region where the parent nucleus consists of a large core, typically ^{208}Pb, $A_1 \gg A_2$ so that $\beta_\ell \sim Z_2$ and therefore the reduced electromagnetic transition probability increases with increasing cluster charge.

Evaluating the reduced matrix element [31],

$$\begin{aligned}
\left|\langle L_f||\beta_\ell r^\ell Y_\ell||L_i\rangle\right|^2 &= (-1)^{2\ell}\sum_{M'q}\langle L_iM'\ell q|L_fM\rangle\,\langle L_fM|\,\beta_\ell r^\ell Y_{\ell q}\,|L_iM'\rangle \\
&= (-1)^{2\ell}\sum_{M'q}\langle L_iM'\ell q|L_fM\rangle\,\left\langle\psi_{L_f}Y_{L_fM}\right|\beta_\ell r^\ell Y_{\ell q}\,|\psi_{L_i}Y_{L_iM'}\rangle \\
&= (-1)^{2\ell}\sum_{M'q}\langle L_iM'\ell q|L_fM\rangle\,\left\langle\psi_{L_f}\right|\beta_\ell r^\ell\,|\psi_{L_i}\rangle\,\left\langle Y_{L_fM}\right|Y_{\ell q}\,|Y_{L_iM'}\rangle \\
&= (-1)^{2\ell}\sum_{M'q}\langle L_iM'\ell q|L_fM\rangle\,\left\langle\psi_{L_f}\right|\beta_\ell r^\ell\,|\psi_{L_i}\rangle\,\langle L_iM'\ell q|L_fM\rangle\,\langle L_f||Y_\ell||L_i\rangle \\
&= \left\langle\psi_{L_f}\right|\beta_\ell r^\ell\,|\psi_{L_i}\rangle\,\langle L_f||Y_\ell||L_i\rangle \\
&= \left[\frac{(2L_i+1)(2\ell+1)}{4\pi(2L_f+1)}\right]^{1/2}\langle L_i0\ell0|L_f0\rangle\,\left\langle\psi_{L_f}\right|\beta_\ell r^\ell\,|\psi_{L_i}\rangle
\end{aligned} \tag{3.2.6}$$

where the definition of the core-cluster relative motion wavefunction has been used (equation 2.1.2), the completeness relation of Clebsch-Gordan coefficients, and the integral over spherical harmonics have been calculated explicitly in the last step.

The reduced transition probability for electric multipole transitions between arbitrary states can then be written as

$$B(E\ell; L_i \to L_f) = \frac{1}{4\pi}\beta_\ell^2\hat{\ell}^2\,|\langle L_i0\ell0|L_f0\rangle|^2\,\left|\left\langle\psi_{L_f}\right|r^\ell\,|\psi_{L_i}\rangle\right|^2. \tag{3.2.7}$$

3.2.4 Single Particle Value (Weisskopf Units)

It is important to note that both the transition probability and the reduced transition probability have units. The transition probability (equation 3.1.20) is measured in number of decays per unit time, while the reduced transition probability for electric multipole transitions (equation 3.2.7) is measured in $e^2fm^{2\ell}$. In order to gain some feeling of the magnitude of reduced transition probabilities, a standard unit is introduced, called the Weisskopf Unit (W.u.).

An estimate of the nuclear wavefunction is obtained by decomposing the single-particle wavefunction into three parts; a radial wavefunction, an orbital angular momentum part and an intrinsic spin part. As an estimate to the reduced transition probability for $E\ell$ transitions, the radial dependence is taken to be determined by the value of ℓ, to first order, while the angular momentum dependence is taken on average to be about $1/4\pi$, since the total solid angle about a point is 4π steradians. The Weisskopf single-particle estimate for the ℓ^{th} multipole reduced electric transition probability is then used to convert from $e^2fm^{2\ell}$ to W.u. [27],

$$1 \quad W.u. = \frac{1}{4\pi}\left(\frac{3}{\ell+3}\right)^2(1.2)^{2\ell}A^{2\ell/3} \quad e^2fm^{2\ell}. \tag{3.2.8}$$

3.3 Exotic Decay Half-Life

The emission of a heavy ion from a nucleus is easily exhibited within the BCM, by simply identifying the emitted ion as the cluster and the remaining nucleons as the core. This emission of a heavy ion is referred to as exotic decay and has been observed experimentally for several actinide nuclei [2, 3].

This type of emission, as all emissions of quanta of radiation, is identified with a certain probability, or decay width, and has a certain half-life. The decay half-life of an element is defined as the time taken to halve the number of radioactive elements, and can be expressed as

$$T_{1/2} = \frac{\hbar \ln 2}{\Gamma}. \tag{3.3.1}$$

The decay width Γ of an isolated state for a single particle in one dimension was found by Gamow [32] to have the simple form $\Gamma = A \exp[-S/\hbar]$ in the quasiclassical limit, where A is a prefactor and S is the action for the classically forbidden region. Gurvitz and Kalbermann spent a considerable amount of effort in obtaining a general formula that embodies Gamow's quasiclassical result, and finding an approximation comparable to the Gamow formula, of which the main points are repeated here [33, 34].

The problem of finding an expression for the decay width starts by describing the quasistationary state. The quasistationary state can be approached as a resonance in a scattering amplitude, of which the decay width is calculated as the width of the corresponding resonance.

The quasistationary state arises as a process starting with a free wave at infinity, impinging on a potential that distorts the wave, eventually trapping it in a quasibound state for a sizable amount of time for the decay to occur. Alternatively, the process can start with a pure bound state, and a perturbation excites the wavefunction into the continuum, creating a quasibound state.

Consider a potential $V(r) = U(r) + W(r)$ of any shape, with properties $U(r) = V(r)$ for $r \leq R$, $U(r) = V_0$ for $r \geq R$ and $W(r) = 0$ for $r \leq R$, $W(r) = V(r) - V_0$ for $r \geq R$ (figure 3.1).

This potential has a bound state $\Phi_0(r)$ as an eigenstate of the Hamiltonian $H_0 = -\frac{\hbar^2}{2m}\nabla^2 + U(r)$ with eigenvalue $E_0 < V_0$,

$$H_0\Phi_0(r) = E_0\Phi_0(r)$$

for simplicity, consider H_0 to contain only one bound state, $\Phi_0(r)$.

At a time $t = 0$, the distorting potential $W(r)$ is turned on, such that the state $\Phi_0(r)$ is no longer an eigenstate of the full Hamiltonian, $H = H_0 + W(r)$. The wavefunction can now be written as a wave packet, spread out in time, and expanded as separate bound state and continuum wavefunctions,

$$\Phi_0(r,t) = b_0(t)e^{-iE_0t/\hbar}\Phi_0(r) + \int \frac{d^3k}{(2\pi)^3} b_k(t)e^{-iE_kt/\hbar}\Phi_k(r) \tag{3.3.2}$$

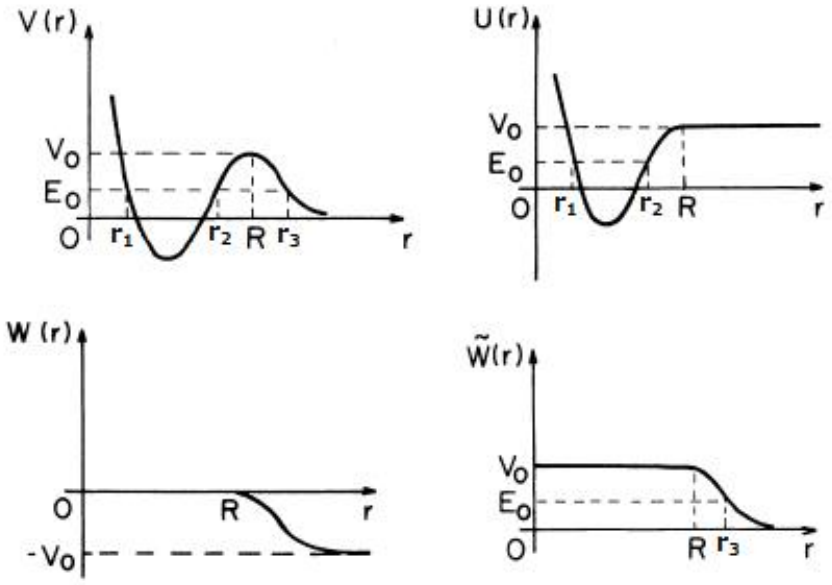

Figure 3.1: The potentials $V(r)$, $U(r)$, $W(r)$ and $\tilde{W}(r) = W(r) + V_0$. r_1, r_2 and r_3 are the classical turning points and E_0 is the energy of the bound state [33].

where the continuum wavefunctions $\Phi_k(r)$ are eigenstates of H_0 with $E_k = V_0 + \frac{\hbar^2 k^2}{2m}$, and the coefficients $b_0(t)$ and $b_k(t)$ can be considered as probability amplitudes when squared. The initial condition is taken as $b_0(0) = 1$ and $b_k(0) = 0$, such the system starts in a pure bound state.

When inserting the wavefunction $\Phi_0(r,t)$ into the time-dependent Schrödinger equation, the standard equations of time-dependent perturbation theory is obtained,

$$\begin{aligned} i\hbar\frac{db_0(t)}{dt} &= b_0(t)\langle\Phi_0|W|\Phi_0\rangle + \int \frac{d^3k}{(2\pi)^3} b_k(t) e^{i(E_0-E_l)t/\hbar}\langle\Phi_0|W|\Phi_0\rangle \\ i\hbar\frac{d\tilde{b}_k(t)}{dt} &= b_0(t)\langle\Phi_k|W|\Phi_0\rangle e^{i(E_k-V_0-E_0)t/\hbar} \\ &\quad + \int \frac{d^3k'}{(2\pi)^3}\tilde{b}_{k'}(t) e^{i(E_k-E_{k'})t/\hbar}\langle\Phi_k|\tilde{W}|\Phi_{k'}\rangle \end{aligned} \tag{3.3.3}$$

where the potential $\tilde{W}(r) = W(r) + V_0$ has been introduced since the continuum-to-continuum transition matrix element $\langle\Phi_k|W|\Phi_{k'}\rangle$ generates singular pieces due to the fact that $W(r) \to -V_0$ as $r \to \infty$. The new potential $\tilde{W}(r)$ vanishes for $r \to \infty$ (figure 3.1). The additional coefficient $\tilde{b}_k(t) = \exp[-iV_0 t/\hbar] b_k(t)$ has also been introduced.

The probability of finding the system in its initial state, $|b_0(t)|^2$ decreases in time, and a resonance state is obtained if, for large t, it drops as $\exp[-\Gamma t/\hbar]$.

These integro-differential equations can be solved exactly by applying the

Laplace-transformation, $b(\epsilon) = \int_0^\infty b(t) \exp[i\epsilon t/\hbar]$,

$$\begin{aligned} -i\hbar + \epsilon b_0(\epsilon) &= W_{00} b_0(\epsilon) + \int \frac{d^3k}{(2\pi)^3} W_{0k} \tilde{b}_k(\epsilon) \\ \epsilon_k \tilde{b}_k(\epsilon_k) &= W_{k0} b_0(\epsilon) + \int \frac{d^3k'}{(2\pi)^3} \tilde{W}_{kk'} \tilde{b}_{k'}(\epsilon_{k'}) \end{aligned} \tag{3.3.4}$$

where $W_{kk'} = \langle \Phi_k | W | \Phi_{k'} \rangle$ and $\epsilon_k = \epsilon + E_0 + V_0 - E_k$. These equations can be combined by iteration,

$$\begin{aligned} -i\hbar + \epsilon b_0(\epsilon) = W_{00} b_0(\epsilon) &+ \int \frac{d^3k}{(2\pi)^3} W_{0k} \frac{1}{\epsilon_k} W_{k0} b_0(\epsilon) \\ &+ \int \frac{d^3k}{(2\pi)^3} \int \frac{d^3k'}{(2\pi)^3)} W_{0k} \frac{1}{\epsilon_k} \tilde{W}_{kk'} \frac{1}{\epsilon_k} W_{k'0} b_0(\epsilon) + \cdots \end{aligned} \tag{3.3.5}$$

where higher order terms are neglected. This series can be simplified by introducing the Green's function $\tilde{G} = \tilde{G}_0 + \tilde{G}_0 \tilde{W} \tilde{G}$,

$$-i\hbar + \epsilon b_0(\epsilon) = (\langle \Phi_0 | W | \Phi_0 \rangle + \langle \Phi_0 | W \tilde{G} W | \Phi_0 \rangle) b_0(\epsilon) \tag{3.3.6}$$

where

$$\tilde{G}_0 = \sum_k \frac{|\Phi_k\rangle \langle \Phi_k|}{\epsilon_k} \tag{3.3.7}$$

such that the integral in equation (3.3.5) has been changed to a sum over discrete values of k.

From equation (3.3.6),

$$b_0(\epsilon) = \frac{i\hbar}{\epsilon - \langle \Phi_0 | W | \Phi_0 \rangle + \langle \Phi_0 | W \tilde{G} W | \Phi_0 \rangle} \tag{3.3.8}$$

a solution for $b_0(t)$ can be found by performing the inverse Laplace-transformation,

$$b_0(t) = \frac{1}{2\pi} \int_{\mathcal{C}} d\epsilon e^{-i\epsilon t/\hbar} b_0(\epsilon)$$

which requires an integration over the complex plane and consideration of the contributions from singularities of $b_0(\epsilon)$ [35]. If $b_0(\epsilon)$ has a pole at $\epsilon = \epsilon_0$, $b_0(t)$ falls off exponentially with t, i.e. $b_0(t) \sim \exp[-\Gamma/2\hbar t]$ where $\Gamma = -2Im(\epsilon_0)$. The value of ϵ_0 is then given by

$$\epsilon_0 = \langle \Phi_0 | W | \Phi_0 \rangle + \langle \Phi_0 | W \tilde{G}(\epsilon_0) W | \Phi_0 \rangle \tag{3.3.9}$$

which can be simplified by expanding $|\Phi_0\rangle$ in partial waves, remembering that this is a one-dimensional problem. Equation (3.3.9) for spherical symmetric potentials, in terms of the radial wave functions is then given by

$$\epsilon_0 = \int_R^\infty |\varphi_0(r)|^2 W(r) dr + \int_R^\infty r dr \int_R^\infty r' dr' \varphi_0(r) W(r) \tilde{G}(E, r, r') W(r') \varphi_0(r') \tag{3.3.10}$$

where $E = E_0 + \epsilon_0$ and the lower limit of the integrals are R since $W(r) = 0$ for $r \leq R$. This expression is still exact, since no assumptions about the particular form of the potential or wavefunctions have been made, but in order to find a simple expression for the decay width in the quasiclassical limit, approximations to the Green's function and the wavefunctions will have to be made.

The first approximation is for the Green's function in equation (3.3.10), by $G_{\tilde{W}}$,

$$G_{\tilde{W}} = \left(E + \frac{\hbar^2 \nabla^2}{2m} - \tilde{W} \right)^{-1} \tag{3.3.11}$$

which, intuitively, can be understood by considering the contribution of non-resonant wavefunctions. The projection operator $\sum_k |\Phi_k\rangle \langle \Phi_k|$ is the only difference between $\tilde{G}_0$ and the total Green's function $G(E) = (E + \frac{\hbar^2 \nabla^2}{2m} - V(r))^{-1}$, but this contribution can be neglected in the outer region $(r, r' \geq r_3)$ due to the exponential falloff of the wavefunctions. In the inner region, $(r, r' \leq r_3)$, the projection operator excludes all bound states, and therefore only nonresonant wavefunctions are present and the contribution of the inner region is negligible, allowing the approximation of $\tilde{G}$ by $G_{\tilde{W}}$.

The Green's function $G_{\tilde{W}}$ can be represented as

$$G_{\tilde{W}}(E_0, r, r') = -\frac{2m}{\hbar^2 r r' k} \chi_k^{(+)}(r_>) \chi_k(r_<) \tag{3.3.12}$$

where χ_k is the regular (incoming) and $\chi_k^{(+)}$ is the irregular (outgoing) eigenstate of the Hamiltonian $(-\frac{\hbar^2 \nabla^2}{2m} + \tilde{W}(r))$. Approximating the Green's function $\tilde{G}$ in equation (3.3.10) with this equation for $G_{\tilde{W}}$, the result obtained is

$$\begin{aligned} \epsilon_0 = \int_R^\infty |\varphi_0(r)|^2 W(r) dr - \frac{2m}{\hbar^2 k} \int_R^\infty dr \int_R^r dr' \varphi_0(r) W(r) \chi_k^{(+)}(r) \chi_k(r') W(r') \varphi_0(r') \\ + \frac{2m}{\hbar^2 k} \int_R^\infty dr \int_r^\infty dr' \varphi_0(r) W(r) \chi_k(r) \chi_k^{(+)}(r') W(r') \varphi_0(r') \end{aligned} \tag{3.3.13}$$

of which the integrals over r, r' can be carried out analytically without any approximations. This is done by using the relation

$$\varphi_0(r) = \varphi_0(R) e^{-\alpha(r-R)} \quad , \quad r \geq R$$

where $\alpha = \frac{1}{\hbar}\sqrt{2m(V_0 - E_0)}$. Further, since χ_k and $\chi_k^{(+)}$ are eigenfunctions of the Schrödinger equation with $\tilde{W}(r) = W(r) + V_0$,

$$W(r)\chi_k(r) = \left(E_0 - V_0 + \frac{\hbar^2}{2m} \frac{d^2}{dr^2} \right) \chi_k(r)$$

with the same relation valid for $\chi_k^{(+)}(r)$. Integrating by parts yields the useful result

$$\int_a^b e^{-\alpha r} W(r) \chi_k(r) dr = e^{-\alpha r} \frac{\hbar^2}{2m} \left[\alpha \chi_k(r) + \chi_k'(r) \right]_a^b \tag{3.3.14}$$

which, when placed into equation (3.3.13) and carrying out the r' integration,

$$\begin{aligned}\epsilon_0 = |\varphi_0(R)|^2 e^{2\alpha R}[& \int_R^\infty e^{-2\alpha r} W(r) dr \\ & + \frac{e^{-\alpha R}}{k}[\alpha\chi_k(R) + \chi_k^{'}(R)] \int_R^\infty e^{-\alpha r} W(r) \chi_k^{(+)}(r) dr \\ & + \frac{1}{k}\int_R^\infty e^{-2\alpha r} W(r)[\chi_k(r)\chi_k^{(+)'}(r) - \chi_k^{'}(r)\chi_k^{(+)}(r)]dr].\end{aligned} \tag{3.3.15}$$

The third integral cancels exactly with the first when using the asymptotic forms of $\chi_k(r)$ and $\chi_k^{(+)}(r)$, which can be calculated in a similar way to equations (2.2.9, 2.2.10)

$$\chi_k(r) \to \sin[kr + \delta_\ell]$$

and

$$\chi_k^{(+)}(r) \to \exp[i(kr + \delta_\ell)]$$

where δ_ℓ is the phase shift, to obtain the relation

$$\chi_k(r)\chi_k^{(+)'}(r) - \chi_k^{'}(r)\chi_k^{(+)}(r) = -k$$

while the second integral, when using equation (3.3.14) and integrating over r,

$$\epsilon_0 = -\frac{\hbar^2}{2mk}|\varphi_0(R)|^2[\alpha\chi_k(R) + \chi_k^{'}(R)][\alpha\chi_k^{(+)}(R) + \chi_k^{(+)'}(R)] \tag{3.3.16}$$

which is the final result for the energy shift and decay width. This equation is just a product of the bound state and the resonant scattering state wavefunctions.

Since $Im\chi_k^{(+)} = \chi_k$ and $\Gamma = -2Im(\epsilon_0)$,

$$\Gamma = \frac{\hbar^2}{mk}\left|\varphi_0[\alpha\chi_k(R) + \chi_k^{'}(R)]\right|^2. \tag{3.3.17}$$

Noticing that $\chi_k(r) = \chi_k(R)e^{\alpha(r-R)}$ for $r \leq R$, since $\tilde{W}(r) = V_0$ for $r \leq R$,

$$\chi_k^{'}(R) = \alpha\chi_k(R)$$

which, when inserted into equation (3.3.17), gives the simple expression for the decay width,

$$\Gamma = \frac{4\hbar^2\alpha^2}{mk}|\varphi_0(R)\chi_k(R)|^2 \tag{3.3.18}$$

which seems dependent on R, but the exact result for Γ, obtained from equation (3.3.9), is independent of R, and therefore the R dependence of equation (3.3.18) must be weak. This is essential, since this equation is derived without specific knowledge of the potential, and R itself will depend on the particular shape of the potential.

The next step is to apply a quasiclassical approximation to equation (3.3.18) in order to get rid of the wavefunctions $\varphi_0(R)$ and $\chi_k(R)$.

Firstly, consider the quasiclassical limit for the scattering wavefunction, $\chi_k(r)$, which is an eigenstate of the Hamiltonian $(-\frac{\hbar^2\nabla^2}{2m}+\tilde{W}(r))$. In the region $R \leq r \leq r_3$, the wavefunction can be written as (equations 2.2.9, 2.2.10)

$$\chi_k(r) = \frac{\sqrt{k}}{2\sqrt{|p(r)|}} \exp\left[-\int_r^{r_3} |p(r')|dr'\right] \tag{3.3.19}$$

where $p(r) = \frac{1}{\hbar}[2m(E_0 - \tilde{W}(r))]^{1/2}$ and the factor $\sqrt{k} = (\frac{2m}{\hbar^2}E_0)^{1/4}$ provides the correct asymptotic limit for $\chi_k(r)$ as $r \to \infty$. The corresponding irregular (outgoing) wavefunction $\chi_k^{(+)}(r)$ in the region $R \leq r \leq r_3$ can then be written as

$$\chi_k^{(+)}(r) = \frac{\sqrt{k}}{\sqrt{|p(r)|}} \exp\left[\int_r^{r_3} |p(r')|dr'\right] \tag{3.3.20}$$

with the same relations for both $p(r)$ and k valid.

Secondly, consider the quasiclassical approximation to the bound-state wavefunction $\varphi_0(r)$,

$$\varphi_0(r) = \frac{\sqrt{N}}{2\sqrt{|p(r)|}} \exp\left[-\int_{r_2}^{r} |p(r')|dr'\right] \tag{3.3.21}$$

for $r > r_2$, with N a quasiclassical normalization factor. For high-lying states, the normalization can be approximated by neglecting the contribution from the classically forbidden regions, $r < r_1$ and $r > r_2$, and, using the quasiclassical form of the wavefunction (equation 2.2.11),

$$\frac{1}{N} = \frac{1}{2}\int_{r_1}^{r_2} \frac{1}{p(r)}dr. \tag{3.3.22}$$

Substituting equations (3.3.19 - 3.3.22) into equation (3.3.18) then gives the final result for the decay width,

$$\Gamma = \frac{\hbar^2}{2m} \frac{\exp\left[-2\int_{r_2}^{r_3} |p(r)|dr\right]}{\int_{r_1}^{r_2} \frac{1}{p(r)}dr}$$

where $p(r) = \sqrt{\frac{2m}{\hbar^2}(E_0 - V(r))}$ with E_0 the energy of the bound state. Note that this equation does not depend on the particular decomposition of $V(r) = U(r) + W(r)$ and therefore it is independent of R, as the initial result indicated.

As a final step, within the BCM, the decay width is taken to be subject to a certain pre-formation probability P, defined as the probability for a certain core-cluster decomposition to form within the parent nucleus. Exotic decay is

then easily exhibited; a parent nucleus is taken to be decomposed into some core-cluster pair with probability P which interact via some central potential $V(r)$, and the decay width of emitting the cluster is given by the expression

$$\Gamma = P\frac{\hbar^2}{2m}\frac{\exp\left[-2\int_{r_2}^{r_3}|p(r)|dr\right]}{\int_{r_1}^{r_2}\frac{1}{p(r)}dr} \tag{3.3.23}$$

with the decay half-life obtained with the use of equation (3.3.1).

Chapter 4

Cluster Size

A great advantage of the BCM is that the emission of a heavy ion, or exotic decay, is very easily exhibited. By identifying the emitted nucleus as the cluster, and the remaining nucleons as the core, several experimentally obtained data, such as decay half-lives, energy spectra and reduced electromagnetic transitions, have been reproduced to good accuracy using the Woods-Saxon and Woods-Saxon Cubed potential of equation (2.1.9) [22, 23, 36, 37, 38].

A problem in applying the BCM to heavy particle clustering and exotic decay, however, is the choice of core and cluster. Where experimental decay data is available, it will always serve as a good guide, but since very few cases of exotic decay have been observed, experimental data is mostly lacking, and therefore a different method needs to be developed in order to make the choice of core and cluster and further extend the range of applications of the BCM.

4.1 Stability Criterion

We investigate here the hypothesis that a good guide in choosing core and cluster sizes are the binding energies of the two components. The most favoured combination will then be if the parent can divide into a cluster and core which are both doubly magic. In general, this is not always possible, so the most likely core-cluster decomposition will then be if both cluster and core are singly magic, or at least one of them doubly- or singly magic [39].

There may be instances when this type of core-cluster decomposition will not be the favoured one, especially if choosing either the cluster or core as doubly magic results in the other body being very loosely bound. Nevertheless, this method of choosing the core and cluster seems like a good starting point in finding favoured core-cluster decompositions.

In general, the most tightly bound nuclei are found by determining the charge and mass values (Z, A) which maximize the difference:

$$D = B_A - B_L \tag{4.1.1}$$

between the actual binding energy B_A and some smoothly varying average value B_L obtained from a liquid-drop mass formula (figure 4.1).

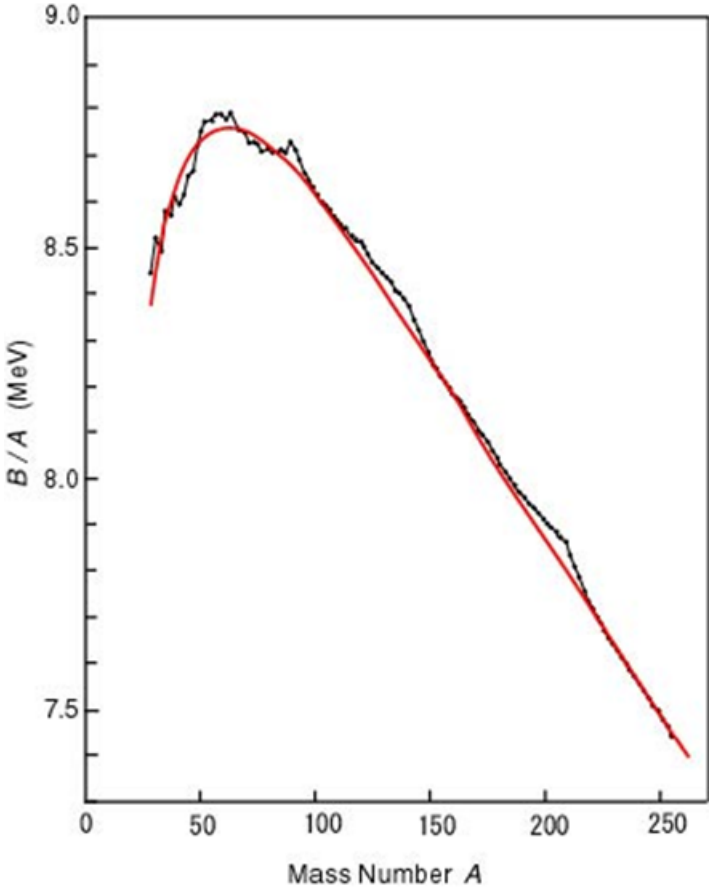

Figure 4.1: The liquid-drop model estimate of experimentally measured binding energies shows the difference between the actual binding energy (black) and the liquid-drop model estimate (red). The greater differences occur where the nuclei are doubly magic. [40].

Within the BCM, the partition of a nucleus with fixed (Z_T, A_T) into various possible pairs of nuclides with charge and mass values (Z_1, A_1) and (Z_2, A_2) are considered. The decomposition which gives the largest summed differences between the actual binding energies and calculated liquid drop binding energies of the core and cluster will then be the most likely candidate for a core-cluster pair [29, 39].

This involves finding the partition $(Z_T, A_T) \rightarrow (Z_1, A_1) + (Z_2, A_2)$ which maximizes the expression

$$D(Z_1, A_1, Z_2, A_2) = [B_A(Z_1, A_1) - B_L(Z_1, A_1)] + [B_A(Z_2, A_2) - B_L(Z_2, A_2)] \tag{4.1.2}$$

Only even-even (Z_T, A_T), (Z_1, A_1) and (Z_2, A_2) are considered when computing the difference for core-cluster decompositions. This is because even-even nuclei are more tightly bound than even-odd or odd-odd nuclei and it is assumed that the nucleus will prefer to be in a nuclear state involving the most tightly bound core and cluster structure.

The current version of the liquid-drop formula, also known as the Semi-Empirical Mass Formula (SEMF), for even-even nuclei is used [41]:

$$B_L = a_v A - a_s A^{2/3} - a_c \frac{Z(Z-1)}{A^{1/3}} - a_a \frac{(A-2Z)^2}{A} + \frac{a_p}{A^{1/2}} \tag{4.1.3}$$

where

$$\begin{aligned} a_v &= 15.56\,\text{MeV} \\ a_s &= 17.23\,\text{MeV} \\ a_c &= 0.697\,\text{MeV} \\ a_a &= 23.285\,\text{MeV} \\ a_p &= 12\,\text{MeV} \end{aligned} \tag{4.1.4}$$

By selecting a certain set of clusters, determined from the experimentally observed emitted heavy ions, the core corresponding to each cluster in the considered Th isotopes can be determined, and the corresponding value of D can be calculated. These results are shown in figure (4.2).

The first set of maxima in figure (4.2) show the importance of α-clustering in heavy nuclei which leads to α-decay. Of more interest in the present study, is the second maximum appearing, indicating the likely existence of exotic clustering in these nuclei. These maxima are indicated by arrows, and shift towards heavier clusters for heavier isotopes. For lighter isotopes, such as $^{222,224}Th$, the maximum is obtained at ^{14}C, while for a heavier isotope, like ^{228}Th, the maximum is obtained for a ^{20}O cluster.

4.2 Dipole Constraint

The stability criterion method requires *a priori* choices of which cluster masses and charges to consider and is therefore not useful for cases in which no exotic decay data is available. A more general approach is therefore needed where only the total charge and mass, (Z_T, A_T), are required in addition to readily available mass tables and equation (4.1.2) [29].

The extra input employed stems from the experimental observation that electric dipole transitions in heavy nuclei are very weak, i.e. $B(E1; 1^- \rightarrow 0^+) \approx 0$. The reduced transition probability, for a transition between states of opposite parity, and with $\ell = 1$, i.e. from $J^\pi = 1^-$ to $J^\pi = 0^+$, is given by (Section 3.2)

$$B(E1; 1^- \rightarrow 0^+) = \frac{1}{4\pi} \left| \beta_1 \int_0^\infty \psi_0^*(r) r \psi_1(r) dr \right|^2$$

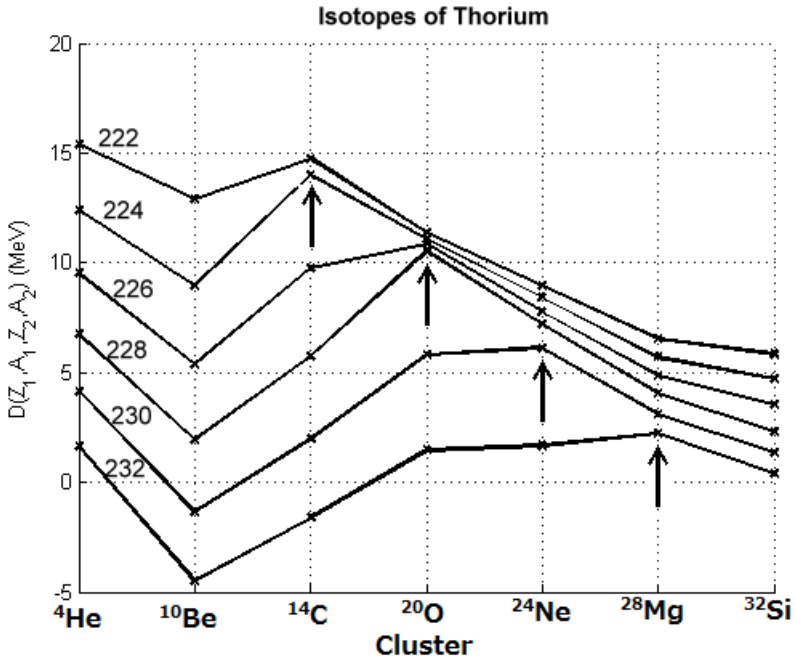

Figure 4.2: Calculations of $D(Z_1, A_1, Z_2, A_2)$ using equation (4.1.2) for different isotopes of Th, restricted to clusters seen in exotic decay of actinide nuclei, and additionally ^{10}Be. The maxima are indicated by an arrow. The values for $^{222-232}Th$ have been shifted vertically by $2MeV$ for greater clarity. Note the increase of cluster charge predicted for increase in isotope mass.

where the charge factor is given by

$$\beta_1 = Z_1\left(-\frac{A_2}{A}\right) + Z_2\left(\frac{A_1}{A}\right) \tag{4.2.1}$$

The near vanishing of these reduced matrix elements require that $\beta_1 \to 0$, so to good approximation

$$\frac{Z_1}{A_1} = \frac{Z_2}{A_2} = \frac{Z_T}{A_T} \tag{4.2.2}$$

and

$$\frac{N_1}{A_1} = \frac{N_2}{A_2} = \frac{N_T}{A_T}. \tag{4.2.3}$$

Within the cluster model, any plausible core-cluster decomposition has to satisfy the dipole constraint (equations 4.2.2, 4.2.3). If the charge condition is exactly satisfied by some single choice of cluster, the neutron number constraint would follow, but this is not possible in general. However, by considering the nuclear state to be a mixture of several possible cluster partitions, it becomes possible that the dipole constraint can be satisfied exactly [29].

4.2.1 Cluster Isotopes

Firstly, the nucleus (Z_T, A_T) is considered to consist of a mixture of two core-cluster configurations where the clusters are neighbouring isotopes. This is achieved by selecting a specific cluster charge Z_2 and finding the corresponding cluster mass A_2 such that

$$\frac{A_2}{Z_2} \leq \frac{A_T}{Z_T} \leq \frac{(A_2+2)}{Z_2} \tag{4.2.4}$$

and then assigning probabilities $p(A_2)$ and $p(A_2+2)$ to the two isotopic masses, with their sums equal to unity. The probabilities are calculated from

$$p(A_2) + p(A_2+2) = 1 \tag{4.2.5}$$

and

$$p(A_2)\left(\frac{Z_2}{A_2}\right) + p(A_2+2)\left(\frac{Z_2}{A_2+2}\right) = \frac{Z_T}{A_T} \tag{4.2.6}$$

such that the dipole constraint is satisfied exactly.

The mean cluster mass can be calculated as

$$\bar{A}_2 = \frac{A_T Z_2}{Z_T}$$

and mean neutron number as

$$\bar{N}_2 = \frac{N_T Z_2}{Z_T}.$$

The weighted average $\bar{D}(1,2) = \bar{D}(Z_1, A_1, Z_2, A_2)$ can then be calculated according to

$$\bar{D}(1,2) = p(A_2)D(Z_1, A_1, Z_2, A_2) + p(A_2+2)D(Z_1, A_1-2, Z_2, A_2+2). \tag{4.2.7}$$

4.2.2 Cluster Isotones

A similar procedure can also be applied to mixtures of adjacent cluster isotones. By choosing particular values of N_2, the cluster mass A_2 can be found such that

$$\frac{A_2}{N_2} \leq \frac{A_T}{N_T} \leq \frac{(A_2+2)}{N_2}. \tag{4.2.8}$$

The probabilities assigned to each cluster isotone, $p(A_2)$ and $p(A_2+2)$, are then calculated from

$$p(A_2) + p(A_2+2) = 1 \tag{4.2.9}$$

and

$$p(A_2)\left(\frac{N_2}{A_2}\right) + p(A_2+2)\left(\frac{N_2}{A_2+2}\right) = \frac{N_T}{A_T} \tag{4.2.10}$$

such that the weighted average $\bar{D}(1,2) = \bar{D}(Z_1, A_1, Z_2, A_2)$ can be calculated according to

$$\bar{D}(1,2) = p(A_2)D(Z_1, A_1, Z_2, A_2) + p(A_2+2)D(Z_1-2, A_1-2, Z_2+2, A_2+2) \tag{4.2.11}$$

The mean mass, in order to ensure that the dipole condition is fulfilled, is then given by

$$\bar{A}_2 = \frac{A_T N_2}{N_T}$$

and the mean charge

$$\bar{Z}_2 = \frac{Z_T N_2}{N_T}.$$

The results obtained in figure (4.4) using the dipole constraint method (red and green crosses), show a maximum near $\bar{Z}_2 = 8.5$, consistent with the cluster choice of ^{20}O as was made earlier. This method, however, can only calculate the weighted average $\bar{D}(1,2)$ for certain values of the mean cluster charge, and not arbitrary values. Therefore the method needs to be expanded in order to calculate the maximum of $\bar{D}$ for any arbitrary cluster charge.

4.3 Full Calculation

The idea behind this development is to be able to choose any arbitrary mean value for the plotting parameter, $\bar{Z}_2$, and find the weighted combinations of clusterings which satisfy the dipole rule [29]. In a similar way to considering the nucleus consisting of a mixture of two core-cluster decompositions, the nucleus is now considered to consist of up to four core-cluster decompositions, where the clusters are neighbouring isotopes and isotones.

This is done by selecting some arbitrary value of the mean charge, $\bar{Z}_2$. The corresponding mean neutron number is then given by

$$\bar{N}_2 = \frac{N_T \bar{Z}_2}{Z_T}. \tag{4.3.1}$$

Given the values of $\bar{Z}_2$ and $\bar{N}_2$, the clusters are determined by finding the values which bracket the mean values, i.e.

$$\begin{aligned} Z_2 \geq \bar{Z}_2 \geq Z_2 - 2 \\ N_2 \geq \bar{N}_2 \geq N_2 - 2 \end{aligned} \tag{4.3.2}$$

with weighting probabilities

$$\begin{aligned} p(Z_2) &= (1/2)[\bar{Z}_2 - (Z_2 - 2)], \\ p(Z_2 - 2) &= (1/2)[Z_2 - \bar{Z}_2]. \\ p(N_2) &= (1/2)[\bar{N}_2 - (N_2 - 2)], \\ p(N_2 - 2) &= (1/2)[N_2 - \bar{N}_2] \end{aligned} \tag{4.3.3}$$

The nucleus is now considered to be a superposition of up to four different cluster configurations with weights being products of the above probabilities. Neighbouring cluster isotopes and isotones are selected as the superposition states in order to ensure that the dipole constraint is satisfied exactly, with the corresponding mean cluster charge used as a plotting parameter and to determine the most likely single core-cluster decomposition.

The weighted average $\bar{D}(1,2)$ can now be calculated according to

$$\bar{D}(\bar{Z}_2, \bar{N}_2) = \sum_{Z_2,N_2} p(Z_2)p(N_2)D(Z_2, N_2) \tag{4.3.4}$$

with the value of $\bar{Z}_2$ corresponding to the maximum $\bar{D}$ being the mean cluster charge. This value of $\bar{Z}_2$ will then establish the core-cluster decomposition of the nucleus which can be used to calculate several structure observables, such as energy spectra, decay half-lives and reduced transition probabilities.

The result of plotting this $\bar{D}(\bar{Z}_2, \bar{N}_2)$ against $\bar{Z}_2$ for ^{226}Th is shown in figure (4.3), and for ^{228}Th in figure (4.4), as the solid black line. The points representing the binding energies for the isotopic and isotonic pairs considered earlier fall exactly on the calculated line, since these points correspond to the case when $\bar{Z}_2$ or $\bar{N}_2$ are even integers, and one of the weights in equation (4.3.3) becomes zero, reducing the four possibilities to two.

For ^{228}Th, a single maximum is clear at around $Z_2 = 8.5$ (figure 4.4), but for ^{226}Th (figure 4.3), the full calculation produces two maxima, and it is unclear which of the two would be the correct choice for Z_2. This example serves as motivation to introduce an averaging scheme in order to eliminate multiple maxima and only find one true maximum, which will correspond to the mean cluster charge.

4.4 Smoothed Calculation

Since some isotopes may have two peaks for $\bar{D}$ lying close together (figure 4.3), a method needs to be developed to find a smooth curve to establish where the most likely mean cluster charge is.

This is done by computing the average of a number of points surrounding a particular mean cluster charge. Firstly, the full calculation is computed for 1000 different mean cluster charges within the interval $Z_2 = 4$ and $Z_2 = 18$. The smoothed calculation for a specific Z_2 can then be computed by taking the average over 100 calculated $\bar{D}$ values, corresponding to the 50 mean cluster charges smaller and greater than the Z_2 in question. This calculation is done for all mean cluster charges, and the resultant average $\bar{D}$ values are plotted.

In doing this, only one maximum $\bar{D}$ will appear, with the corresponding Z_2 used as the mean cluster charge. For ^{226}Th (figure 4.3), the blue line represents the smoothed curve. It is clearly visible that the previous problem

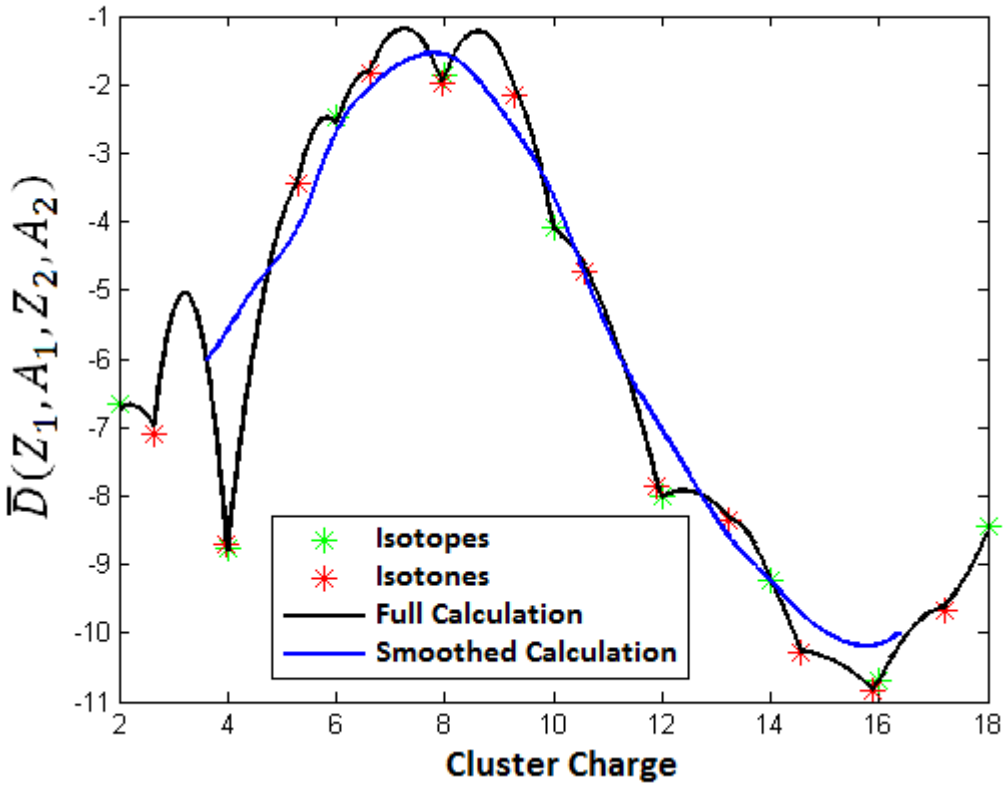

Figure 4.3: Calculations of $\bar{D}(Z_1, A_1, Z_2, A_2)$ as a function of cluster charge for ^{226}Th. Isotopes are indicated with green crosses, isotones with red crosses and the full calculation is indicated with the black line. A smoothed calculation is indicated with a blue line.

of two maxima have now disappeared, and only one maximum, around $Z_2 = 8$ is visible.

For ^{228}Th (figure 4.4), the smoothed curve gives a very similar maximum to that of the full calculation, around $Z_2 = 8.5$. This is a good indication that taking averages over a number of cluster charges does not influence the most likely cluster charge, but only smoothes the curve out, and should the full calculation provide two maxima, the average will only produce one.

Figure (4.5) shows all the smoothed calculation curves for $^{222-232}Th$ isotopes. The maximum of each curve seems to shift towards heavier clusters for increasing isotope mass, as was seen earlier, in figure (4.2).

4.5 Extended Calculation

By utilizing the dipole constraint and considering the nucleus to consist of a mixture of up to four different core-cluster decompositions, with weighting

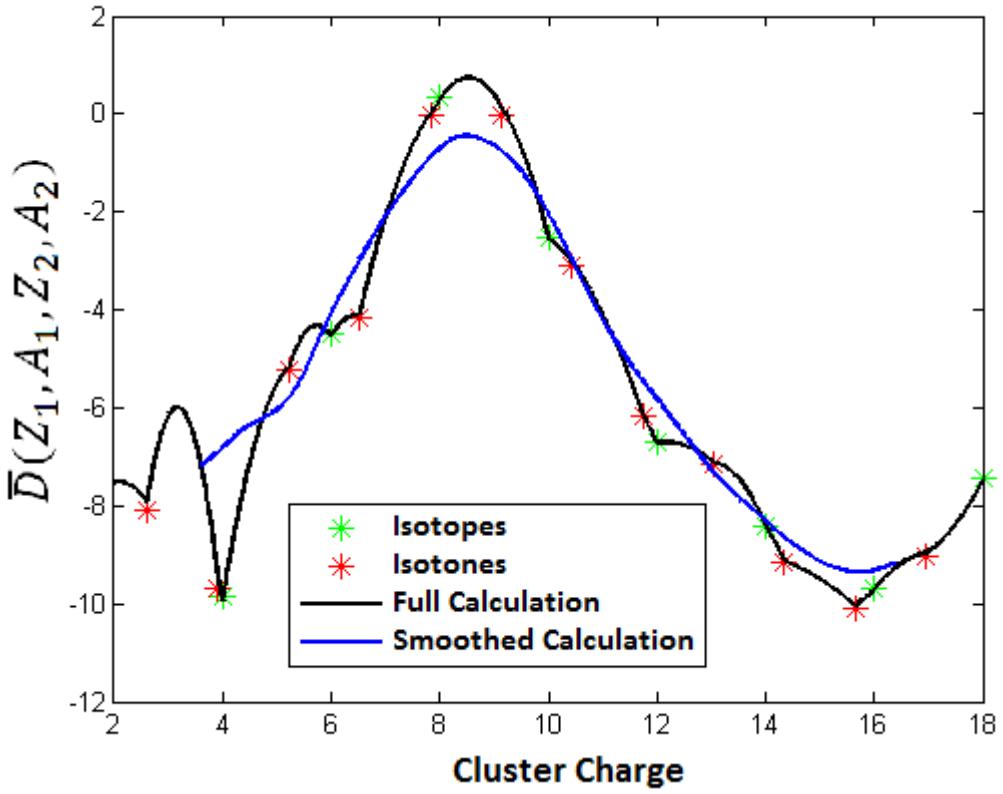

Figure 4.4: Calculations of $\bar{D}(Z_1, A_1, Z_2, A_2)$ as a function of cluster charge for ^{228}Th. Isotopes are indicated with green crosses, isotones with red crosses and the full calculation is indicated with the black line. A smoothed calculation is indicated with a blue line.

probabilities, a method of establishing the different core-cluster decompositions has been described. This method can be used to determine the most likely heavy clusters which can form in heavy nuclei and possibly be emitted in exotic decay. Most actinide nuclei, however, can also decay by spontaneous fission, and emit even heavier clusters. It is interesting therefore to extend this method, and see if it can predict heavier clusters which can be emitted, up to the point of fission.

Figure (4.6) shows the value of $\bar{D}$ for ^{224}Th up to large clusters, where $Z_2 = 45$. It clearly indicates three prominent peaks, corresponding to three separate core-cluster formations of varying sizes. Each of these peaks can be described within the shell model, by simply utilizing the known magic numbers. Since a nucleus decomposed into a core and cluster prefers the most tightly bound structure, i.e. both core and cluster doubly- or singly magic, or either core or cluster doubly- or singly magic, these peaks correspond to situations where the core and/or cluster are particularly tightly bound. Within the shell model, the magic numbers $(2, 8, 20, 28, 50, 82, 126)$ indicate the complete filling

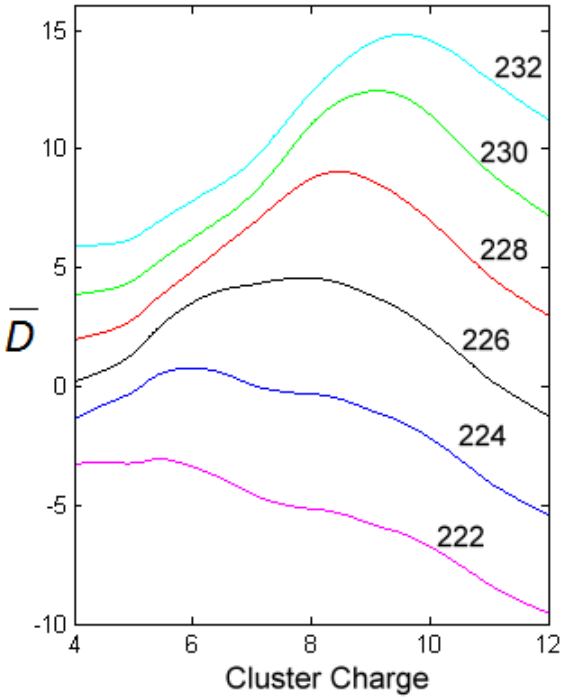

Figure 4.5: Smoothed calculation of $\bar{D}(Z_1, A_1, Z_2, A_2)$ as a function of cluster charge for $^{222-232}Th$ isotopes. The values for $^{222-232}Th$ have been shifted vertically by 3 MeV for greater clarity

of a shell, and therefore a more tightly bound structure.

The first peak occurs around $Z_2 = 8$, and is the value of the cluster used to indicate exotic decay. This peak forms since these cluster formations are centered around a cluster charge $Z_2 = 8$ to the right, and a neutron number of $N_2 = 8$ to the left side of the peak. Furthermore, the core is centered around a doubly magic ^{208}Pb core, with charge number $Z_1 = 82$ and neutron number $N_1 = 126$, such that there exists plenty of filled neutron and proton shells within the core and cluster, creating a dominant maximum.

The second peak occurs around $Z_2 = 20$, which is itself a magic number. Some clusters around this area will also have a neutron number of $N_2 = 28$, indicating at least singly magic clusters in each core-cluster decomposition. In this case, no magic numbers are present within the core, which explains the difference in the value of $\bar{D}$ between this peak and the other two, since only the cluster has completely filled shells.

The third peak, to the far right, occurs around $Z_2 = 35$, which is not a magic number, but corresponds to a neutron number of $N_2 = 50$, which is a magic number. The core, however, is situated around the proton number $Z_1 = 50$, towards the right of the peak, and the neutron number $N_1 = 82$, indicating that both core and cluster will be singly magic in this region. This

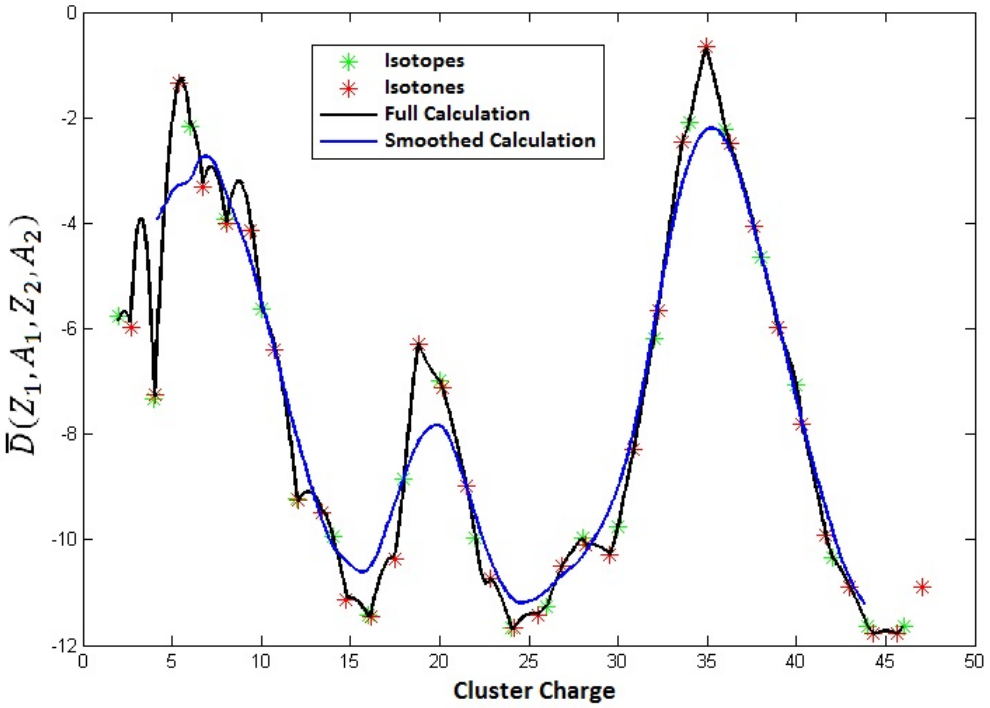

Figure 4.6: Calculations of $\bar{D}(Z_1, A_1, Z_2, A_2)$ as a function of cluster charge for ^{224}Th. Isotopes are indicated with green crosses, isotones with red crosses and the full calculation is indicated with the black line. A smoothed calculation is indicated with a blue line.

region may be an indication of fission fragments, and considering the nucleus to consist of these heavy clusters, it might be possible to describe fission.

Chapter 5

Thorium Isotopes

Having established a method of determining the most likely core-cluster decomposition in which a nucleus is considered to consist of a mixture of up to four different core-cluster decompositions, several structure observables can now be calculated and compared to experimental values. The exotic decay half-life can be calculated by using equation (3.3.23) along with equation (3.3.1); the reduced transition probability for electric multipole transitions can be calculated by using equation (3.2.7); and energy spectra can be calculated by utilizing the BS Rule, equation (2.3.4).

Although the decay half-life and energy spectrum can be calculated without any knowledge of the wavefunction, the electromagnetic transition probability requires explicit knowledge of the wavefunction. This establishes the need to solve the Schrödinger Equation (equation 2.1.1), in order to obtain information about the wavefunction. By solving the SE, an energy spectrum can also be obtained, and compared to that found by the semi-classical Bohr-Sommerfeld approximation and experiment.

5.1 Numerical Solution to the Schrödinger Equation

The radial Schrödinger Wave Equation (SWE),

$$\left(-\frac{\hbar^2}{2\mu}\frac{d^2}{dr^2} + V_L(r)\right)\varphi_{nL}(r) = E_{nL}\varphi_{nL}(r)$$

is a second-order differential equation, which cannot be solved analytically for arbitrary potentials, $V_L(r)$. For this reason, the SWE must be solved numerically. This can be done in different ways, one of which is to separate the 2^{nd}

order differential equation into two coupled first order differential equations,

$$\frac{d\varphi}{dr} = \psi(r)$$
$$\frac{d^2\varphi}{dr^2} = \frac{d\psi}{dr} = -k^2(r)\psi(r)$$

where $k^2(r) = \frac{2\mu}{\hbar^2}(E - V(r))$, and a Runge-Kutta method is used to solve for $\varphi(r)$.

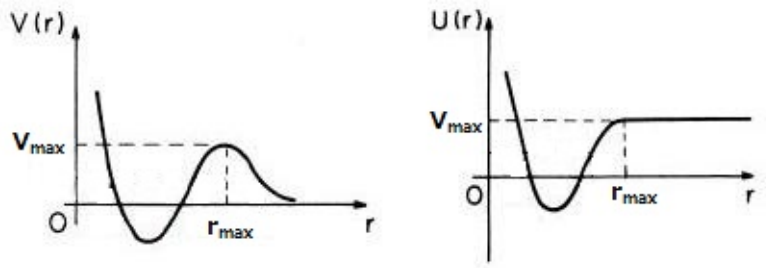

Figure 5.1: The nuclear potential $V(r)$ (left) vanishes for greater radial distances, while the modified nuclear potential $U(r)$ (right) equals the maximum value of the potential beyond r_{max}.

In order to avoid the complication brought about by the unbound nature of the wavefunction, the potential gets modified as shown in figure (5.1) [10], and is then given by

$$U(r) = \begin{cases} V_{max} & , \quad r > r_{max} \\ V_L(r) + V_C(r) + V_N(r) & , \quad r < r_{max} \end{cases} \tag{5.1.1}$$

where the Coulomb and Nuclear potentials take on their normal forms (equation 2.1.6 and 2.1.9), but the centrifugal potential takes on the form of equation (2.1.7), and does not get Langer modified.

Given the G-value of a $L = 0, 2, 4, \cdots$ core-cluster band, the radius R_0 of the band can be determined by fitting the $L = 0$ ground state member of the band to the experimentally known Q-value, while all the remaining potential parameters, a, x, and V_0 of equation (2.1.9) are assumed specified. All the necessary information is then in place to calculate the $L = 2, 4, 6, \cdots$ excited states of the system. An example of the many nodal radial wavefunction $\varphi_{nL}(r)$ for $n = 25$ and $L = 0$ thus obtained is shown in figure (5.2).

5.2 Parameter Dependence

The BCM has been used to reproduce exotic decay data to good precision in the past, particularly when using the Woods-Saxon and Woods-Saxon Cubed

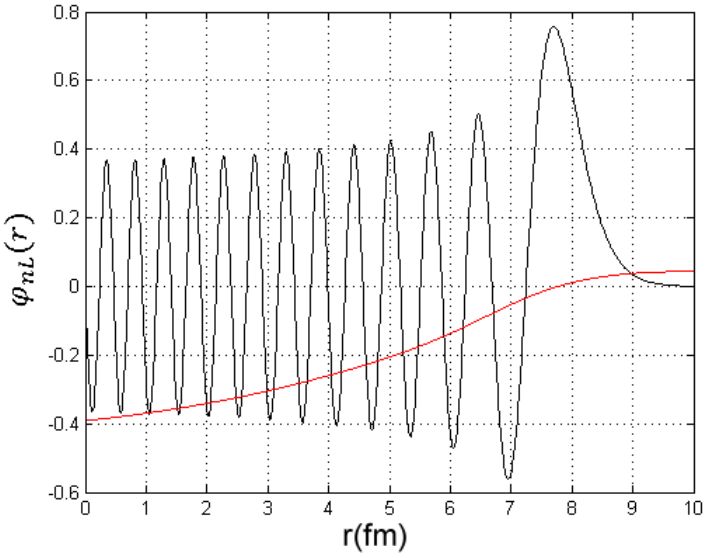

Figure 5.2: The calculated wavefunction (black) for the core-cluster decomposition $^{222}Th \rightarrow ^{212}Rn + ^{10}Be$, $\varphi_{nL}(r)$ for $n = 25$ and $L = 0$, corresponding to the modified potential $U(r)$ decreases exponentially beyond r_{max}, as required. For reference, a normalized potential (red) is also included.

potential. This potential, however, is parameter dependent, and the calculated value of different structure observables depend to different degrees on these parameters. Although the value of the diffuseness parameter, $a = 0.75$, the mixing parameter, $x = 0.36$, and the global quantum number, $G = 5A_2$, are normally kept the same [22, 23], the value of the potential depth, V_0 tends to be different, ranging from $V_0 = 55.7A_2$ [23] to $V_0 = 56.6A_2$ [22], while the radius, R_0, is always fitted to the ground state energy.

It would be a useful exercise to therefore determine how the structure observables - the exotic decay half-life, the electromagnetic transition probability and the energy spectrum - depend on these parameters, and determine the best-fit parameters to describe the exotic decay of actinide nuclei.

To this end, each structure observables' dependence on the diffuseness and mixing parameter as well as the potential depth is investigated. Each parameter value will be adjusted separately, with the other values taking on the values of equation (5.2.1). For this exercise, the exotic decay of ^{230}Th is investigated, with the results shown in tables (5.2, 5.3, 5.4), and the experimental values given in table (5.1).

$$\begin{aligned} a &= 0.75 \\ x &= 0.36 \\ V_0 &= 56.6A_2 \\ G &= 5A_2 \end{aligned} \tag{5.2.1}$$

$T_{1/2}^{expt}$[y]	$B(E2;2^+ \rightarrow 0^+)^{expt}$[W.u.]	E_{24}^{expt}[MeV]
1.300×10^{17}	196 ± 8	3.819

Table 5.1: Experimental structure observables for $^{230}Th \rightarrow ^{206}Hg + ^{24}Ne$.

a	R_0	$T_{1/2}^{calc}$[y]	$B(E2;2^+ \rightarrow 0^+)^{calc}$[W.u.]	E_{24}^{calc}[MeV]
0.75	6.5589	3.6554×10^{17}	217	3.690
0.76	6.5664	1.7003×10^{17}	222	3.743
0.79	6.5881	1.7417×10^{16}	236	3.888
0.83	6.6148	8.6931×10^{14}	256	4.048

Table 5.2: The dependence of the structure observables on the diffuseness parameter for $^{230}Th \rightarrow ^{206}Hg + ^{24}Ne$.

x	R_0	$T_{1/2}^{calc}$[y]	$B(E2;2^+ \rightarrow 0^+)^{calc}$[W.u.]	E_{24}^{calc}[MeV]
0.36	6.5589	3.6554×10^{17}	217	3.690
0.37	6.5339	5.1343×10^{17}	215	3.641
0.38	6.5091	7.2098×10^{17}	213	3.590
0.40	6.4601	1.4203×10^{18}	209	3.488

Table 5.3: The dependence of the structure observables on the mixing parameter for $^{230}Th \rightarrow ^{206}Hg + ^{24}Ne$.

V_0	R_0	$T_{1/2}^{calc}$[y]	$B(E2;2^+ \rightarrow 0^+)^{calc}$[W.u.]	E_{24}^{calc}[MeV]
$56.6A_2$	6.5589	3.6554×10^{17}	217	3.690
$57.2A_2$	6.5249	6.1463×10^{17}	215	3.756
$59.4A_2$	6.4043	3.9010×10^{18}	205	3.996
$62.3A_2$	6.2547	3.9189×10^{19}	193	4.308

Table 5.4: The dependence of the structure observables on the potential depth for $^{230}Th \rightarrow ^{206}Hg + ^{24}Ne$.

1. **Radius**
   The radius, R_0, is fitted to the Q-value of the ground state for every set of parameters. This is done by solving the Schrödinger Equation numerically, and R_0 is therefore not a parameter as such, but rather a dependent variable. Its value increases with increasing diffuseness parameter and decreases with increasing mixing parameter and potential depth.

2. **Exotic Decay Half-Life**
   The exotic decay half-life can be calculated by making use of equations (3.3.23) and (3.3.1). These calculations require no knowledge of the wavefunctions, only of the shape of the potential and turning points. The turning points (r_1, r_2, r_3) are defined as the radial distances where the energy intersects the potential curve (figure 3.1). The preformation probability is taken to be $P = 1$ for the present purpose.

   From tables (5.2, 5.3, 5.4), it is clear that the exotic decay half-life is heavily dependent on all parameters. The half-life decreases with increasing diffuseness parameter, and increases with increasing mixing parameter and potential depth. The mixing parameter seems to have the slightest effect on the half-life, while as little as a 10% change in the diffuseness parameter can cause a change in the half-life by a factor of 400. The potential depth itself is also a very sensitive parameter; a change of 10% can bring about a factor 100 change in the half-life.

   The dependence of the half-life on the preformation probability is also important, and should therefore be considered. As P becomes smaller, the half-life becomes longer, and the appropriate change in the potential parameters, such as a decrease in potential depth, have to take place to ensure the correct calculated half-life.

3. **Reduced Electromagnetic Transition Probability**
   The reduced electromagnetic transition probability can be calculated by making use of equation (3.2.7) and by introducing an effective charge by replacing,
   $$Z_i \rightarrow Z_i + \epsilon A_i$$
   where $\epsilon = 0.17$. This corresponds to a very modest effective charge, particularly in the present study which accounts for $B(E2)$ values of the order of 100 W.u.

   Unlike the exotic decay half-life, the transition probability increases with increasing diffuseness parameter and decreases with increasing mixing parameter and potential depth. The value of the transition probability is also not as dependent on these parameters as the half-life, with a 10% change in the diffuseness parameter causing a 40% change in the $B(E2)$ value, while a 10% change in the mixing parameter only manages a 4% change in the $B(E2)$ value.

4. **Energy Spectra**
   The energy spectrum can be calculated in two ways; either by solving the SE, or by utilizing the BS Rule. In tables (5.2, 5.3, 5.4), it was calculated by solving the SE. Only the highest known energy level is shown; since the radius is fitted to the ground state, the energy level of the ground state will be inherently correct, and if the highest energy

level corresponds to the experimental value, all energy levels in-between will be close to their respective experimental values.

The energy level increases with increasing diffuseness parameter and potential depth, while decreasing with increasing mixing parameter. The effect of changes in the parameters on the energy level is also not that severe, since a 10% change in the diffuseness parameter causes a 10% change in the energy level, while a 10% change in the mixing parameter brings about a 5% change.

In order to determine the ideal parameters for reproducing experimental data on exotic decay, it has to be considered that the value of the preformation probability, P, is no longer equal to one. In the past, this value was always taken to equal unity, but Chapter 4 establishes a method of determining the value of P. Since the exotic decay half-life is the only observable dependent on the value, and also the most sensitive to each parameter, the parameters have been adjusted to allow the best fit of known exotic decay half-lives to their experimental values. In addition, only the potential depth is varied, to limit the amount of free parameters. The best fit parameters were then found to be,

$$\begin{aligned} a &= 0.75 \\ x &= 0.36 \\ V_0 &= 54.7A_2 \\ G &= 5A_2 \end{aligned} \tag{5.2.2}$$

and have been used throughout the following analyses.

5.3 Thorium-222

The first nucleus to be investigated using the parameter set of equation (5.2.2) is ^{222}Th. The cluster size calculation yields a maximum value for $\bar{D}(Z_1, A_1, Z_2, A_2)$ at $Z_2 = 4.51$ (figure 5.3) when using the smoothed calculation, since the full calculation yields two very prominent peaks. The four most likely core-cluster decompositions, with their weighted probabilities, are then given in table (5.5).

The most likely cluster is that of $^{10}_{4}Be$. The peak forming with a cluster charge of $Z_2 \sim 3$ indicates the possibility of Be clusters forming, and this moves the maximum of the smoothed calculation towards a cluster charge of $Z_2 \sim 4$, since the two maxima obtained from the full calculation at $Z_2 \sim 5$ and $Z_2 \sim 3$ both include Be clusters.

The exotic decay half-life of each core-cluster decomposition can then be calculated, by using the appropriate preformation probability. This is done by

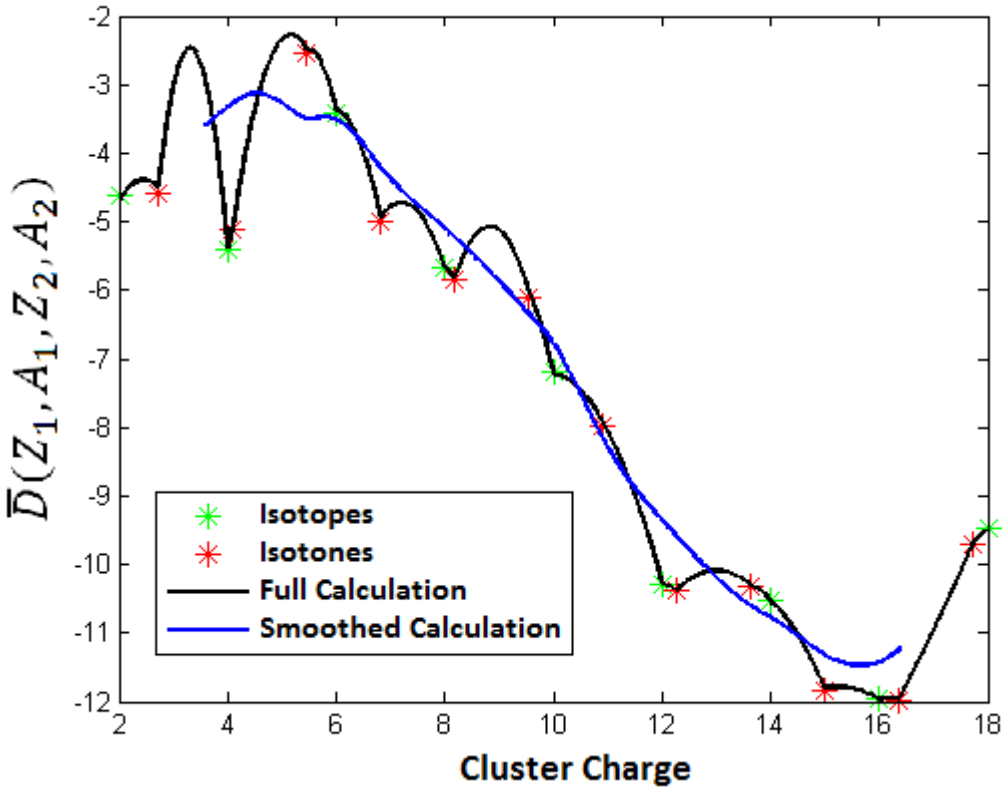

Figure 5.3: Calculations of $\bar{D}(Z_1, A_1, Z_2, A_2)$ as a function of cluster charge for ^{222}Th. Isotopes are indicated with green crosses, isotones with red crosses and the full calculation is indicated with the black line. A smoothed calculation is indicated with a blue line.

using equation (3.3.23),

$$\Gamma = P\frac{\hbar^2}{2m}\frac{\exp\left[-2\int_{r_2}^{r_3}|p(r)|dr\right]}{\int_{r_1}^{r_2}\frac{1}{p(r)}dr}$$

along with equation (3.3.1), $T_{1/2} = \frac{\hbar \ln 2}{\Gamma}$, and are shown in table (5.5).

Since no experimental data on the cluster decay of ^{222}Th exists, these results are speculative. The most likely cluster of ^{10}Be has a very long half-life and has never been observed in the exotic decay of any nucleus. A more realistic decay would then be that of ^{14}C or ^{12}C, both of which have relatively low probabilities, but the short half-life of ^{12}C makes this the more probable mode of cluster decay.

The extremely long half-life of ^{12}Be indicates that even if the nucleus decays by emitting this cluster, it would be nearly impossible to detect, especially since the α-decay half-life is only 2.24 ms, making the detection of any cluster decay nearly impossible.

Table 5.5: Cluster decompositions of ^{222}Th with weighted probabilities and corresponding exotic decay half-lives.

Cluster Decomposition	Q[MeV]	P	$T_{1/2}^{calc}$[y]	$T_{1/2}^{expt}$[y]
$^{222}Th \rightarrow ^{14}_{6}C + ^{208}_{84}Po$	31.652	0.0806	1.5485×10^{9}	
$^{222}Th \rightarrow ^{12}_{6}C + ^{210}_{84}Po$	33.156	0.1794	3327.5	
$^{222}Th \rightarrow ^{12}_{4}Be + ^{210}_{86}Rn$	1.724	0.2294	4.8116×10^{267}	
$^{222}Th \rightarrow ^{10}_{4}Be + ^{212}_{86}Rn$	13.256	0.5106	5.9903×10^{22}	

The next structure observable to compute is that of the reduced electromagnetic transition probability, by making use of equation (3.2.7),

$$B(E\ell; L_i \rightarrow L_f) = \frac{1}{4\pi}\beta_\ell^2 \hat{\ell}^2 \left|\langle L_i 0 \ell 0 |\, L_f 0\rangle\right|^2 \left|\left\langle \psi_{L_f} \right| r^\ell \left|\psi_{L_i}\right\rangle\right|^2$$

and introducing an effective charge by replacing

$$Z_i \rightarrow Z_i + \epsilon A_i \tag{5.3.1}$$

where $\epsilon = 0.17$ throughout the following.

The $B(E2)$ values for each core-cluster decomposition can be computed, and then an average value extracted by weighting the four separate values according to the probability of the corresponding core-cluster formation. This average $B(E2)$ is then expected to match the experimental values [42] and are shown in table (5.6).

The average values for both $B(E2; 2^+ \rightarrow 0^+)$ and $B(E2; 4^+ \rightarrow 2^+)$ are too low, indicating that the parameter set used should have had a shallower potential depth. Since these parameters, however, were obtained by fitting exotic decay half-life data and no exotic decay data has been observed for ^{222}Th, it was expected that some values would be incorrect. However, the calculated values are within a factor of 2, which is still satisfactory, given the simplicity of the model.

The $B(E2)$ values in Weisskopf units give an indication of the strength of the transition as compared to the single-particle strength. Even a value of $\sim$ 50W.u. is large, and indicates that the probability of the transition occurring is high.

The final structure observable to compute is the energy spectra. This can be calculated in two ways; either by solving the SE, or by utilizing the BS Rule, equation (2.3.4),

$$\int_{r_1}^{r_2} \sqrt{\frac{2\mu}{\hbar^2}\left(E_L - V(r)\right)} dr = (G - L + 1)\frac{\pi}{2}.$$

The energy spectrum calculated by using the SE is shown in table (5.7) and for the BS Rule in table (5.8). In each case, the energy spectrum calculated for each core-cluster decomposition, as well as the weighted average, is shown.

Table 5.6: $B(E2)$ values for each different core-cluster decomposition as well as the weighted average for ^{222}Th. All values are shown in units of the Weisskopf Unit (W.u.)

Core		$^{208}_{84}Pb$	$^{210}_{84}Pb$	$^{210}_{86}Rn$	$^{212}_{86}Rn$	
Cluster		$^{14}_{6}C$	$^{12}_{6}C$	$^{12}_{4}Be$	$^{10}_{4}Be$	
	$B(E2)^{expt}$	$B(E2)^{calc}$				$B(E2)^{avg}$
$B(E2;2^+ \rightarrow 0^+)$	74 ± 7	84	76	40	38	49
$B(E2;4^+ \rightarrow 2^+)$	108	119	108	57	54	70

It is interesting to firstly note the very small difference between the two methods of $\sim 0.3\%$, even though the BS Rule is a semi-classical approximation to solving the SE.

Compared to the experimental values [42], the energy spectrum is very good, with a difference of $\sim 0.2MeV$ for the 26^+ excited state. The calculated levels, however, are too low at first and then move from a difference of $\sim 0.35MeV$ at E_{12} to the $\sim 0.2MeV$ difference for E_{26}.

Table 5.7: Energy levels calculated for each core-cluster decomposition, as well as the weighted average, for ^{222}Th by solving the Schrödinger Equation. All values are shown in MeV.

	Core	$^{208}_{84}Pb$	$^{210}_{84}Pb$	$^{210}_{86}Rn$	$^{212}_{86}Rn$	
	Cluster	$^{14}_{6}C$	$^{12}_{6}C$	$^{12}_{4}Be$	$^{10}_{4}Be$	
	R_0	6.7272	6.8587	6.7757	6.8046	
L^π	E_L^{expt}	E_L^{calc}				E_L^{avg}
0^+	0.0	0.0	0.0	0.0	0.0	0.0
2^+	0.183	0.071	0.075	0.075	0.089	0.082
4^+	0.440	0.226	0.233	0.234	0.270	0.251
6^+	0.750	0.444	0.456	0.455	0.522	0.488
8^+	1.094	0.720	0.732	0.728	0.832	0.781
10^+	1.461	1.047	1.058	1.050	1.194	1.125
12^+	1.851	1.420	1.422	1.411	1.600	1.510
14^+	2.260	1.839	1.827	1.811	2.042	1.934
16^+	2.688	2.294	2.262	2.238	2.514	2.388
18^+	3.134	2.784	2.724	2.693	3.007	2.866
20^+	3.596	3.304	3.207	3.169	3.512	3.362
22^+	4.078	3.850	3.708	3.660	4.028	3.872
24^+	4.578	4.420	4.218	4.162	4.536	4.384
26^+	5.098	5.007	4.732	4.668	5.035	4.894
	χ^2	1.2749	1.7072	1.9513	0.4015	0.8857

A measure of how accurate the calculated energy spectrum fits the experimental energy spectrum, χ^2, can also be introduced for each energy spectrum

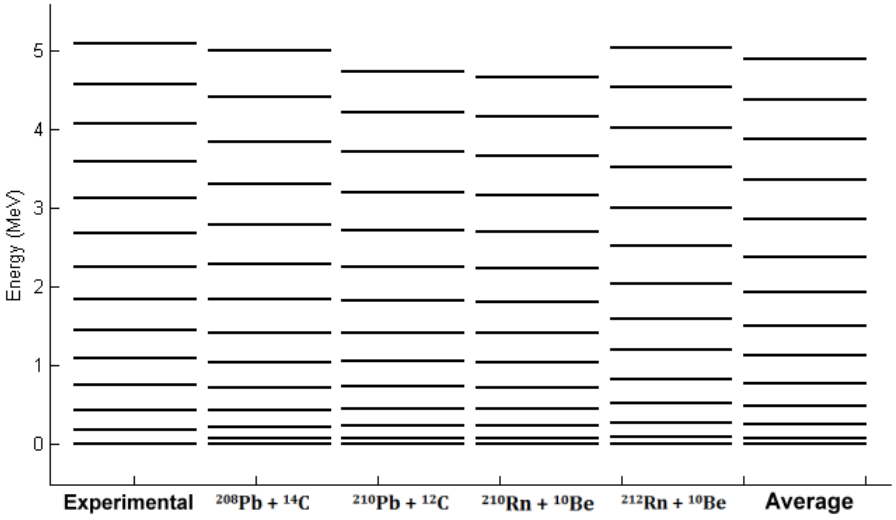

Figure 5.4: Energy levels calculated for each core-cluster decomposition, as well as the weighted average, for ^{222}Th by solving the Schrödinger Equation. All values are shown in MeV.

calculation. This is calculated according to

$$\chi^2 = \sum_L \left(E_L^{expt} - E_L^{calc}\right)^2 \tag{5.3.2}$$

where a minimum in χ^2 corresponds to the most accurate energy spectrum.

According to the χ^2 values, the best energy spectrum is obtained from the ^{10}Be, which is also the most probable cluster.

Table 5.8: Energy levels calculated for each core-cluster decomposition, as well as the weighted average, for ^{222}Th by solving the BS Rule. All values are shown in MeV.

	Core	$^{208}_{84}Pb$	$^{210}_{84}Pb$	$^{210}_{86}Rn$	$^{212}_{86}Rn$	
	Cluster	$^{14}_{6}C$	$^{12}_{6}C$	$^{12}_{4}Be$	$^{10}_{4}Be$	
	R_0	6.7270	6.8597	6.7766	6.8058	
L^π	E_L^{expt}	E_L^{calc}				E_L^{avg}
0^+	0.0	0.0	0.0	0.0	0.0	0.0
2^+	0.183	0.076	0.078	0.080	0.092	0.086
4^+	0.440	0.230	0.236	0.238	0.273	0.255
6^+	0.750	0.448	0.457	0.458	0.523	0.490
8^+	1.094	0.723	0.732	0.732	0.833	0.783
10^+	1.461	1.050	1.056	1.051	1.193	1.124
12^+	1.851	1.422	1.421	1.412	1.597	1.509
14^+	2.260	1.838	1.822	1.808	2.037	1.930
16^+	2.688	2.291	2.256	2.235	2.506	2.382
18^+	3.134	2.780	2.717	2.688	2.998	2.859
20^+	3.596	3.299	3.198	3.162	3.503	3.354
22^+	4.078	3.844	3.697	3.651	4.015	3.861
24^+	4.578	4.412	4.205	4.151	4.523	4.372
26^+	5.098	4.998	4.718	4.655	5.019	4.880
	χ^2	1.2788	1.7583	1.9868	0.4155	0.9133

5.4 Thorium-224

The next isotope under consideration, is ^{224}Th. The cluster charge which yields a maximum value for $\bar{D}(Z_1, A_1, Z_2, A_2)$ is $Z_2 = 6.24$. From figure (5.6), it can be seen that the full calculation has a maximum slightly smaller than $Z_2 = 6$, but the smooth calculation increases this maximum to a value greater than 6, due to the slightly smaller maxima occurring at $Z_2 \sim 7$ and $Z_2 \sim 8.5$.

This optimal value of the cluster charge, $Z_2 = 6.24$, is in accordance with the observation of a C cluster structure, and C is the smallest known cluster emitted from heavy nuclei. The four core-cluster decompositions relating to $Z_2 = 6.24$ are given in table (5.9), along with their appropriate probabilities.

Unfortunately, no cluster decay has been observed for ^{224}Th, and therefore the calculated values of the exotic decay half-life cannot be compared to experimental values. It can be seen, however, that ^{16}C forms the dominant core-cluster formation, while ^{14}C also has a large probability. The two O clusters, however, have very small probabilities, and therefore the possibility of ever observing these decays will be extremely small.

With the weighted probabilities of the two C clusters, it may be possible to observe the cluster decay via ^{14}C, since this is a cluster which is commonly emitted with a relatively short half-life. The α-decay half-life, however, is only

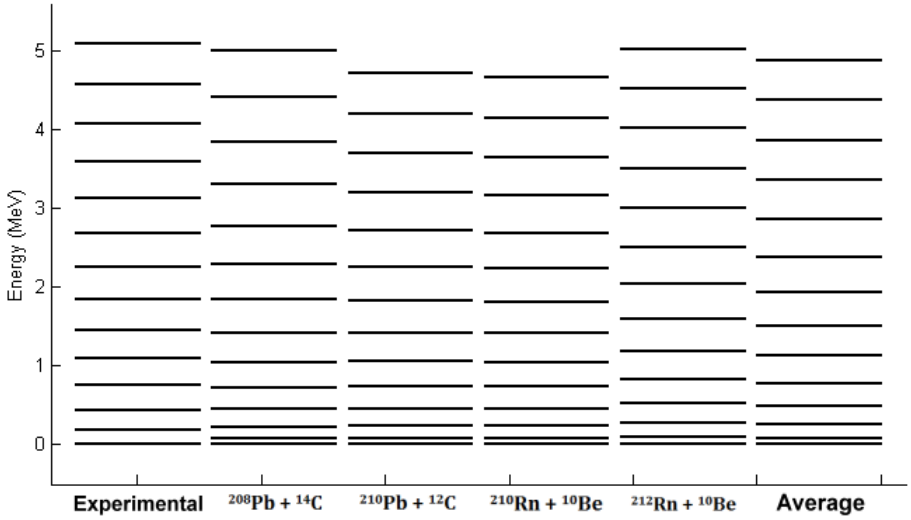

Figure 5.5: Energy levels calculated for each core-cluster decomposition, as well as the weighted average, for ^{222}Th by solving theBS Rule. All values are shown in MeV.

1.05 s, which will make the observation of cluster decay increasingly difficult.

Table 5.9: Cluster decompositions of ^{224}Th with weighted probabilities and corresponding exotic decay half-lives.

Cluster Decomposition	Q [MeV]	P	$T_{1/2}^{calc}$[y]	$T_{1/2}^{expt}$[y]
$^{224}Th \rightarrow ^{18}_{8}O + ^{206}_{82}Pb$	44.563	0.078	2.2836×10^{13}	
$^{224}Th \rightarrow ^{16}_{8}O + ^{208}_{82}Pb$	46.482	0.042	2.9861×10^{8}	
$^{224}Th \rightarrow ^{16}_{6}C + ^{208}_{84}Po$	23.772	0.572	5.6804×10^{31}	
$^{224}Th \rightarrow ^{14}_{6}C + ^{210}_{84}Po$	32.929	0.308	1.5013×10^{6}	

The calculated $B(E2)$ values, compared to experimental values [43], are shown in table (5.10). Only experimental data on the $B(E2; 2^+ \rightarrow 0^+)$ transition exists, but the $B(E2; 4^+ \rightarrow 2^+)$ transition is also calculated. In this case, the average $B(E2)$ value falls within the error range of the experimental value. This is a very good result indeed, since the parameter values were not fitted to any data of ^{224}Th, but the results obtained are still accurate and correspond to very strong transitions.

The final structure observable calculated is the energy spectrum, shown in table (5.11) and compared to experimental data [43]. The average calculated energy spectrum using both the SE and BS Rule are shown, and yet again the difference between the two is very small, with both spectra giving a good indication of the energy levels of ^{224}Th.

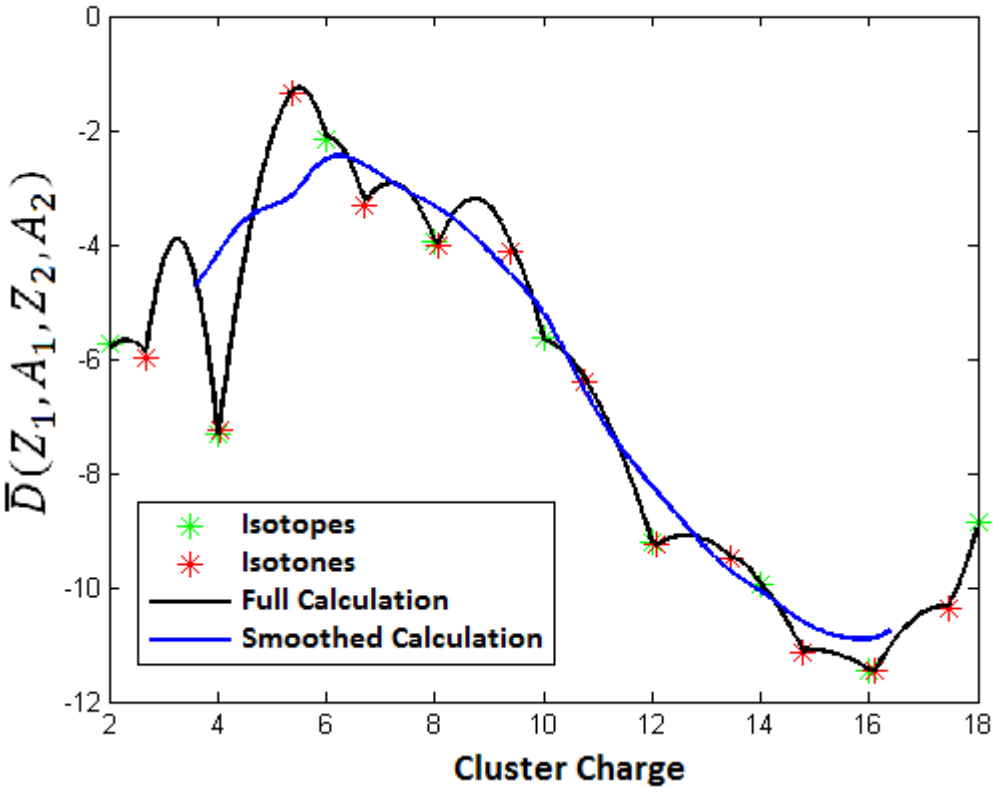

Figure 5.6: Calculations of $\bar{D}(Z_1, A_1, Z_2, A_2)$ as a function of cluster charge for ^{224}Th. Isotopes are indicated with green crosses, isotones with red crosses and the full calculation is indicated with the black line. A smoothed calculation is indicated with a blue line.

Table 5.10: $B(E2)$ values for each different core-cluster decomposition as well as the weighted average for ^{224}Th. All values shown are measured in Weisskopf Units [W.u.].

Core		$^{206}_{82}Pb$	$^{208}_{82}Pb$	$^{208}_{84}Po$	$^{210}_{84}Po$	
Cluster		$^{18}_{8}O$	$^{16}_{8}O$	$^{16}_{6}C$	$^{14}_{6}C$	
	$B(E2)^{expt}$	$B(E2)^{calc}$				$B(E2)^{avg}$
$B(E2; 2^+ \rightarrow 0^+)$	96 ± 7	142	132	87	84	92
$B(E2; 4^+ \rightarrow 2^+)$		203	189	124	119	132

5.5 Thorium-226

The next nucleus in the isotopic sequence of Thorium is ^{226}Th. From figure (5.8), it can be seen that the full calculation of $\bar{D}(Z_1, A_1, Z_2, A_2)$ gives two prominent maxima. The smoothed calculation, however, reduces these two peaks at $Z_2 \sim 7$ and $Z_2 \sim 8$, to one maximum at $Z_2 = 7.79$. No important

Table 5.11: Weighted energy levels calculated for ^{224}Th by solving the SE and BS Rule. All values are shown in MeV.

L^π	E_L^{expt}	E_L^{SE}	E_L^{BS}
0^+	0.0	0.0	0.0
2^+	0.098	0.064	0.068
4^+	0.284	0.209	0.213
6^+	0.534	0.415	0.418
8^+	0.834	0.675	0.677
10^+	1.174	0.985	0.985
12^+	1.550	1.339	1.338
14^+	1.959	1.736	1.733
16^+	2.398	2.169	2.165
18^+	2.864	2.637	2.632
	χ^2	0.2807	0.2840

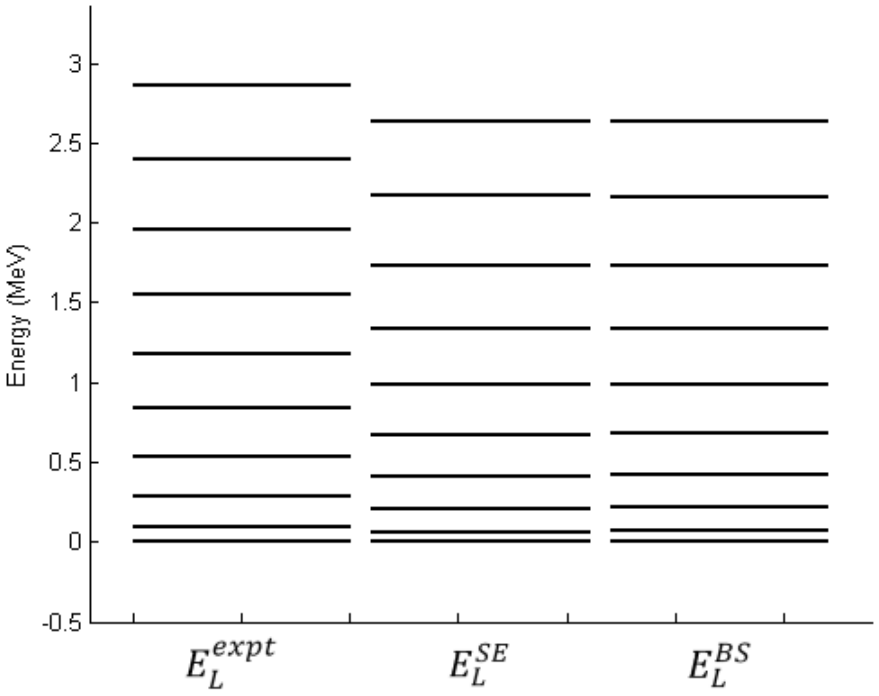

Figure 5.7: Weighted energy levels calculated for ^{224}Th by solving the SE and BS Rule. All values are shown in MeV.

information is lost, however, since the overlapping clusters of the two maxima from the full calculation is still evident in the maximum from the smoothed calculation.

The four core-cluster decompositions, with their respective probabilities,

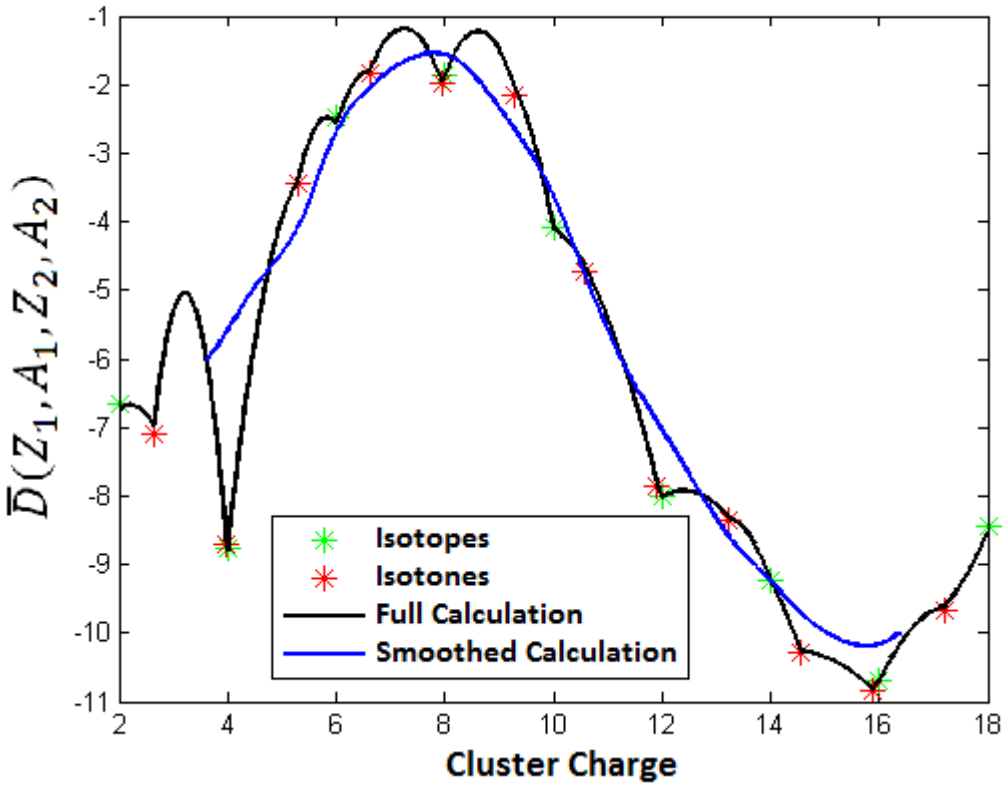

Figure 5.8: Calculations of $\bar{D}(Z_1, A_1, Z_2, A_2)$ as a function of cluster charge for ^{226}Th. Isotopes are indicated with green crosses, isotones with red crosses and the full calculation is indicated with the black line. A smoothed calculation is indicated with a blue line.

are shown in table (5.12). The most probable cluster seems to be that of ^{20}O, with all other possibilities having very small probabilities. Thorium-226 is however known to decay by emitting a ^{18}O cluster, but within the present model it only has a probability of 0.099 for this core-cluster structure to form. This small probability may be the reason why the calculated half-life for ^{18}O is incorrect. It is also notable that, in the past, the cluster emission of O isotopes have never been accurately described [22, 23].

The α-decay half-life of ^{226}Th is 30.57m [44], further explaining why the cluster emissions of the two C isotopes will not be observed experimentally, due to the magnitude of their decay half-lives compared to the α-decay half-life. It is interesting to note that ^{226}Th is the lightest Thorium isotope to be experimentally observed to decay via the emission of a heavy ion, and that the α-decay half-life compared to lighter Thorium isotopes is much greater. This allows the observation of exotic decay, since the branching ratio relative to α-decay is smaller compared to $^{222,224}Th$, and therefore exotic decay can be observed.

Table 5.12: Cluster decompositions of ^{226}Th with weighted probabilities and corresponding exotic decay half-lives.

Cluster Decomposition	Q [MeV]	P	$T_{1/2}^{calc}$[y]	$T_{1/2}^{expt}$[y]
$^{226}Th \rightarrow ^{20}_{8}O + ^{206}_{82}Pb$	43.185	0.801	7.1435×10^{16}	
$^{226}Th \rightarrow ^{18}_{8}O + ^{208}_{82}Pb$	45.724	0.099	2.1963×10^{11}	1.818×10^{9}
$^{226}Th \rightarrow ^{18}_{6}C + ^{208}_{84}Po$	15.740	0.089	2.5351×10^{75}	
$^{226}Th \rightarrow ^{16}_{6}C + ^{210}_{84}Po$	25.456	0.011	1.3121×10^{28}	

The reduced electromagnetic transition probability can also be computed once the different core-cluster decompositions and their appropriate weighting factors are known. By computing the $B(E2)$ values of each core-cluster decomposition and then weighting these factors with their probabilities, the average value can be computed, and compared to the experimental value. These results are shown in table (5.13), and compared to experimental values [45].

The calculated value of $B(E2; 2^+ \rightarrow 0^+) = 145$ W.u. does not fall within the error bounds of the experimental value, but only differs by $\sim 10\%$, which is still a very good approximation. It is interesting to note the increasing strength of the $B(E2; 2^+ \rightarrow 0^+)$ and $B(E2; 4^+ \rightarrow 2^+)$ transitions in increasing cluster charge, and therefore also increasing isotope mass, since it has been shown that heavier isotopes prefer core-cluster decompositions with heavier clusters.

Table 5.13: $B(E2)$ values for each different core-cluster decomposition as well as the weighted average for ^{226}Th. All values are shown in Weisskopf Units [W.u.].

Core		$^{206}_{82}Pb$	$^{208}_{82}Pb$	$^{208}_{84}Po$	$^{210}_{84}Po$	
Cluster		$^{20}_{8}O$	$^{18}_{8}O$	$^{18}_{6}C$	$^{16}_{6}C$	
	$B(E2)^{expt}$	$B(E2)^{calc}$				$B(E2)^{avg}$
$B(E2; 2^+ \rightarrow 0^+)$	164 ± 10	152	142	92	87	145
$B(E2; 4^+ \rightarrow 2^+)$		218	202	131	125	207

Lastly, the energy spectra using both the SE and BS Rule are computed. The results are shown in table (5.14), and compared to experimental data [45]. Similar to $^{222,224}Th$, the energy of the highest known excited state is ~ 0.2 MeV too low, while that difference is greater at lower energy levels. Overall the energy spectrum is a good fit, as can be seen from the small χ^2 values, with the SE and BS Rule results very similar.

5.6 Thorium-228

The plot of $\bar{D}(Z_1, A_1, Z_2, A_2)$ is shown in figure (5.10). This figure shows a prominent maximum at $Z_2 \sim 8.5$ for the full calculation, and indeed for the

Table 5.14: Weighted energy levels calculated for ^{226}Th by solving the SE and BS Rule. All values are shown in MeV.

L^π	E_L^{expt}	E_L^{SE}	E_L^{BS}
0^+	0.0	0.0	0.0
2^+	0.072	0.053	0.056
4^+	0.226	0.179	0.182
6^+	0.447	0.360	0.362
8^+	0.722	0.591	0.593
10^+	1.040	0.868	0.869
12^+	1.395	1.189	1.188
14^+	1.782	1.550	1.548
16^+	2.196	1.947	1.944
18^+	2.635	2.381	2.377
20^+	3.097	2.847	2.842
	χ^2	0.3420	0.3478

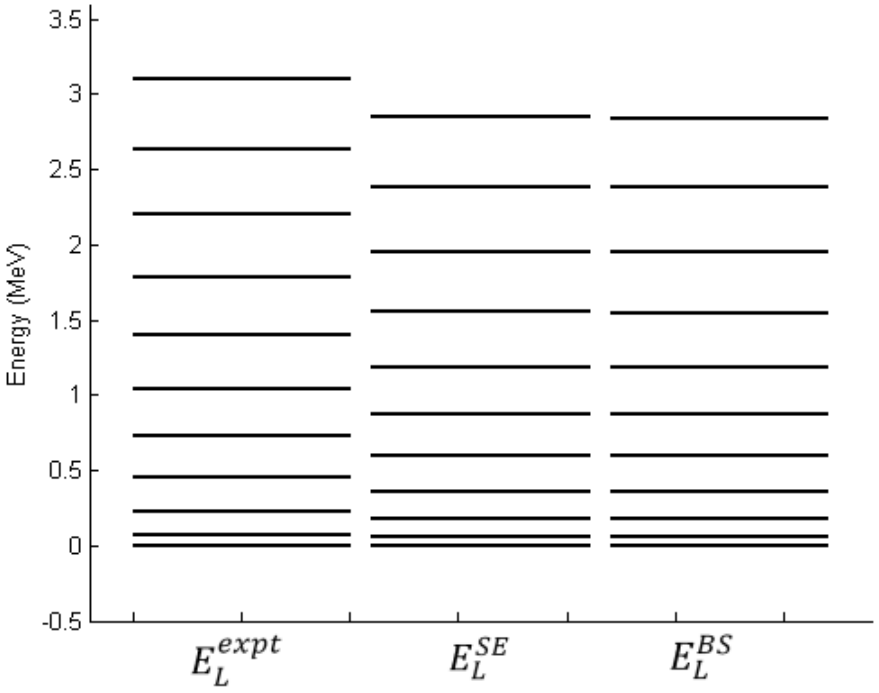

Figure 5.9: Weighted energy levels calculated for ^{226}Th by solving the SE and BS Rule. All values are shown in MeV.

smoothed calculation as well, $Z_2 = 8.48$. This value is consistent with an O cluster forming within the nucleus, along with a Pb core, both of which are at least singly magic, and therefore the preferred choice of core and cluster.

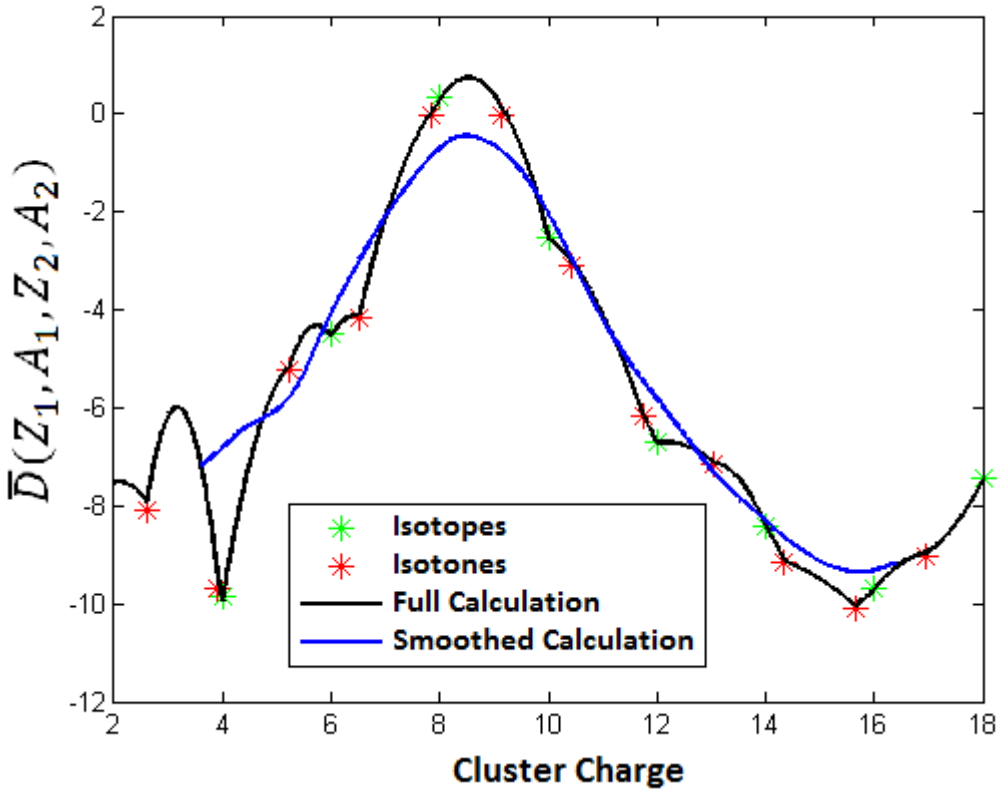

Figure 5.10: Calculations of $\bar{D}(Z_1, A_1, Z_2, A_2)$ as a function of cluster charge for ^{228}Th. Isotopes are indicated with green crosses, isotones with red crosses and the full calculation is indicated with the black line. A smoothed calculation is indicated with a blue line.

By using the most likely cluster charge, $Z_2 = 8.48$, the four core-cluster decompositions with their respective probabilities can be calculated, and are shown in table (5.15). This predicts the formation of two O clusters, with mass numbers 20 and 22, to form with equal probabilities as the most likely clusters. Only one of these clusters, ^{20}O, have been observed experimentally to be emitted from ^{228}Th [46].

Simply looking at the difference in magnitude between the calculated half-lives of the two O clusters, it is clear to see why only the exotic decay of ^{20}O has been observed, simply because its half-life is almost 10^{10} times smaller than that of ^{22}O.

When compared to the α-decay half-life of 1.9116y, it becomes clear why exotic decay is observed for ^{228}Th, due to the relative small branching ratio for ^{20}O, and the much greater branching ratios for the other possible clusters. Similar to the cluster emission of ^{226}Th, however, the calculated half-life for the cluster emission of ^{20}O is about 10 times greater than the experimental value, but this is in line with previous work [22, 23].

Table 5.15: Cluster decompositions of ^{228}Th with weighted probabilities and corresponding exotic decay half-lives.

Cluster Decomposition	Q [MeV]	P	$T_{1/2}^{calc}$[y]	$T_{1/2}^{expt}$[y]
$^{228}Th \rightarrow ^{24}_{10}Ne + ^{204}_{80}Hg$	57.414	0.12	1.8019×10^{18}	
$^{228}Th \rightarrow ^{22}_{10}Ne + ^{206}_{80}Hg$	55.742	0.12	1.457×10^{19}	
$^{228}Th \rightarrow ^{22}_{8}O + ^{206}_{82}Pb$	41.273	0.38	1.0063×10^{23}	
$^{228}Th \rightarrow ^{20}_{8}O + ^{208}_{82}Pb$	44.723	0.38	2.4022×10^{14}	1.692×10^{13}

The reduced electromagnetic transition probabilities are shown in table (5.16), along with experimentally measured values [46]. The weighted $B(E2; 2^+ \rightarrow 0^+)$ calculated by weighting the separate values of each core-cluster decomposition, falls within the error bounds of the experimental value, while the weighted value for $B(E2; 4^+ \rightarrow 2^+)$ is extremely close to the experimental value.

Although there exists exotic decay data for ^{228}Th, this data was not used for fitting the potential parameters, due to the fact that it has been found that the ^{20}O decays are poorly reproduced by a range of binary cluster models. The accuracy of the $B(E2)$ values are therefore very good results, indicating the strength of this simplistic model.

Table 5.16: $B(E2)$ values for each different core-cluster decomposition as well as the weighted average for ^{228}Th. All values is shown in Weisskopf Units [W.u.].

Core		$^{204}_{80}Hg$	$^{206}_{80}Hg$	$^{206}_{82}Pb$	$^{208}_{82}Pb$	
Cluster		$^{24}_{10}Ne$	$^{22}_{10}Ne$	$^{22}_{8}O$	$^{20}_{8}O$	
	$B(E2)^{expt}$	$B(E2)^{calc}$				$B(E2)^{avg}$
$B(E2; 2^+ \rightarrow 0^+)$	167 ± 6	229	211	163	152	172
$B(E2; 4^+ \rightarrow 2^+)$	242	327	301	232	217	246

The final structure observable to measure is the energy spectrum, and these results, along with experimental data, are shown in table (5.17). Comparing the highest known excited energy, E_{18}, the difference between the calculated and experimental values is only ~ 0.1 MeV, which is more accurate than the calculations done for lighter isotopes of Thorium. Further, the χ^2 value is less than 0.06, which is extremely small, and indicates a very good fit to the experimental data, with the SE and BS Rule results once more similar.

5.7 Thorium-230

The next nucleus in the isotopic sequence of Thorium is ^{230}Th, for which figure (5.12) shows the plot of $\bar{D}(Z_1, A_1, Z_2, A_2)$ for different cluster charges. The full

Table 5.17: Weighted energy levels calculated for ^{228}Th by solving the SE and BS Rule. All values are measured in MeV.

L^π	E_L^{expt}	E_L^{SE}	E_L^{BS}
0^+	0.0	0.0	0.0
2^+	0.058	0.048	0.054
4^+	0.187	0.168	0.174
6^+	0.378	0.342	0.346
8^+	0.623	0.564	0.567
10^+	0.912	0.830	0.833
12^+	1.239	1.140	1.141
14^+	1.600	1.489	1.488
16^+	1.988	1.874	1.873
18^+	2.408	2.296	2.294
	χ^2	0.0597	0.0588

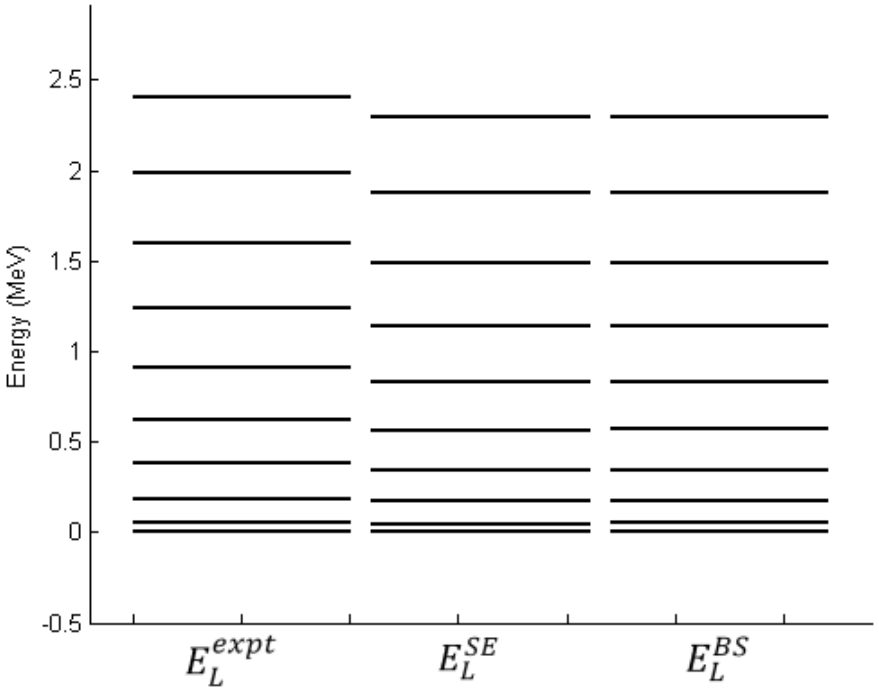

Figure 5.11: Weighted energy levels calculated for ^{228}Th by solving the SE and BS Rule. All values are shown in MeV.

calculation shows one distinct maximum at $Z_2 \sim 9$, and this is reflected in the maximum of the smoothed calculation, at $Z_2 = 9.26$.

The four different core-cluster decompositions, along with their probabilities, appear in table (5.18). The most likely cluster to form in this case is

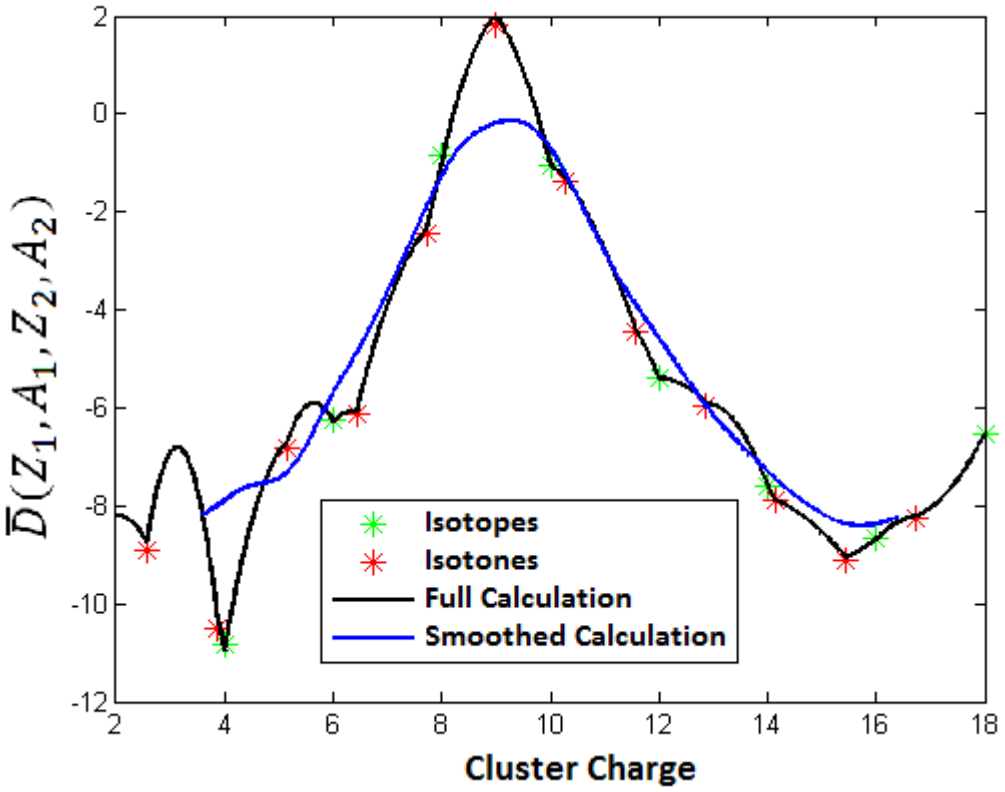

Figure 5.12: Calculations of $\bar{D}(Z_1, A_1, Z_2, A_2)$ as a function of cluster charge for ^{230}Th. Isotopes are indicated with green crosses, isotones with red crosses and the full calculation is indicated with the black line. A smoothed calculation is indicated with a blue line.

^{24}Ne, and its calculated exotic decay half-life corresponds to the experimental value [47] almost exactly. Comparing this half-life to the α-decay half-life of 7.54×10^4y shows that the branching ratio for ^{24}Ne relative to α-decay is relatively small, and can therefore be detected experimentally.

For the other three core-cluster decompositions, however, the branching ratio relative to α-decay is extremely small and therefore not experimentally detectable. The only exception is ^{22}O, which also has the next greatest probability of forming, and a half-life ~ 70 times that of ^{24}Ne, but its small preformation probability, together with the competition from the cluster decay of ^{24}Ne, makes it difficult to detect.

Table (5.19) shows the reduced electromagnetic transition probabilities for ^{230}Th. The weighted value calculated for $B(E2; 2^+ \rightarrow 0^+)$ compares very well with the experimental value, although it is just slightly outside the error bounds, while the calculated value for $B(E2; 4^+ \rightarrow 2^+)$ is greater than the experimental value [47].

The magnitude of these numbers indicate the dependence of the $B(E2)$

Table 5.18: Cluster decompositions of ^{230}Th with weighted probabilities and corresponding exotic decay half-lives.

Cluster Decomposition	Q[MeV]	P	$T_{1/2}^{calc}$[y]	$T_{1/2}^{expt}$[y]
$^{230}Th \rightarrow ^{26}_{10}Ne + ^{204}_{80}Hg$	55.125	0.126	4.9480×10^{23}	
$^{230}Th \rightarrow ^{24}_{10}Ne + ^{206}_{80}Hg$	57.761	0.504	1.3348×10^{17}	1.300×10^{17}
$^{230}Th \rightarrow ^{24}_{8}O + ^{206}_{82}Pb$	35.579	0.074	8.2853×10^{39}	
$^{230}Th \rightarrow ^{22}_{8}O + ^{208}_{82}Pb$	43.328	0.296	8.5631×10^{18}	

numbers on cluster charge. For increasing cluster charge, and therefore increasing isotope mass, the $B(E2)$ transition strength increases, and reaches significantly high strengths.

Table 5.19: $B(E2)$ values for each different core-cluster decomposition as well as the weighted average for ^{230}Th. All values are shown in Weisskopf units [W.u.].

Core		$^{204}_{80}Hg$	$^{206}_{80}Hg$	$^{206}_{82}Pb$	$^{208}_{82}Pb$	
Cluster		$^{26}_{10}Ne$	$^{24}_{10}Ne$	$^{24}_{8}O$	$^{22}_{8}O$	
	$B(E2)^{expt}$	$B(E2)^{calc}$				$B(E2)^{avg}$
$B(E2; 2^+ \rightarrow 0^+)$	196 ± 8	241	227	170	163	206
$B(E2; 4^+ \rightarrow 2^+)$	265	344	324	242	233	293

Lastly, the weighted energy spectrum for ^{230}Th is shown in table (5.20), when calculated both by solving the SE, and by using the BS Rule, along with the experimentally measured values [47]. Comparing the calculated values of the highest known energy level, E_{24}, the difference between both calculated values and the experimental value is about $\sim 0.2MeV$, with both methods giving similar results.

5.8 Thorium-232

The last Thorium isotope under consideration is ^{232}Th. Figure (5.14) shows the plot of $\bar{D}(Z_1, A_1, Z_2, A_2)$ as a function of cluster charge, with the full calculation giving one distinct maximum around $Z_2 \approx 9.5$. The smoothed calculation's maximum leans towards a higher cluster charge, due to the shape of the peak; it tails off longer towards higher cluster charges. The most likely cluster charge is then obtained as $Z_2 = 9.62$.

The four core-cluster decompositions with their respective probabilities are shown in table (5.21). From experimental data [48], ^{232}Th decays via the cluster emission of ^{24}Ne and ^{26}Ne. Only the half-life of ^{26}Ne is calculated accurately, with about a factor of 10 difference in the calculated and experimental half-lives of ^{24}Ne. Fortunately, the predicted core-cluster decompositions does have the two Ne isotopes as the most probable cluster structures.

Table 5.20: Weighted energy levels calculated for ^{230}Th by solving the SE and BS Rule. All values are measured in MeV.

L^π	E_L^{expt}	E_L^{SE}	E_L^{BS}
0^+	0.0	0.0	0.0
2^+	0.053	0.044	0.053
4^+	0.174	0.157	0.165
6^+	0.356	0.321	0.328
8^+	0.594	0.531	0.537
10^+	0.879	0.784	0.790
12^+	1.207	1.079	1.082
14^+	1.572	1.411	1.414
16^+	1.970	1.779	1.782
18^+	2.396	2.184	2.184
20^+	2.849	2.622	2.620
22^+	3.324	3.090	3.088
24^+	3.819	3.590	3.586
	χ^2	0.2978	0.2953

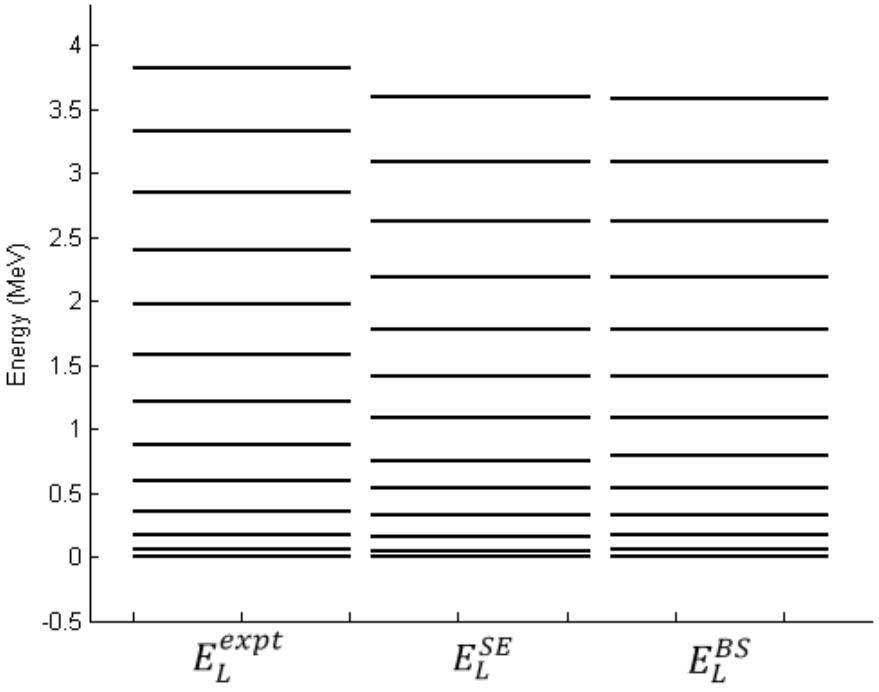

Figure 5.13: Weighted energy levels calculated for ^{230}Th by solving the SE and BS Rule. All values are shown in MeV.

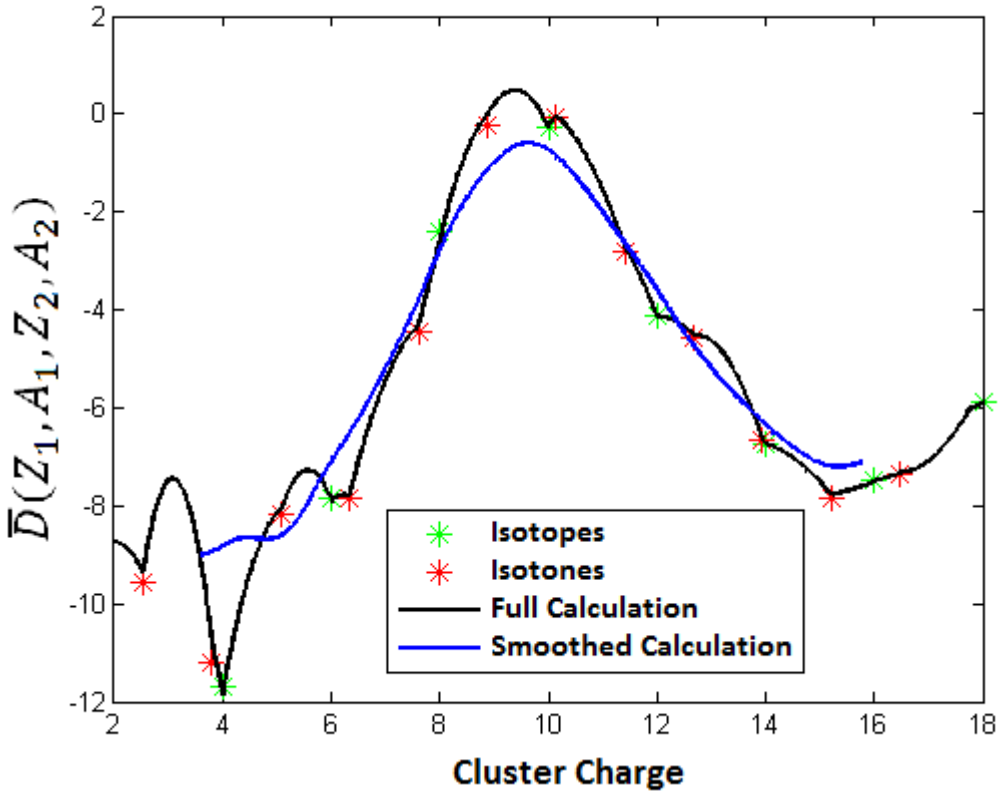

Figure 5.14: Calculations of $\bar{D}(Z_1, A_1, Z_2, A_2)$ as a function of cluster charge for ^{232}Th. Isotopes are indicated with green crosses, isotones with red crosses and the full calculation is indicated with the black line. A smoothed calculation is indicated with a blue line.

The formation of ^{26}Ne, however, is given as being the most probable cluster formation. Experiments normally find it difficult to distinguish between different clusters, such as $^{24,26}Ne$, although the half-life can be measured accurately, regardless of which cluster the nucleus decays by. It is therefore more likely that ^{232}Th decays via the cluster emission of ^{26}Ne, and not ^{24}Ne, since the experimentally measured half-life can be reproduced for ^{26}Ne.

The other two clusters, both isotopes of O, have small probabilities of forming, and the nuclear emission of these clusters aren't observed experimentally. Comparing the calculated half-lives to the α-decay half-life of 1.40×10^{10}y, the calculated half-life for ^{24}O is too long compared to the other clusters to be observed. The half-life of ^{22}O may suggest that the branching ratio relative to α-decay is small enough for it to be detected in cluster emission, but the small preformation probability, and the competition from the cluster emission of Ne isotopes, makes it nearly impossible to detect.

Table (5.22) shows the calculated $B(E2)$ values for each separate core-cluster decomposition as well as the weighted average, along with the exper-

Table 5.21: Cluster decompositions of ^{232}Th with weighted probabilities and corresponding exotic decay half-lives.

Cluster Decomposition	Q[MeV]	P	$T_{1/2}^{calc}$[y]	$T_{1/2}^{expt}$[y]
$^{232}Th \rightarrow ^{26}_{10}Ne + ^{206}_{80}Hg$	55.964	0.4779	4.8676×10^{21}	5.06×10^{21}
$^{232}Th \rightarrow ^{24}_{10}Ne + ^{208}_{80}Hg$	54.497	0.3321	6.5378×10^{22}	5.06×10^{21}
$^{232}Th \rightarrow ^{24}_{8}O + ^{208}_{82}Pb$	38.126	0.1121	8.8519×10^{32}	
$^{232}Th \rightarrow ^{22}_{8}O + ^{210}_{82}Pb$	40.892	0.0779	3.9613×10^{24}	

imental values [48]. The weighted value calculated for $B(E2; 2^+ \rightarrow 0^+)$ does fall outside the experimental error bounds, but is still a very good approximation to it, while the same can be said for the weighted value calculated for $B(E2; 4^+ \rightarrow 2^+)$.

Table 5.22: $B(E2)$ values for each different core-cluster decomposition as well as the weighted average for ^{232}Th. All values are measured in Weisskopf units [W.u.].

Core		$^{206}_{80}Hg$	$^{208}_{80}Hg$	$^{208}_{82}Pb$	$^{210}_{82}Pb$	
Cluster		$^{26}_{10}Ne$	$^{24}_{10}Ne$	$^{24}_{8}O$	$^{22}_{8}O$	
	$B(E2)^{expt}$	$B(E2)^{calc}$				$B(E2)^{avg}$
$B(E2; 2^+ \rightarrow 0^+)$	198 ± 11	239	220	170	158	219
$B(E2; 4^+ \rightarrow 2^+)$	286	341	314	243	226	312

Finally, table (5.23) shows the weighted energy spectrum calculated for ^{232}Th using both the SE method and the BS Rule, as well as the experimental data [48]. The calculated values for the highest known energy state, E_{30}, are a very good approximation to the experimental data, and only differs by about 0.1 MeV, with the differences between the SE and BS Rule being very small.

Table 5.23: Weighted energy levels calculated for ^{232}Th by solving the SE and BS Rule. All values are shown in MeV.

L^π	E_L^{expt}	E_L^{SE}	E_L^{BS}
0^+	0.0	0.0	0.0
2^+	0.049	0.042	0.049
4^+	0.162	0.150	0.157
6^+	0.333	0.308	0.314
8^+	0.557	0.509	0.516
10^+	0.827	0.753	0.759
12^+	1.137	1.037	1.041
14^+	1.482	1.360	1.361
16^+	1.859	1.715	1.716
18^+	2.262	2.105	2.105
20^+	2.691	2.528	2.526
22^+	3.144	2.981	2.978
24^+	3.620	3.464	3.460
26^+	4.117	3.975	3.970
28^+	4.633	4.514	4.507
30^+	5.164	5.078	5.069
	χ^2	0.1978	0.2028

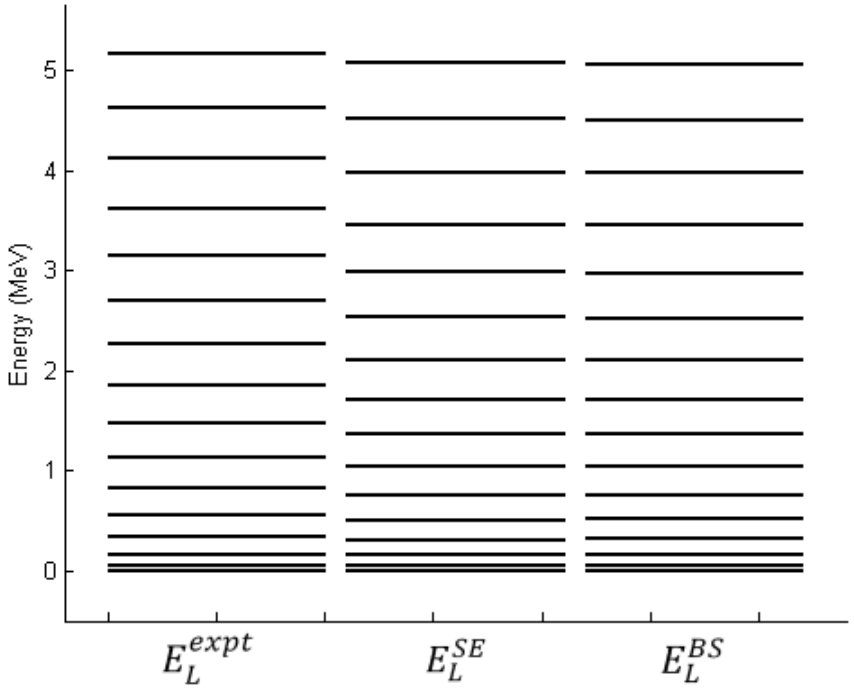

Figure 5.15: Weighted energy levels calculated for ^{232}Th by solving the SE and BS Rule. All values are shown in MeV.

Chapter 6

Uranium Isotopes

After the successful application of the BCM to Thorium isotopes, the application of this model was extended to include other actinide nuclei as well. Only isotopes with known exotic decay data were investigated, and the exotic decay half-life, $B(E2)$ values, and energy spectra were calculated for each of these isotopes.

6.1 Uranium-230

The first of these isotopes is ^{230}U, for which figure (6.1) shows the plot of $\bar{D}(Z_1, A_1, Z_2, A_2)$. The full calculation shows one distinct maximum near $Z_2 = 9$, similar to the smoothed calculation, whose maximum is at $Z_2 = 9.52$. The smoothed calculation shifts the maximum slightly to the right due to the shoulder to the right of the full calculation's peak.

Using the mean cluster charge obtained from the smoothed calculation, the four core-cluster decompositions, with probabilities, can be determined. These results are shown in table (6.1). The most likely cluster to form is that of ^{24}Ne, which is also the experimentally detected emitted cluster [47]. The calculated half-life for ^{24}Ne is within a factor 3 of the experimental value, and is still considered as accurate enough.

Comparing the other three clusters' half-lives to that of α-decay, which is 20.8d, it is clear why these clusters are not detected as exotic decay. The branching ratio relative to α-decay for all three these clusters, ^{26}Ne and $^{22,24}O$, will be extremely small, making the detection of these clusters nearly impossible.

By using the four most likely core-cluster decompositions, the $BE(2)$ values for each one can be computed. Their respective weights can then be used to calculate an average, or weighted, $B(E2)$ value, which should correspond to the experimental value [47]. These results are shown in table (6.2).

The calculated value for the $B(E2; 2^+ \rightarrow 0^+)$ transition is very accurate, and also very large, indicating the strength of this transition, with the transi-

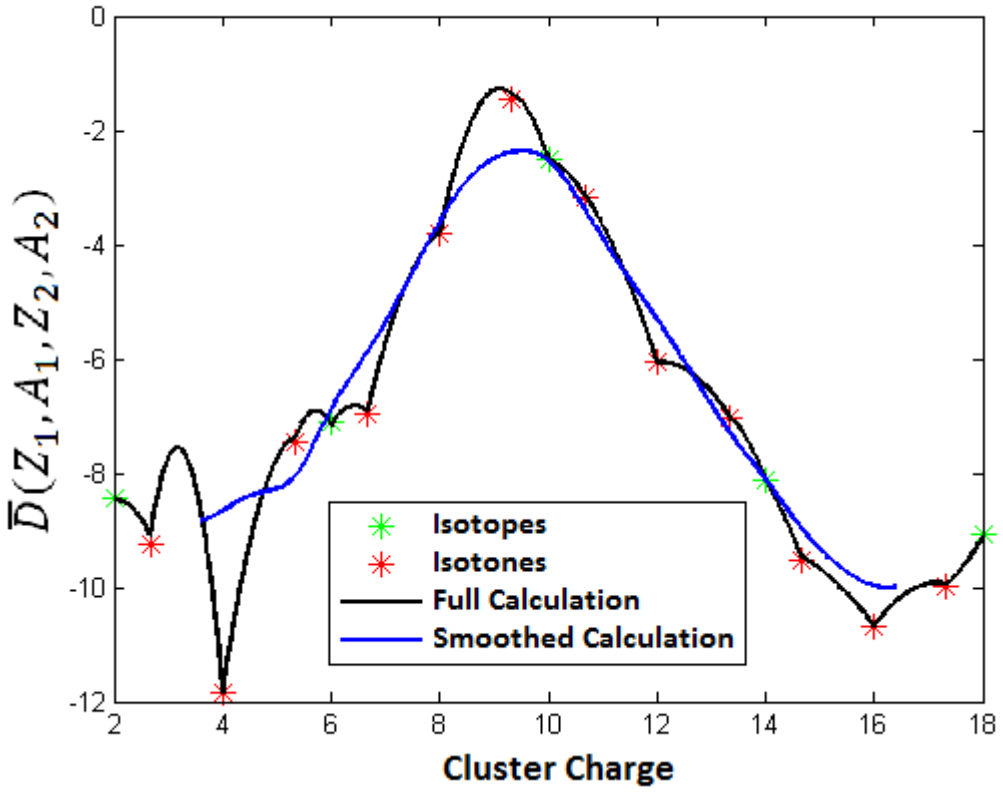

Figure 6.1: Calculations of $\bar{D}(Z_1, A_1, Z_2, A_2)$ as a function of cluster charge for ^{230}U. Isotopes are indicated with green crosses, isotones with red crosses and the full calculation is indicated with the black line. A smoothed calculation is indicated with a blue line.

Table 6.1: Cluster decompositions of ^{230}U with weighted probabilities and corresponding exotic decay half-lives.

Cluster Decomposition	Q[MeV]	P	$T_{1/2}^{calc}$[y]	$T_{1/2}^{expt}$[y]
$^{230}U \rightarrow ^{26}_{10}Ne + ^{204}_{82}Pb$	56.295	0.1064	6.1541×10^{24}	
$^{230}U \rightarrow ^{24}_{10}Ne + ^{206}_{82}Pb$	61.352	0.6536	2.0551×10^{14}	5.699×10^{14}
$^{230}U \rightarrow ^{24}_{8}O + ^{206}_{84}Po$	30.726	0.0336	3.3660×10^{59}	
$^{230}U \rightarrow ^{22}_{8}O + ^{208}_{84}Po$	39.800	0.2064	2.8530×10^{29}	

tion from the 4^+ to the 2^+ state, however, even stronger.

The last structure observable to measure is the energy spectrum. By calculating the energy spectrum for each individual core-cluster decomposition and then weighting them according to their probabilities to get a weighted spectrum, these results are compared to the experimental data for both the SE method and the BS Rule, and shown in table (6.3).

For the highest known excited state, E_{22}, the difference between calcula-

Table 6.2: $B(E2)$ values for each different core-cluster decomposition as well as the weighted average for ^{230}U. All values are shown in Weisskopf units [W.u.].

Core		$^{204}_{82}Pb$	$^{206}_{82}Pb$	$^{206}_{84}Po$	$^{208}_{84}Po$	
Cluster		$^{26}_{10}Ne$	$^{24}_{10}Ne$	$^{24}_{8}O$	$^{22}_{8}O$	
	$B(E2)^{expt}$	$B(E2)^{calc}$				$B(E2)^{avg}$
$B(E2; 2^+ \rightarrow 0^+)$	222	240	229	164	158	213
$B(E2; 4^+ \rightarrow 2^+)$		342	327	234	225	305

tion and experiment is $\sim$ 0.2 MeV, with both methods giving a very good approximation to the energy spectrum.

Table 6.3: Weighted energy levels calculated for ^{230}U by solving the SE and BS Rule. All values are shown in MeV.

L^π	E_L^{expt}	E_L^{SE}	E_L^{BS}
0^+	0.0	0.0	0.0
2^+	0.052	0.043	0.051
4^+	0.169	0.154	0.161
6^+	0.347	0.314	0.320
8^+	0.578	0.519	0.525
10^+	0.856	0.766	0.771
12^+	1.176	1.054	1.057
14^+	1.532	1.378	1.380
16^+	1.921	1.737	1.738
18^+	2.338	2.130	2.130
20^+	2.779	2.557	2.555
22^+	3.243	3.013	3.010
	χ^2	0.2308	0.2295

6.2 Uranium-232

The next isotope of Uranium under consideration is ^{232}U. Figure (6.3) shows the plot of $\bar{D}(Z_1, A_1, Z_2, A_2)$ from which the most likely cluster charge can be determined. The full calculation indicates a cluster charge of about $Z_2 \sim 9$, while the smoothed calculation takes into account the long tail towards the right of the peak and higher cluster charges, to give a mean cluster charge of $Z_2 = 9.92$.

Using the mean cluster charge, the four core-cluster decompositions can be determined. This is displayed in table (6.4) along with calculated and experimental exotic decay data [48]. The most likely cluster is that of ^{26}Ne, even though it has not been observed as an emitted cluster from ^{232}U. The

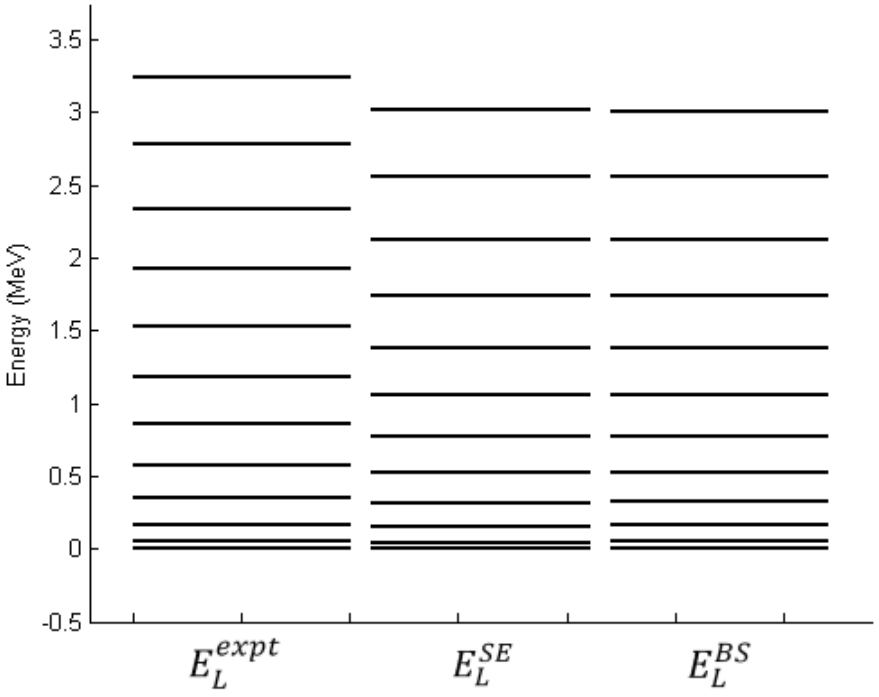

Figure 6.2: Weighted energy levels calculated for ^{230}U by solving the SE and BS Rule. All values are shown in MeV.

calculated half-life of ^{24}Ne, the second most favoured cluster, compares to the experimental data within a factor 2, which is a very good approximation.

Looking at the α-decay half-life of 68.9y, it is easy to see why ^{26}Ne is not observed as an emitted cluster, due to magnitude of its half-life compared to that of α-decay and the cluster decay of ^{24}Ne. The detection of the other two clusters, $^{22,24}O$, would also be nearly impossible, due to their large half-lives and very small preformation probabilities.

Table 6.4: Cluster decompositions of ^{232}U with weighted probabilities and corresponding exotic decay half-lives.

Cluster Decomposition	Q[MeV]	P	$T_{1/2}^{calc}$[y]	$T_{1/2}^{expt}[y]$
$^{232}U \rightarrow ^{26}_{10}Ne + ^{206}_{82}Pb$	57.967	0.528	1.7837×10^{21}	
$^{232}U \rightarrow ^{24}_{10}Ne + ^{208}_{82}Pb$	52.311	0.432	1.3733×10^{13}	7.742×10^{12}
$^{232}U \rightarrow ^{24}_{8}O + ^{208}_{84}Po$	33.010	0.022	6.2994×10^{51}	
$^{232}U \rightarrow ^{22}_{8}O + ^{210}_{84}Po$	41.780	0.018	1.6001×10^{27}	

The next structure observable, the reduced electromagnetic transition probabilities, are calculated for each separate core-cluster decomposition, and then the weighted value is compared to the experimental data [48] in table (6.5).

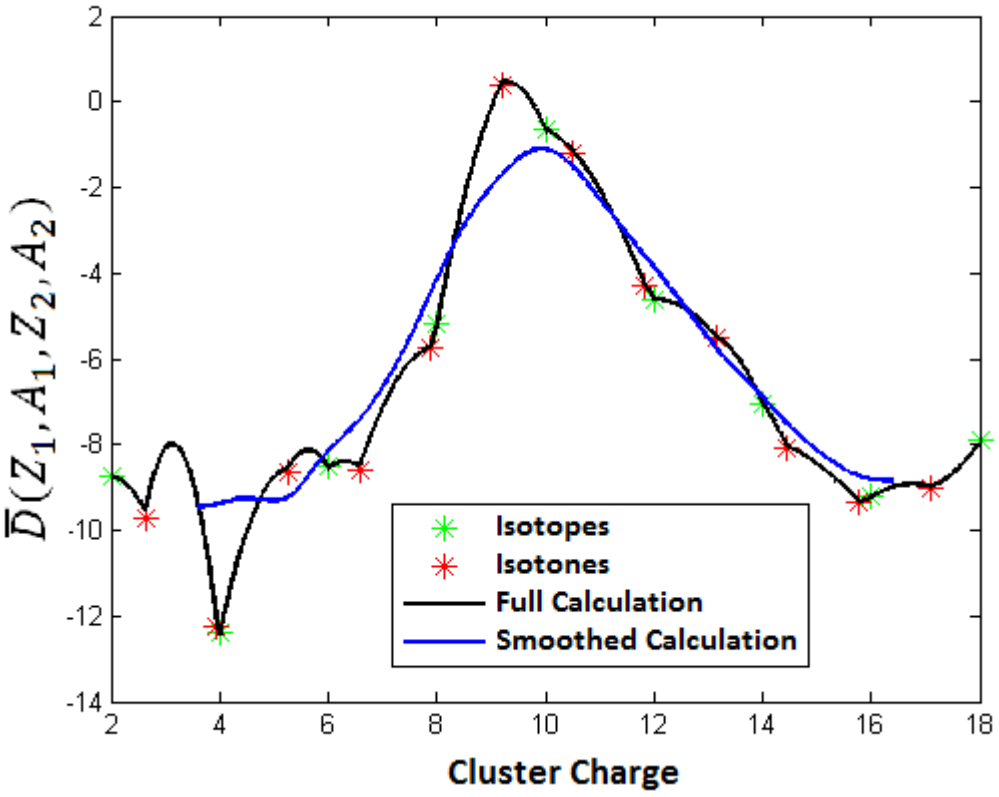

Figure 6.3: Calculations of $\bar{D}(Z_1, A_1, Z_2, A_2)$ as a function of cluster charge for ^{232}U. Isotopes are indicated with green crosses, isotones with red crosses and the full calculation is indicated with the black line. A smoothed calculation is indicated with a blue line.

The large $B(E2)$ values are due to the large clusters involved, and the calculated value for $B(E2; 2^+ \rightarrow 0^+)$ is in very good agreement with the experimental value.

Table 6.5: $B(E2)$ values for each different core-cluster decomposition as well as the weighted average for ^{232}U. All values are measured in Weisskopf units [W.u.].

Core		$^{206}_{82}Pb$	$^{208}_{82}Pb$	$^{208}_{84}Po$	$^{210}_{84}Po$	
Cluster		$^{26}_{10}Ne$	$^{24}_{10}Ne$	$^{24}_{8}O$	$^{22}_{8}O$	
	$B(E2)^{expt}$	$B(E2)^{calc}$				$B(E2)^{avg}$
$B(E2; 2^+ \rightarrow 0^+)$	241	239	228	164	157	231
$B(E2; 4^+ \rightarrow 2^+)$		341	325	234	224	330

The weighted energy spectrum, calculated by using both the SE method and the BS Rule, along with the experimental data, is shown in table (6.6). Comparing the highest known excited energy state, E_{20}, the difference between

calculated and experimental values are only ~ 0.15 MeV, which is a very good approximation. The SE and BS Rule results are again very similar.

Table 6.6: Weighted energy levels calculated for ^{232}U by solving the SE and BS Rule. All values are measured in MeV.

L^π	E_L^{expt}	E_L^{SE}	E_L^{BS}
0^+	0.0	0.0	0.0
2^+	0.048	0.041	0.047
4^+	0.157	0.149	0.154
6^+	0.323	0.305	0.310
8^+	0.541	0.505	0.510
10^+	0.806	0.748	0.752
12^+	1.112	1.030	1.033
14^+	1.454	1.347	1.351
16^+	1.828	1.700	1.705
18^+	2.232	2.087	2.092
20^+	2.660	2.507	2.512
	χ^2	0.0839	0.0773

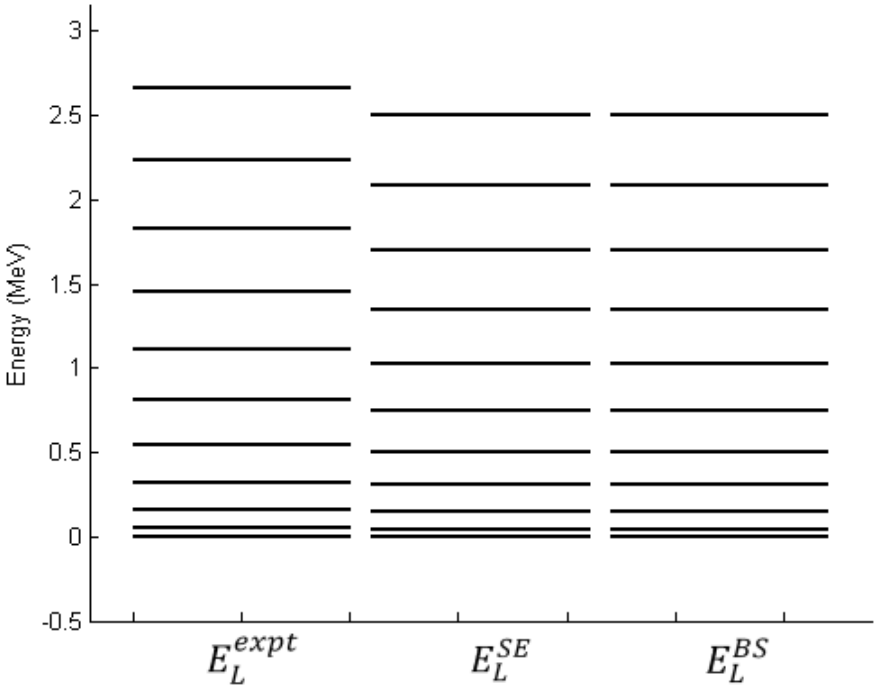

Figure 6.4: Weighted energy levels calculated for ^{232}U by solving the SE and BS Rule. All values are shown in MeV.

6.3 Uranium-234

The final Uranium isotope under consideration is ^{234}U, for which the plot of $\bar{D}(Z_1, A_1, Z_2, A_2)$ is shown in figure (6.5). The full calculation indicates a maximum at a cluster charge of $Z_2 \sim 10$, while the smoothed calculation has a similar maximum, at $Z_2 = 10.32$.

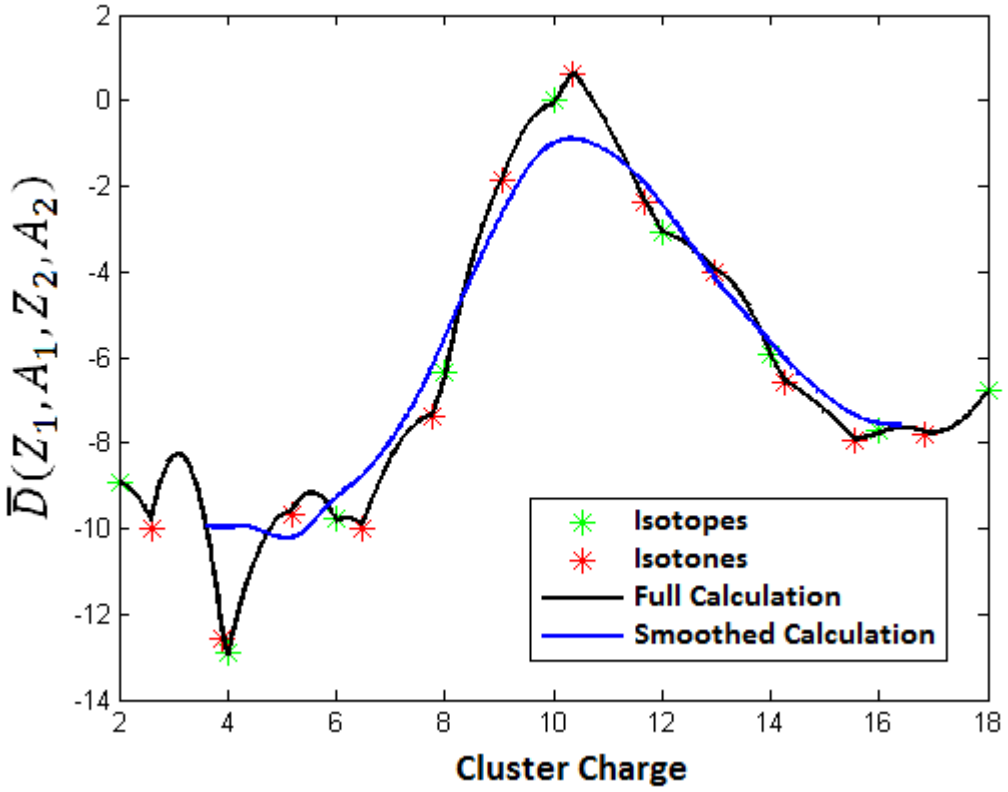

Figure 6.5: Calculations of $\bar{D}(Z_1, A_1, Z_2, A_2)$ as a function of cluster charge for ^{234}U. Isotopes are indicated with green crosses, isotones with red crosses and the full calculation is indicated with the black line. A smoothed calculation is indicated with a blue line.

The four core-cluster decompositions corresponding to the mean cluster charge, with their respective probabilities, are shown in table (6.7). Experimental data suggest that ^{234}U can decay by emitting three different clusters [49]. All three of these clusters, ^{28}Mg and $^{24,26}Ne$, are predicted by the model, and the calculated half-lives of both ^{28}Mg and ^{26}Ne are within a factor 2 of the experimental data. Only the calculated half-life of ^{24}Ne is inaccurate, about a factor 20 from the experimental data, but the suggested probability of finding a ^{24}Ne cluster structure within ^{234}U is very small.

The model indicates that the formation of ^{26}Ne is the most probable, and therefore, by also comparing the calculated half-lives to the experimental data, the experimentally observed decay of ^{234}U will most likely occur via the cluster decay of ^{26}Ne and not ^{24}Ne, since experiments cannot distinguish between the two, similarly to the cluster decay of ^{232}Th.

Comparing the exotic decay half-lives to the α-decay half-life of 2.455×10^5y, it is easy to explain why three different clusters are observed. Since the decay half-lives of ^{28}Mg and $^{24,26}Ne$ are of the same magnitude, their respective branching ratios relative to α-decay is similar, and therefore all three can be detected. The remaining cluster, ^{26}Mg, has an almost vanishingly small probability, and a much longer half-life, and is therefore not observed.

Table 6.7: Cluster decompositions of ^{234}U with weighted probabilities and corresponding exotic decay half-lives.

Cluster Decomposition	Q[MeV]	P	$T_{1/2}^{calc}$[y]	$T_{1/2}^{expt}[y]$
$^{234}U \rightarrow {}^{28}_{12}Mg + {}^{206}_{80}Hg$	74.111	0.1552	1.5783×10^{18}	1.754×10^{18}
$^{234}U \rightarrow {}^{26}_{12}Mg + {}^{208}_{80}Hg$	67.458	0.0048	1.993×10^{28}	
$^{234}U \rightarrow {}^{26}_{10}Ne + {}^{208}_{82}Pb$	59.465	0.8148	4.2952×10^{18}	2.728×10^{18}
$^{234}U \rightarrow {}^{24}_{10}Ne + {}^{210}_{82}Pb$	58.826	0.0252	4.8657×10^{19}	2.728×10^{18}

Comparing the experimental transition strength to the calculated value in table (6.8), it can be seen that the calculated value is somewhat greater. It is slightly surprising to see an experimental $B(E2; 2^+ \rightarrow 0^+)$ for ^{234}U which is smaller than for ^{232}U, since it has been seen that these values increase for increasing isotope mass. The calculated values follow the expected trend, since ^{234}U has a larger cluster charge and therefore larger $B(E2)$ value. Nevertheless, the calculated value is still a good approximation of the experimental value.

Table 6.8: $B(E2)$ values for each different core-cluster decomposition as well as the weighted average for ^{234}U. All values are measured in Weisskopf units [W.u.].

Core		${}^{206}_{80}Hg$	${}^{208}_{80}Hg$	${}^{208}_{82}Pb$	${}^{210}_{82}Pb$	
Cluster		${}^{28}_{12}Mg$	${}^{26}_{12}Mg$	${}^{26}_{10}Ne$	${}^{24}_{10}Ne$	
	$B(E2)^{expt}$	$B(E2)^{calc}$				$B(E2)^{avg}$
$B(E2; 2^+ \rightarrow 0^+)$	236	314	284	238	220	251
$B(E2; 4^+ \rightarrow 2^+)$		448	406	340	314	358

The final structure observable is the energy spectrum, and the weighted energy spectrum calculated by both the SE method and the BS Rule, along with the experimental data [49], is shown in table (6.9). Only comparing the highest known excited state, E_{30}, both calculated values are too large by ~ 0.15 MeV, with both methods giving similar results.

Table 6.9: Weighted energy levels calculated for ^{234}U by solving the SE and BS Rule. All values are measured in MeV.

L^π	E_L^{expt}	E_L^{SE}	E_L^{BS}
0^+	0.0	0.0	0.0
2^+	0.043	0.039	0.047
4^+	0.143	0.143	0.151
6^+	0.296	0.296	0.303
8^+	0.497	0.491	0.497
10^+	0.741	0.730	0.732
12^+	1.024	1.006	1.006
14^+	1.341	1.318	1.316
16^+	1.688	1.665	1.660
18^+	2.063	2.045	2.038
20^+	2.464	2.458	2.449
22^+	2.890	2.902	2.889
24^+	3.339	3.375	3.360
26^+	3.808	3.878	3.858
28^+	4.297	4.406	4.384
30^+	4.807	4.958	4.935
	χ^2	0.0430	0.0296

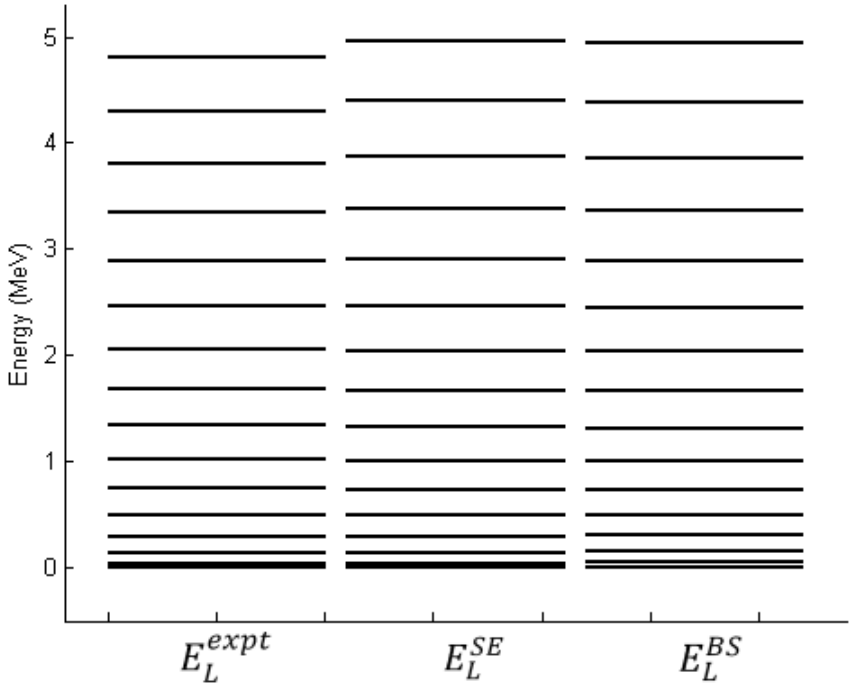

Figure 6.6: Weighted energy levels calculated for ^{234}U by solving the SE and BS Rule. All values are shown in MeV.

Chapter 7

Plutonium Isotopes

In order to establish the range of applicability of the current set of potential parameters, the next set of actinide nuclei, namely Plutonium, were investigated. By establishing the most likely core-cluster decompositions with associated probabilities, and calculating the exotic decay half-life, $B(E2)$ transition strength and energy spectra, the validity - not of the BCM, since that has already been established - but rather of the current set of potential parameters, can be determined.

To this end, the same parameters that were used for both Thorium and Uranium will be used on all Plutonium isotopes for which exotic decay have been observed experimentally.

7.1 Plutonium-236

The first, and lightest, of these isotopes, is ^{236}Pu. Figure (7.1) shows the plot of $\bar{D}(Z_1, A_1, Z_2, A_2)$ versus cluster charge, from which the mean cluster charge can be determined. The full calculation shows a very broad peak, with a maximum at $Z_2 \sim 10$, while the smoothed calculation shifts that maximum to a slightly larger cluster charge at $Z_2 = 11.71$. This is due to the broadening of the peak, especially towards larger cluster charges, away from the full calculation's maximum.

Having established the mean cluster charge, this can be decomposed into the four core-cluster decompositions with their respective probabilities. The result is shown in table (7.1), along with the calculated and experimental exotic decay half-life [50]. The most likely cluster component is ^{30}Mg, even though this cluster emission has not been observed experimentally. Comparing the half-life of this cluster to the α-decay half-life, 2.858y, shows the reason why; the branching ratio for the cluster emission of ^{30}Mg relative to α-decay will be vanishingly small, making it almost impossible to detect.

Furthermore, the cluster emission of ^{28}Mg, which has been detected experimentally, but has a smaller probability of forming, has a half-life 10^5 times

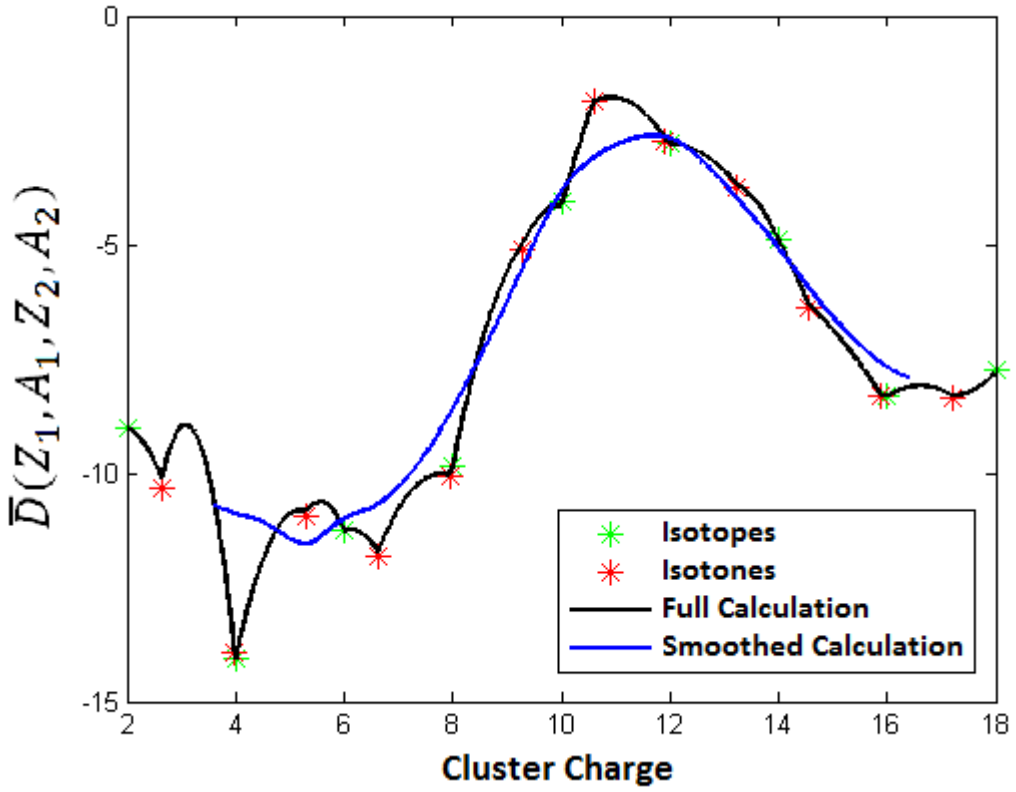

Figure 7.1: Calculations of $\bar{D}(Z_1, A_1, Z_2, A_2)$ as a function of cluster charge for ^{236}Pu. Isotopes are indicated with green crosses, isotones with red crosses and the full calculation is indicated with the black line. A smoothed calculation is indicated with a blue line.

smaller than that of ^{30}Mg, making it much easier to detect. The calculated half-life for ^{28}Mg also compares very well to the experimental value.

The other two clusters, $^{26,28}Ne$, have, along with small preformation probabilities, extremely long half-lives, making them virtually impossible to detect.

Table 7.1: Cluster decompositions of ^{236}Pu with weighted probabilities and corresponding exotic decay half-lives.

Cluster Decomposition	Q[MeV]	P	$T_{1/2}^{calc}$[y]	$T_{1/2}^{expt}$[y]
$^{236}Pu \rightarrow ^{30}_{12}Mg + ^{206}_{82}Pb$	75.599	0.731	7.3055×10^{19}	
$^{236}Pu \rightarrow ^{28}_{12}Mg + ^{208}_{82}Pb$	79.670	0.129	1.1442×10^{14}	1.429×10^{14}
$^{236}Pu \rightarrow ^{28}_{10}Ne + ^{208}_{84}Po$	49.128	0.119	4.7087×10^{44}	
$^{236}Pu \rightarrow ^{26}_{10}Ne + ^{208}_{84}Po$	58.426	0.021	9.7153×10^{24}	

By calculating the $B(E2)$ transition strengths for each core-cluster decomposition, a weighted $B(E2)$ value can then be calculated by weighting each

separate value. This is done in table (7.2). Unfortunately, no experimental data exists to compare these calculated values to.

Table 7.2: $B(E2)$ values for each different core-cluster decomposition as well as the weighted average for ^{236}Pu. All vlaues are measured in Weisskopf units [W.u.].

Core		$^{206}_{82}Pb$	$^{208}_{82}Pb$	$^{208}_{84}Po$	$^{208}_{84}Po$	
Cluster		$^{30}_{12}Mg$	$^{28}_{12}Mg$	$^{28}_{10}Ne$	$^{26}_{10}Ne$	
	$B(E2)^{expt}$	$B(E2)^{calc}$				$B(E2)^{avg}$
$B(E2; 2^+ \to 0^+)$		329	315	237	231	314
$B(E2; 4^+ \to 2^+)$		470	450	339	330	449

Finally, the weighted energy spectrum can be calculated using both the SE method and the BS Rule, and compared to experimental data [50]. These results are shown in table (7.3), and show that both calculated methods differ in energy by about 0.25 MeV when comparing the highest known excited energy state.

Table 7.3: Weighted energy levels calculated for ^{236}Pu by solving the SE and BS Rule. All values are measured in MeV.

L^π	E_L^{expt}	E_L^{SE}	E_L^{BS}
0^+	0.0	0.0	0.0
2^+	0.045	0.032	0.040
4^+	0.147	0.128	0.134
6^+	0.306	0.265	0.272
8^+	0.516	0.443	0.449
10^+	0.774	0.660	0.663
12^+	1.074	0.911	0.913
14^+	1.414	1.195	1.196
16^+	1.786	1.512	1.512
	χ^2	0.1701	0.1664

7.2 Plutonium-238

The next isotope under consideration is ^{238}Pu, for which the plot of $\bar{D}(Z_1, A_1, Z_2, A_2)$ can be seen in figure (7.3). The full calculation shows a maximum at $Z_2 \sim 12$, while the shape of the peak means that the smoothed calculation's maximum is at $Z_2 = 12.32$. This is due to the fact that the peak is smeared out towards heavier cluster charges, which shifts the maximum in that direction.

Using the mean cluster charge obtained from the smoothed calculation, the four core-cluster decompositions can be written down along with their

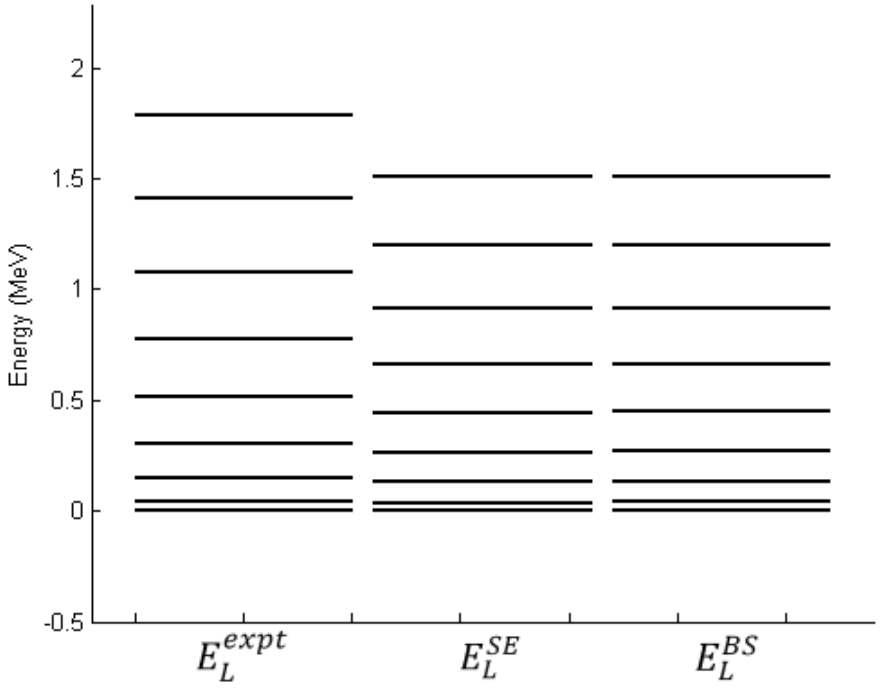

Figure 7.2: Weighted energy levels calculated for ^{236}Pu by solving the SE and BS Rule. All values are shown in MeV.

respective probabilities. Table (7.4) shows these four possibilities, along with their calculated exotic decay half-lives, as well as available experimental data [51].

The most likely cluster is that of ^{30}Mg, and the calculated half-life corresponds to the experimental half-life within a factor of 2. The second most likely cluster, ^{32}Mg, has not been observed to be emitted from ^{238}Pu, but comparing its half-life to the α-decay half-life, 87.7y, it is clear that the branching ratio relative to α-decay is vanishingly small, making it near impossible to detect the cluster decay of ^{32}Mg.

In addition to the cluster decay of ^{30}Mg, ^{238}Pu can also decay via the emission of ^{32}Si. This emission has a half-life comparable to that of ^{30}Mg, although the calculated half-life is incorrect by a factor of about 7, and is not considered accurate enough, but this inaccuracy can be accounted for by the small preformation probability. The remaining cluster, ^{34}Si, has a very small preformation probability, and a very long half-life, the combination of the two making it too difficult to detect this cluster decay experimentally.

The decay of ^{28}Mg from ^{238}Pu has been observed experimentally, however, but is not predicted within the present model, being the only such failure in all cases considered.

Table (7.5) shows the calculated $B(E2)$ values for each separate core-cluster

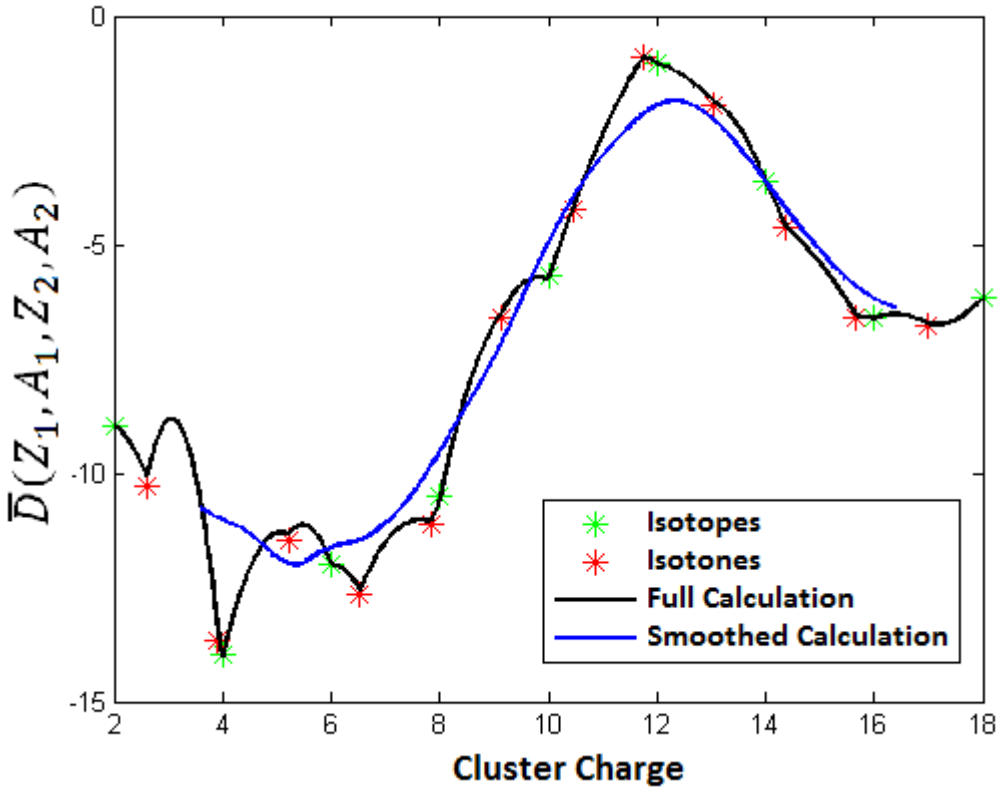

Figure 7.3: Calculations of $\bar{D}(Z_1, A_1, Z_2, A_2)$ as a function of cluster charge for ^{238}Pu. Isotopes are indicated with green crosses, isotones with red crosses and the full calculation is indicated with the black line. A smoothed calculation is indicated with a blue line.

Table 7.4: Cluster decompositions of ^{238}Pu with weighted probabilities and corresponding exotic decay half-lives.

Cluster Decomposition	Q[MeV]	P	$T_{1/2}^{calc}$[y]	$T_{1/2}^{expt}$[y]
$^{238}Pu \rightarrow ^{34}_{14}Si + ^{204}_{80}Hg$	90.812	0.0704	1.4483×10^{20}	
$^{238}Pu \rightarrow ^{32}_{14}Si + ^{206}_{80}Hg$	91.191	0.0896	4.4613×10^{18}	6.271×10^{17}
$^{238}Pu \rightarrow ^{32}_{12}Mg + ^{206}_{82}Pb$	70.905	0.3696	3.6959×10^{28}	
$^{238}Pu \rightarrow ^{30}_{12}Mg + ^{208}_{82}Pb$	76.824	0.4704	2.5147×10^{18}	1.463×10^{18}

decomposition as well as the weighted value. The latter is in relative poor agreement with its experimental counterpart value [51], but still gives a reasonable indication of the $B(E2)$ values.

In order to get a better theoretical prediction, it seems that the potential parameters should get adjusted. Doing this will not be easy however, since the exotic decay half-life is the most sensitive quantity, and, for ^{30}Mg decay, gives accurate results. More than one parameter will therefore have to be adjusted

in order to reproduce both the decay half-life and $B(E2)$ values accurately.

Table 7.5: $B(E2)$ values for each different core-cluster decomposition as well as the weighted average for ^{238}Pu. All values are measured in Weisskopf units [W.u.].

Core		$^{204}_{80}Hg$	$^{206}_{80}Hg$	$^{206}_{82}Pb$	$^{208}_{82}Pb$	
Cluster		$^{34}_{14}Si$	$^{32}_{14}Si$	$^{32}_{12}Mg$	$^{30}_{12}Mg$	
	$B(E2)^{expt}$	$B(E2)^{calc}$				$B(E2)^{avg}$
$B(E2; 2^+ \rightarrow 0^+)$	285	436	412	338	327	347
$B(E2; 4^+ \rightarrow 2^+)$		623	589	483	467	495

The last structure observable to be computed is the energy spectrum. Using the same potential parameters, the energy spectrum is calculated using both the SE method and the BS Rule, compared to the experimental data and displayed in table (7.6). When comparing the highest known excited state, E_{26}, the difference between the calculated values and the experimental data is ~ 0.8 MeV, which is not nearly as accurate as all other isotope data was. Similarly to the $B(E2)$ values, this indicates that the potential parameters are not valid in this region, and will have to be adjusted in order to accurately approximate the energy spectrum.

When adjusting these parameters, however, it needs to be taken into account that the exotic decay half-life needs to stay approximately the same, the $B(E2)$ values need to decrease, and the energy spectrum needs to increase. Looking at Tables (5.2, 5.3, 5.4), it seems that the potential depth is the only parameter which, when increased, decreases the $B(E2)$ value and increases the energy levels. Unfortunately, changing only the potential depth means that the half-life will also change, and since this observable is more sensitive to parameter changes than the $B(E2)$ value and energy level, either the diffuseness or mixing parameter, or perhaps even both, will also have to be adjusted.

Another possible solution to this problem is by selecting smaller clusters, since this will decrease the calculated $B(E2)$ values and increase the energy levels.

By investigating figure (7.3) it can be seen that the full calculation predicts a mean cluster charge smaller than $Z_2 = 12$, while the smoothed calculation predicts a cluster charge $Z_2 > 12$. The smoothed calculation therefore predicts greater cluster charges, and by rather using the full calculation's mean cluster charge, smaller clusters will form. As shown below, this results in smaller $B(E2)$ values and greater energy levels.

The possible core-cluster decompositions, with weighted probability and calculated half-lives, obtained when using the mean cluster charge from the full calculation are shown in table (7.7). It is easy to see that smaller clusters form in this case, with isotopes of Ne forming instead of Si, along with isotopes of Mg. An immediate shortcoming is the absence of the experimentally observed emission of $^{32}_{14}Si$, which was predicted when using the mean cluster charge

Table 7.6: Weighted energy levels calculated for ^{238}Pu by solving the SE and BS Rule. All values are measured in MeV.

L^π	E_L^{expt}	E_L^{SE}	E_L^{BS}
0^+	0.0	0.0	0.0
2^+	0.044	0.029	0.039
4^+	0.146	0.121	0.130
6^+	0.303	0.254	0.263
8^+	0.514	0.427	0.434
10^+	0.773	0.636	0.642
12^+	1.080	0.880	0.884
14^+	1.429	1.156	1.159
16^+	1.819	1.464	1.466
18^+	2.245	1.802	1.803
20^+	2.706	2.171	2.170
22^+	3.199	2.567	2.565
24^+	3.721	2.991	2.987
26^+	4.265	3.441	3.436
	χ^2	2.3655	2.3698

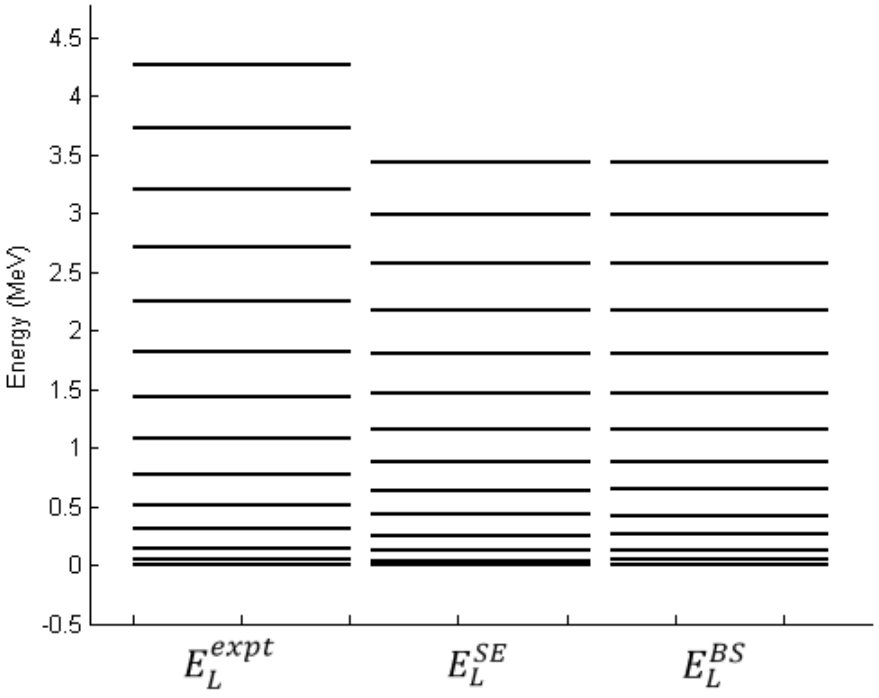

Figure 7.4: Weighted energy levels calculated for ^{238}Pu by solving the SE and BS Rule. All values are shown in MeV.

Table 7.7: Cluster decompositions of ^{238}Pu with weighted probabilities and corresponding exotic decay half-lives, calculated by using the mean cluster charge obtained from the full calculation.

Cluster Decomposition	Q[MeV]	P	$T_{1/2}^{calc}$[y]	$T_{1/2}^{expt}[y]$
$^{238}Pu \rightarrow ^{32}_{12}Mg + ^{206}_{82}Pb$	70.905	0.045	3.0353×10^{29}	
$^{238}Pu \rightarrow ^{30}_{12}Mg + ^{208}_{82}Pb$	76.824	0.855	1.3830×10^{18}	1.463×10^{18}
$^{238}Pu \rightarrow ^{30}_{10}Ne + ^{208}_{88}Po$	40.532	0.005	6.8585×10^{72}	
$^{238}Pu \rightarrow ^{28}_{10}Ne + ^{210}_{84}Po$	51.037	0.095	3.9704×10^{40}	

obtained from the smoothed calculation. This is an indication of the success of the smoothed calculation; although extremely simplistic, it correctly increases the mean cluster charge, depending on the behaviour of surrounding core-cluster decompositions.

Although a decrease in calculated $B(E2)$ value, $B(E2) = 319$ W.u., and an increase in energy levels, $E_{26} = 3.535$ MeV, are observed when using the smaller clusters from table (7.7), the failure to predict the cluster emission of $^{32}_{14}Si$ indicates that the problem does not lie in the fact that the smoothed calculation predicts heavier clusters, but rather that the chosen set of parameters are no longer ideal for this nucleus.

7.3 Plutonium-240

The final Plutonium isotope that will be tested, is ^{240}Pu, for which the plot of $\bar{D}(Z_1, A_1, Z_2, A_2)$ as a function of cluster charge is shown in figure (7.5). The maximum is seen to be near $Z_2 = 13$, when considering the full calculation, but due to the relative heights of the curve to the left and right of the peak, the smoothed calculation gives a maximum of $Z_2 = 13.12$.

Using this mean cluster charge, the corresponding core-cluster decompositions are given in table (7.8), along with their respective preformation probabilities and calculated exotic decay half-life. The most likely cluster is ^{34}Si, a cluster which has been observed to be emitted by ^{240}Pu. The calculated half-life is within a factor 3 of the experimental value [52], which is considered to be an accurate approximation.

^{32}Mg is a cluster that also has a large probability of appearing within the structure of ^{240}Pu, but when comparing its half-life to that of α-decay, 6561y, it can be explained why it is not observed experimentally to be emitted. Due to the competition from both α-particles and the cluster decay of ^{34}Si, the half-life for the cluster emission of ^{32}Mg is too long to be observed experimentally, and the same argument is valid for the other two clusters, ^{36}Si and ^{34}Mg, in addition to their preformation probabilities being very small.

The calculated values of the reduced electromagnetic transition probabilities are shown in table (7.9), along with known experimental data [52]. Similar

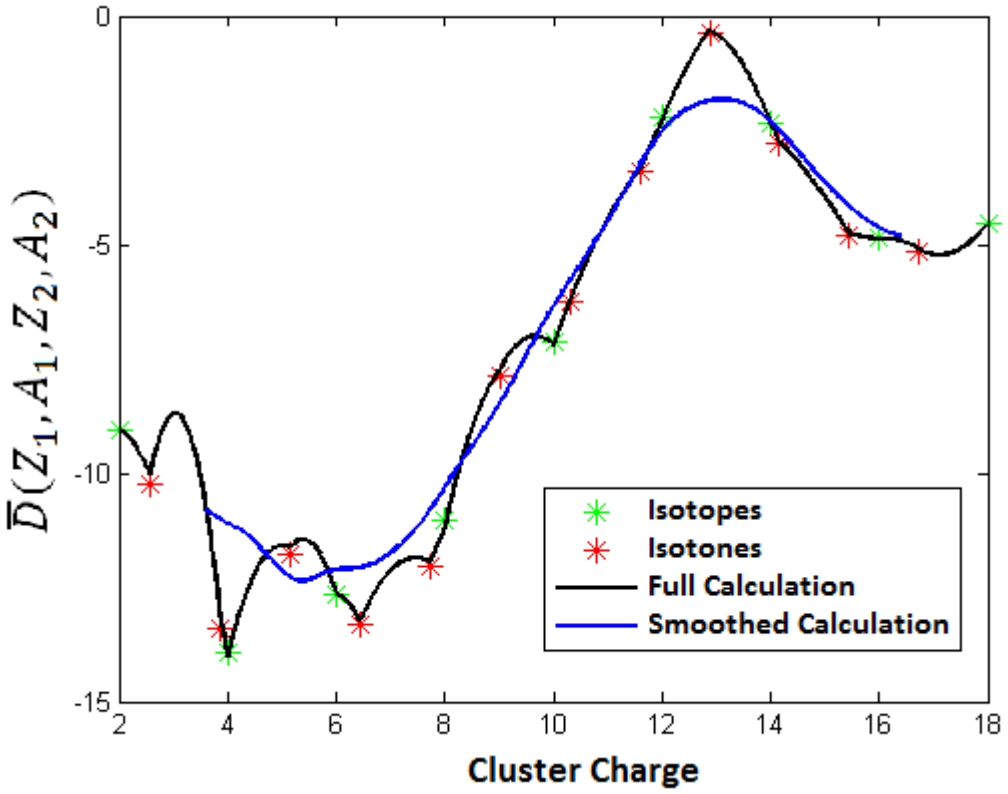

Figure 7.5: Calculations of $\bar{D}(Z_1, A_1, Z_2, A_2)$ as a function of cluster charge for ^{240}Pu. Isotopes are indicated with green crosses, isotones with red crosses and the full calculation is indicated with the black line. A smoothed calculation is indicated with a blue line.

Table 7.8: Cluster decompositions of ^{240}Pu with weighted probabilities and corresponding exotic decay half-lives.

Cluster Decomposition	Q[MeV]	P	$T_{1/2}^{calc}$[y]	$T_{1/2}^{expt}$[y]
$^{240}Pu \rightarrow ^{36}_{14}Si + ^{204}_{80}Hg$	87.300	0.1064	4.5305×10^{25}	
$^{240}Pu \rightarrow ^{34}_{14}Si + ^{206}_{80}Hg$	91.029	0.4536	1.4090×10^{19}	5.047×10^{18}
$^{240}Pu \rightarrow ^{34}_{12}Mg + ^{206}_{82}Pb$	65.104	0.0836	8.6229×10^{40}	
$^{240}Pu \rightarrow ^{32}_{12}Mg + ^{208}_{82}Pb$	72.830	0.3564	3.8112×10^{25}	

to ^{238}Pu, the calculated weighted value for $B(E2; 2^+ \rightarrow 0^+)$ is a lot greater than the experimental value, and parameter adjusting may be necessary to achieve a more accurate result.

Finally, the weighted energy spectrum is calculated by both the SE method and the BS Rule and compared to experimental data in Table (7.10). Once more, similar to ^{238}Pu, the calculated energy levels are lower in energy than the experimental levels, and a change in potential parameters will be necessary to

Table 7.9: $B(E2)$ values for each different core-cluster decomposition as well as the weighted average for ^{240}Pu. All values are measured in Weisskopf units [W.u.].

Core		$^{204}_{80}Hg$	$^{206}_{80}Hg$	$^{206}_{82}Pb$	$^{208}_{82}Pb$	
Cluster		$^{36}_{14}Si$	$^{34}_{14}Si$	$^{34}_{12}Mg$	$^{32}_{12}Mg$	
	$B(E2)^{expt}$	$B(E2)^{calc}$				$B(E2)^{avg}$
$B(E2; 2^+ \rightarrow 0^+)$	287	448	431	347	338	393
$B(E2; 4^+ \rightarrow 2^+)$		640	616	495	482	561

adjust these values. As discussed earlier, however, more than one parameter will have to be changed, since the ^{34}Si decay half-life is approximately correct.

Table 7.10: Weighted energy levels calculated for ^{240}Pu by solving the SE and BS Rule. All values are measured in MeV.

L^π	E_L^{expt}	E_L^{SE}	E_L^{BS}
0^+	0.0	0.0	0.0
2^+	0.043	0.026	0.038
4^+	0.142	0.113	0.125
6^+	0.294	0.241	0.252
8^+	0.497	0.406	0.416
10^+	0.747	0.606	0.614
12^+	1.041	0.839	0.847
14^+	1.375	1.105	1.111
16^+	1.746	1.401	1.406
18^+	2.152	1.726	1.730
20^+	2.590	2.081	2.084
22^+	3.060	2.462	2.464
24^+	3.559	2.872	2.872
26^+	4.086	3.307	3.306
28^+	4.639	3.767	3.765
30^+	5.220	4.252	4.249
32^+	5.819	4.760	4.756
	χ^2	4.9616	4.9557

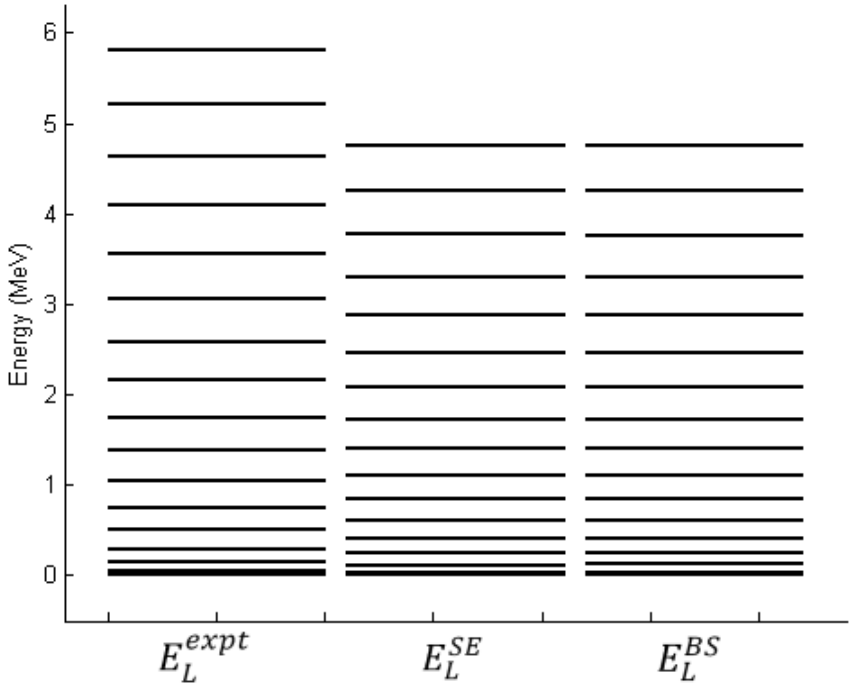

Figure 7.6: Weighted energy levels calculated for ^{240}Pu by solving the SE and BS Rule. All values are shown in MeV.

Chapter 8

Radium Isotopes

After testing the validity of the current set of potential parameters to Plutonium isotopes, and determining that it is not ideal in reproducing structure observables for such heavy nuclei, it would be useful to further extend the range of applicability of the model and set of parameters, but rather to lighter nuclei. To this end, it is applied to Radium isotopes which are known to emit clusters in exotic decay.

8.1 Radium-222

The first of these isotopes is ^{222}Ra, for which the plot of $\bar{D}(Z_1, A_1, Z_2, A_2)$ is shown in figure (8.1). The full calculation shows a distinct maximum at $Z_2 \sim 5.5$, with a few smaller peaks surrounding it. These surrounding peaks impacts the smoothed curve, although the relative differences in height still produces a mean cluster charge of $Z_2 = 5.66$.

After determining the mean cluster charge, the set of four core-cluster decompositions, with accompanying probabilities, can be determined. These are shown in table (8.1), along with the calculated decay half-lives, as well as the known experimental data [42]. The most likely cluster structure to appear in ^{222}Ra is ^{14}C, which is also the observed cluster emitted from ^{222}Ra. The calculated half-life, however, is incorrect by a factor of about 60, which is a poor result. This suggests that the current set of parameters is not good enough to reproduce the exotic decay half-life for nuclei lighter than Thorium, which were used to determine the current set of parameters.

^{16}C also has a very high probability of forming within the nucleus, but its half-life is extremely long, especially when compared to the α-decay half-life of 38.0s, and will therefore not be detected.

Of the other two clusters, ^{14}Be is not a possible mode of decay, due to the negative Q-value, while the probability of ^{12}Be forming is very low and its half-life too long.

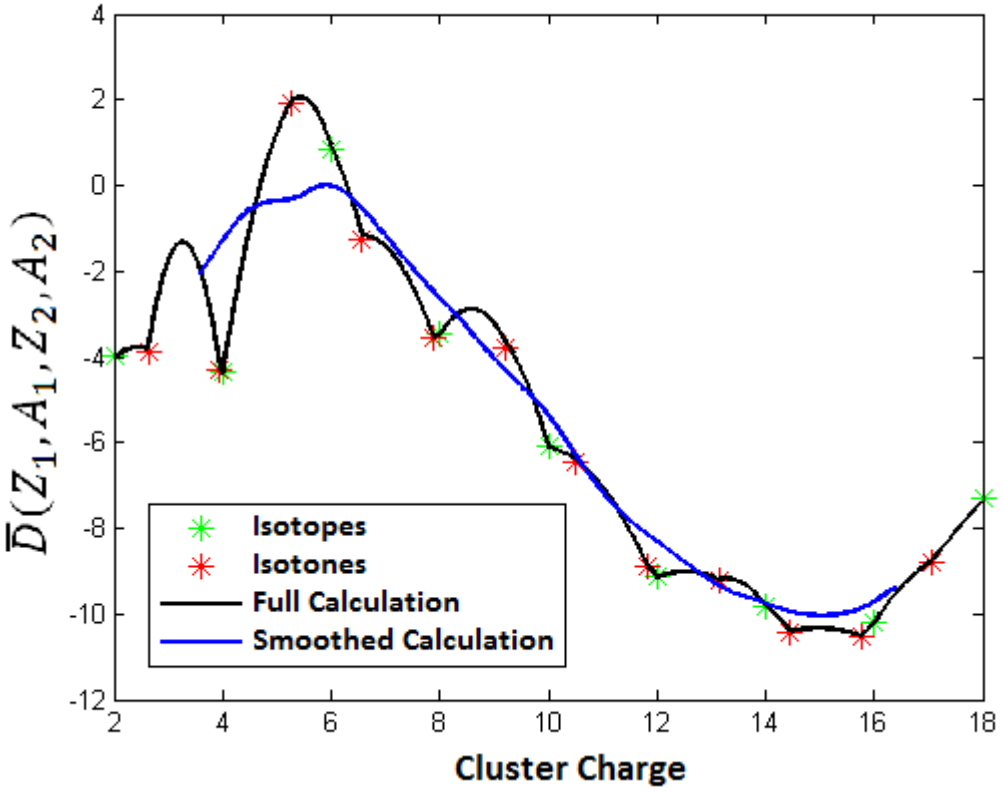

Figure 8.1: Calculations of $\bar{D}(Z_1, A_1, Z_2, A_2)$ as a function of cluster charge for ^{222}Ra. Isotopes are indicated with green crosses, isotones with red crosses and the full calculation is indicated with the black line. A smoothed calculation is indicated with a blue line.

Table 8.1: Cluster decompositions of ^{222}Ra with weighted probabilities and corresponding exotic decay half-lives.

Cluster Decomposition	Q[MeV]	P	$T_{1/2}^{calc}$[y]	$T_{1/2}^{expt}$[y]
$^{222}Ra \rightarrow ^{16}_{6}C + ^{206}_{82}Pb$	24.413	0.2567	2.4568×10^{27}	
$^{222}Ra \rightarrow ^{14}_{6}C + ^{208}_{82}Pb$	33.050	0.5733	6594.2	105.7
$^{222}Ra \rightarrow ^{14}_{4}Be + ^{208}_{84}Po$	-8.164	0.0526		
$^{222}Ra \rightarrow ^{12}_{4}Be + ^{210}_{84}Po$	5.198	0.1174	7.2594×10^{103}	

By calculating the separate $B(E2)$ values and using them to generate a weighted $B(E2)$ value, good agreement with experiment for the $B(E2; 2^+ \rightarrow 0^+)$ case is found, as can be seen in table (8.2). Although the calculated value is slightly too small, it is still a good approximation. By reducing the potential depth, however, this value will increase, and the exotic decay half-life will decrease, possibly increasing the accuracy of both observables.

The low experimental value of the $B(E2; 4^+ \rightarrow 2^+)$ transition is something

of a mystery. Normally, as was seen with all other nuclei tested, this transition will have a higher transition strength than the $B(E2; 2^+ \rightarrow 0^+)$ transition. The BCM model fails in reproducing this value, and rather produces what would have been expected; a value higher than what was calculated for the $B(E2; 2^+ \rightarrow 0^+)$ transition.

Table 8.2: $B(E2)$ values for each different core-cluster decomposition as well as the weighted average for ^{222}Ra. All values are measured in Weisskopf units W.u.].

Core		$^{206}_{82}Pb$	$^{208}_{82}Pb$	$^{208}_{84}Po$	$^{210}_{84}Po$	
Cluster		$^{16}_{6}C$	$^{14}_{6}C$	$^{14}_{4}Be$	$^{12}_{4}Be$	
	$B(E2)^{expt}$	$B(E2)^{calc}$				$B(E2)^{avg}$
$B(E2; 2^+ \rightarrow 0^+)$	111	90	86	44	41	80
$B(E2; 4^+ \rightarrow 2^+)$	11.83	128	122	63	59	113

The last structure observable to be measured, is the energy spectrum. The weighted energy spectrum is calculated using both the SE method and the BS Rule, and compared against the experimental data in table (8.3). Comparing the highest known excited state, E_{20}, the calculated value of both methods are within 0.1 MeV of the experimental value, which is a very good approximation.

Table 8.3: Weighted energy levels calculated for ^{222}Ra by solving the SE and BS Rule. All values are measured in MeV.

L^π	E_L^{expt}	E_L^{SE}	E_L^{BS}
0^+	0.0	0.0	0.0
2^+	0.111	0.071	0.076
4^+	0.301	0.227	0.232
6^+	0.550	0.449	0.451
8^+	0.843	0.729	0.731
10^+	1.173	1.061	1.062
12^+	1.537	1.441	1.441
14^+	1.933	1.867	1.865
16^+	1.359	2.331	2.327
18^+	2.811	2.831	2.826
20^+	3.288	3.363	3.357
	χ^2	0.0632	0.0608

8.2 Radium-224

The final isotope under investigation is ^{224}Ra, for which the plot of $\bar{D}(Z_1, A_1, Z_2, A_2)$ as a function of cluster charge is shown in figure (8.3). The full calculation

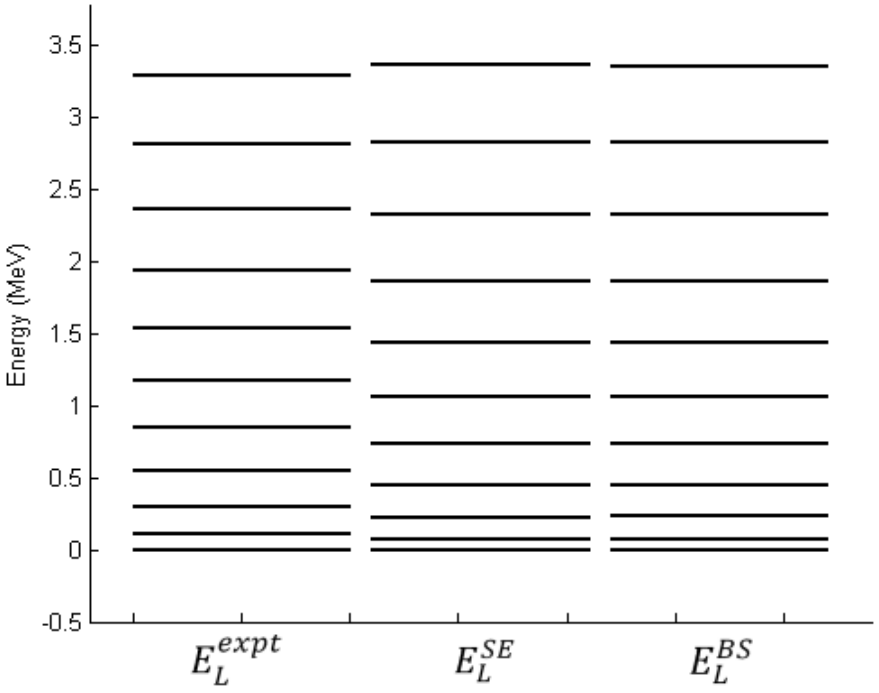

Figure 8.2: Weighted energy levels calculated for ^{222}Ra by solving the SE and BS Rule. All values are measured in MeV.

gives a maximum at $Z_2 \sim 5.5$, but due to the long tail of the peak towards heavier clusters, the smoothed calculation is shifted slightly towards the right, and has a maximum at $Z_2 = 6.30$.

Table (8.4) shows the four possible decompositions obtained from the mean cluster charge, with their appropriate probabilities. The most likely cluster is ^{16}C, but it has not yet been observed that ^{224}Ra decays via the emission of such a cluster.

The only observed cluster decay of ^{224}Ra is via the emission of ^{14}C [43]. The calculated half-life for this decay is about a factor 10 greater than the experimental value, indicating an error in the potential parameters; a shallower potential well will be needed to model this decay more accurately.

Comparing the other decays to the α-decay half-life, and to the exotic decay half-life of ^{14}C, explains the absence of experimental observation of their decay. The α-decay half-life is measured as 3.66d, which implies that all other decay half-lives are too long to be observed; the competition from α-decay and ^{14}C-decay is too great to allow the experimental observation of further cluster emission.

By calculating the $B(E2)$ values for each separate core-cluster decomposition and then calculating a weighted value using their respective probabilities, the weighted $B(E2)$ value can be compared to the experimental val-

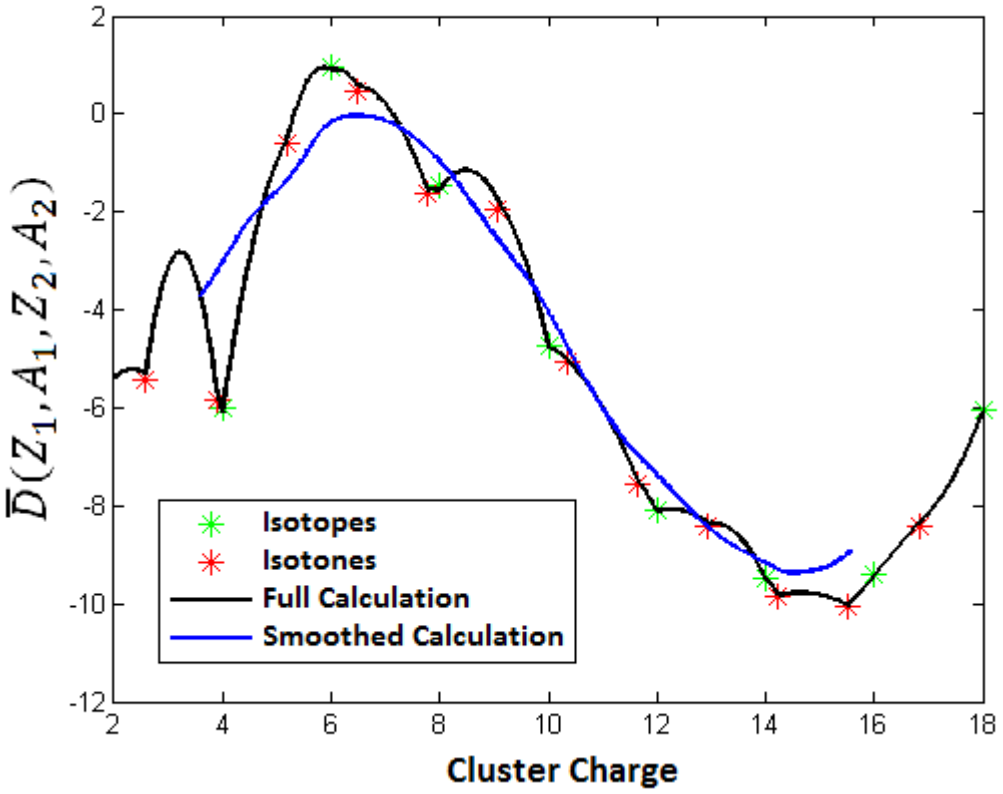

Figure 8.3: Calculations of $\bar{D}(Z_1, A_1, Z_2, A_2)$ as a function of cluster charge for ^{224}Ra. Isotopes are indicated with green crosses, isotones with red crosses and the full calculation is indicated with the black line. A smoothed calculation is indicated with a blue line.

Table 8.4: Cluster decompositions of ^{224}Ra with weighted probabilities and corresponding exotic decay half-lives.

Cluster Decomposition	Q[MeV]	P	$T_{1/2}^{calc}$[y]	$T_{1/2}^{expt}$[y]
$^{224}Ra \rightarrow ^{18}_{8}O + ^{206}_{80}Hg$	40.554	0.1280	1.0311×10^{18}	
$^{224}Ra \rightarrow ^{16}_{8}O + ^{208}_{80}Hg$	36.661	0.0200	1.5742×10^{24}	
$^{224}Ra \rightarrow ^{16}_{6}C + ^{208}_{82}Pb$	26.882	0.7371	5.8643×10^{19}	
$^{224}Ra \rightarrow ^{14}_{6}C + ^{210}_{82}Pb$	30.536	0.1149	2.2708×10^{9}	2.507×10^{8}

ues, as is shown in table (8.5). Interestingly, both the $B(E2; 2^+ \rightarrow 0^+)$ and $B(E2; 4^+ \rightarrow 2^+)$ are almost exactly that of the experimental values. This is an indication of the power of the BCM; with a very simple choice of potential and the right parameters, complicated observables such as transition probabilities can be reproduced. It is also notable that no anomaly involving the $B(E2; 4^+ \rightarrow 2^+)$ transition is seen for ^{224}Ra as is the case for ^{222}Ra.

Finally, the weighted energy spectrum can be calculated in two methods;

Table 8.5: $B(E2)$ values for each different core-cluster decomposition as well as the weighted average for ^{224}Ra. All values are measured in Weisskopf units [W.u.].

Core		$^{206}_{80}Hg$	$^{208}_{80}Hg$	$^{208}_{82}Pb$	$^{210}_{82}Pb$	
Cluster		$^{18}_{8}O$	$^{16}_{8}O$	$^{16}_{6}C$	$^{14}_{6}C$	
	$B(E2)^{expt}$	$B(E2)^{calc}$				$B(E2)^{avg}$
$B(E2; 2^+ \rightarrow 0^+)$	97	140	126	90	83	96
$B(E2; 4^+ \rightarrow 2^+)$	138	200	179	128	118	137

the SE method and by solving the BS Rule. These spectra are then compared to the experimental data in table (8.6). Comparing the highest known energy state, E_{12}, it can be seen that both calculated methods compare extremely well with the measured value, with only a difference of about 0.05 MeV, which is a very good approximation to the energy spectrum.

Table 8.6: Weighted energy levels calculated for ^{224}Ra by solving the SE and BS Rule. All values are measured in MeV.

L^π	E_L^{expt}	E_L^{SE}	E_L^{BS}
0^+	0.0	0.0	0.0
2^+	0.084	0.064	0.068
4^+	0.251	0.210	0.213
6^+	0.479	0.418	0.421
8^+	0.755	0.683	0.683
10^+	1.067	0.997	0.997
12^+	1.414	1.358	1.357
	χ^2	0.0190	0.0184

From the investigation of these structure observables, it was seen that, although the $B(E2)$ values and energy spectrum are very accurate, the exotic decay half-life is not as good, with the calculated value differing from the experimental value by a factor of about 10. This problem should be easy to solve; since the decay half-life is more sensitive to the potential parameters than the transition probability and the energy spectrum, a slight reduction in potential depth should decrease the decay half-life while keeping the other observables at an almost constant value.

This problem, however, intensifies when considering the calculated observables of ^{222}Ra. A mere reduction of the potential depth may not be sufficient in this case, and, similar as was the case with Plutonium, more than one potential parameter may have to be adjusted in order to accurately calculate all structure observables, but this is not within the scope of this work.

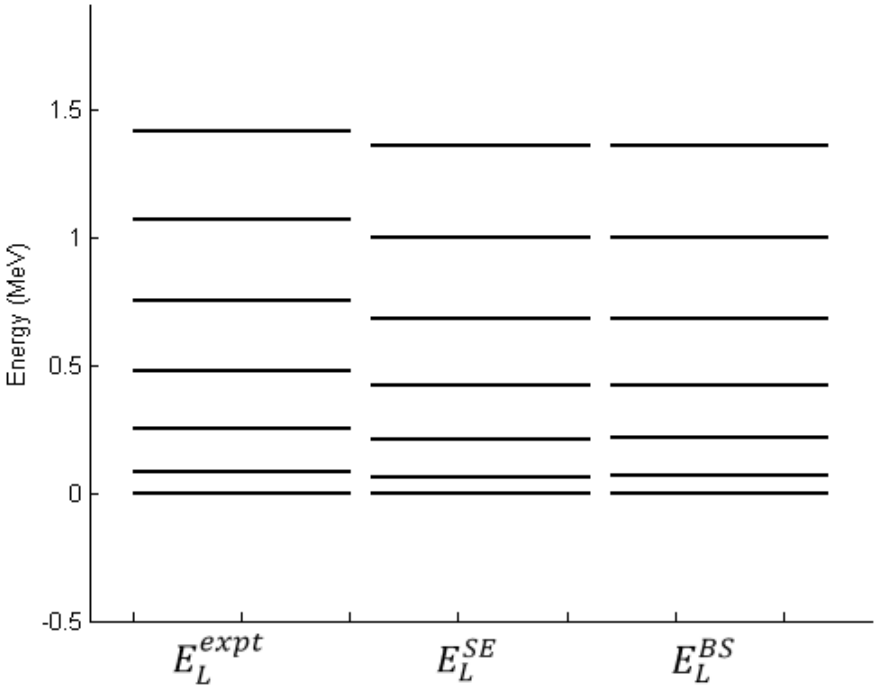

Figure 8.4: Weighted energy levels calculated for ^{224}Ra by solving the SE and BS Rule. All values are measured in MeV.

Chapter 9

Conclusion

The Binary Cluster Model, along with a Woods-Saxon and cubic Woods-Saxon nuclear potential, has been used to study the exotic decay of actinide nuclei.

In the past, the probability for a certain core-cluster pair to form in a nucleus was taken as $P = 1$, which created difficulty in explaining how certain nuclei can decay via the emission of multiple clusters. In this work, a method was introduced to establish a mean cluster charge which satisfies the dipole constraint, resulting in a nucleus consisting of a mixture of up to four core-cluster pairs, each with an associated probability, which ensures the satisfaction of the dipole constraint.

In order to find these core-cluster pairs, the cluster charge which maximizes the expression $D(1,2) = [B_A(1) - B_L(1)] + [B_A(2) - B_L(2)]$ is found, by determining the difference between the actual binding energy and the binding energy obtained from a liquid-drop formula. Only even-even nuclei were considered, since it is assumed the nucleus will prefer an arrangement of the most tightly bound nuclei, and even-even nuclei are more tightly bound than others.

Once the core-cluster decompositions have been obtained, the exotic decay half-life for each cluster could be determined. A summary of these results is shown in table (9.1). Of all the nuclei investigated, only one experimentally observed cluster was not predicted in the model: the ^{28}Mg decay of ^{238}Pu. Furthermore, just more than half of the calculated half-lives are within a factor 3 of the experimental half-life, which is considered a good approximation.

This is rather remarkable, since the decay half-life is particularly sensitive to the choice of parameters. The parameters used for all calculations were determined from a best-fit to exotic decay data of Thorium isotopes, and extended to investigate the exotic decay of Uranium, Plutonium and Radium isotopes.

Of all these nuclei, the choice of parameters only failed to reproduce decay data for Radium, as well as the cluster decay of O. The cluster decay of ^{20}O, however, has been a problem in the past as well, producing a difference by a factor of ~ 10. The inaccuracy of the exotic decay data of Radium, however,

indicates a shortcoming in the potential parameters, and sets a bound on the region where the particular choice of parameters are valid.

Table 9.1: Summary of Exotic Decay Half-Lives of all experimentally observed decays. All considered actinide nuclei are shown, with the emitted cluster, and whether or not the model predicted this cluster. Should the calculated half-life be within a factor 3 of the experimental half-life, it is considered as a good approximation.

Nucleus	Cluster	Observed	Factor ~ 3	$T_{1/2}^{calc}$[y]	$T_{1/2}^{expt}$[y]
^{222}Ra	^{14}C	√		6594.2	105.7
^{224}Ra	^{14}C	√		2.2708×10^{9}	2.507×10^{8}
^{226}Th	^{18}O	√		2.1963×10^{11}	1.818×10^{9}
^{228}Th	^{20}O	√		2.4022×10^{14}	1.692×10^{13}
^{230}Th	^{24}Ne	√	√	1.3348×10^{17}	1.300×10^{17}
^{232}Th	^{24}Ne	√		6.5378×10^{22}	5.06×10^{21}
^{232}Th	^{26}Ne	√	√	4.8676×10^{21}	5.06×10^{21}
^{230}U	^{24}Ne	√	√	2.0551×10^{14}	5.699×10^{14}
^{232}U	^{24}Ne	√	√	1.3733×10^{13}	7.742×10^{12}
^{234}U	^{24}Ne	√		4.8657×10^{19}	2.728×10^{18}
^{234}U	^{26}Ne	√	√	4.2952×10^{18}	2.728×10^{18}
^{234}U	^{28}Mg	√	√	1.5783×10^{18}	1.754×10^{18}
^{236}Pu	^{28}Mg	√	√	1.1442×10^{14}	1.429×10^{14}
^{238}Pu	^{28}Mg				1.463×10^{18}
^{238}Pu	^{30}Mg	√	√	2.5147×10^{18}	1.463×10^{18}
^{238}Pu	^{32}Si	√		4.4613×10^{18}	6.271×10^{17}
^{240}Pu	^{34}Si	√	√	1.4090×10^{19}	5.047×10^{18}

Other than the exotic decay half-life, further structure observables, such as $B(E2)$ transitions between low-lying states, and energy spectra, were also calculated and compared to experimental data. A summary of these results is shown in table (9.2). Only the $B(E2; 2^+ \rightarrow 0^+)$ transition strength is shown, since experimental data for this transition is abundant.

Since the radius parameter of the potential is fitted to the Q-value of the ground state, the ground state energy will be inherently correct. Should the highest known energy level then also be correct, all states in-between are assumed to be approximately correct. For this reason, only the highest known energy state is shown in table (9.2)

The energy spectrum can be solved in two ways; by solving the Schrödinger Equation (SE) numerically, or by solving the Bohr-Sommerfeld (BS) Rule. Both results are listed, and it is interesting to note how little they differ, even though the BS Rule is a semi-classical approximation to solving the SE.

Apart from the energy level for $^{238,240}Pu$, all other energy levels are a very good approximation of the experimental data. This may be an indication, once more, of the limits to which the particular set of parameters can be applied. Considering the results obtained from all nuclei investigated, the ideal nuclear mass for applying the set of parameters chosen seem to be in the range $A = 226 - 236$.

This statement is confirmed when investigating the $B(E2)$ values. Except for $^{238,240}Pu$, all calculated $B(E2)$ are very good approximations of the experimental values. It is also interesting to note how the $B(E2)$ transition strengths increase with increasing isotope mass. This is due to the dependence of the $B(E2)$ values on the cluster charge, and the fact that heavier isotopes tend to have heavier clusters. The transition probability therefore increases for heavier nuclei, and the relative strength, compared to a single-particle transition, becomes increasingly larger.

Table 9.2: Summary of $B(E2)$ and energy levels for Actinide Nuclei. The $B(E2)$ values are shown in Weisskopf units, while the energy levels are shown in MeV.

Nucleus	$B(E2)^{expt}$	$B(E2)^{calc}$	E_L^*	E_L^{expt}	E_L^{SE}	E_L^{BS}
^{222}Ra	111	80	E_{20}^*	3.288	3.363	3.357
^{224}Ra	97	96	E_{12}^*	1.414	1.358	1.357
^{222}Th	74 ± 7	49	E_{26}^*	5.098	4.894	4.880
^{224}Th	96 ± 7	92	E_{18}^*	2.864	2.637	2.632
^{226}Th	164 ± 10	145	E_{20}^*	3.097	2.847	2.842
^{228}Th	167 ± 6	172	E_{18}^*	2.408	2.296	2.294
^{230}Th	196 ± 8	206	E_{24}^*	3.819	3.590	3.586
^{232}Th	198 ± 11	219	E_{30}^*	5.164	5.078	5.069
^{230}U	222	213	E_{22}^*	3.243	3.013	3.010
^{232}U	241	231	E_{20}^*	2.660	2.507	2.512
^{234}U	236	251	E_{30}^*	4.807	4.958	4.953
^{236}Pu	-	314	E_{16}^*	1.786	1.512	1.512
^{238}Pu	285	347	E_{26}^*	4.265	3.441	3.436
^{240}Pu	287	393	E_{32}^*	5.819	4.760	4.756

In conclusion, this work has established a very successful method of predicting the most likely exotic cluster structure which exists in actinide nuclei. By applying a simple cluster model, such as the BCM, and by using a parameterized potential, with a single choice of parameters, a wide variety of nuclei can be described in terms of exotic decay half-lives, reduced transition probabilities and energy spectra.

Appendix A

The different values of $\hbar$

Planck's constant, $\hbar$, is a value which is commonly used throughout quantum mechanics. In different equations, however, this constant needs to have different units. The more common values that $\hbar$ has, are

$$\hbar = 1.055 \times 10^{-34} J \cdot s$$

and

$$\hbar = 6.582 \times 10^{-22} MeV \cdot s$$

In the Bohr-Sommerfeld Rule,

$$\int_{r_1}^{r_2} \sqrt{\frac{\hbar^2}{2\mu}(Q - V(r))}dr = (G - L + 1)\frac{\pi}{2}$$

the value of $\hbar^2$ needs to have units of $amu \cdot MeV \cdot fm^2$.

In order to obtain such units, it is useful to remember that $\hbar$ is a unit of angular momentum,

$$\begin{aligned} angular \quad momentum &= mass \times velocity \times distance \\ (angular \quad momentum)^2 &= (mass)^2 \times (velocity)^2 \times (distance)^2 \\ &= mass \times \left(mass \times velocity^2\right) \times (distance)^2 \\ &= mass \times energy \times (distance)^2 \\ &= kg \times Joule \times m^2 \end{aligned}$$

which, when put into the value of $\hbar^2$,

$$\begin{aligned} \hbar^2 &= \left(1.0546 \times 10^{-34}\right)^2 kg \cdot J \cdot m^2 \\ &= \left(1.0546 \times 10^{-34}\right)^2 \frac{kg \cdot J \cdot m^2}{amu \cdot MeV \cdot fm^2} \times amu \cdot MeV \cdot fm^2 \\ &= \frac{\left(1.0546 \times 10^{-34}\right)^2}{1.6605 \times 10^{-27} \times 1.6022 \times 10^{-13} \times 10^{-30}} amu \cdot MeV \cdot fm^2 \\ &= 0.41804 \times 10^2 \quad amu \cdot MeV \cdot fm^2 \end{aligned}$$

gives the correct units needed for $\hbar$, and also the value used in calculations.

Bibliography

[1] Greiner, W., *Rom. Rep. Phys.* **59**, 193 (2007).

[2] Rose, H.J. and Jones, G.A., *Nature* **307**, 245 (1984).

[3] Bonetti, R. and Guglielmetti, A., *Rom. Rep. Phys.* **59**, 301 (2007).

[4] Maruhn, J. and Greiner, W., *Z. Physik* **251**, 431 (1972).

[5] Fink, H.J., Maruhn, J., Scheid, W. and Greiner, W., *Z. Physik* **268**, 321 (1974).

[6] Beck, C., *Lecture Notes in Physics 818: Clusters in Nuclei, Volume 1* (Springer, 2010).

[7] Poenaru, D.N., Nagame, Y., Gherghescu, R.A. and Greiner, W., *Phys. Rev.* **C65**, 054308 (2002).

[8] Wildermuth, K. and Kanellopoulos, T., *Nucl. Phys.* **7**, 150 (1958).

[9] Sheline, R.K. and Wildermuth, K., *Nucl. Phys.* **21**, 196 (1960).

[10] Buck, B., Dover, C.B. and Vary, J.P., *Phys. Rev.* **C11**, 1803 (1975).

[11] Buck, B., Merchant, A.C. and Perez, S.M., *Phys. Rev.* **C45**, 2247 (1992).

[12] Langer, R.E., *Phys. Rev.* **51**, 669 (1937).

[13] Sun, H., *Bull. Korean Chem. Soc.* **33**, 818 (2012).

[14] Buck, B., Merchant, A.C. and Perez, S.M., *Nucl. Phys.* **A614**, 129 (1997).

[15] Buck, B., Merchant, A.C. and Perez, S.M., *Phys. Rev. Lett.* **65**, 2975 (1990).

[16] Buck, B., Merchant, A.C. and Perez, S.M., *Phys. Rev. Lett.* **72**, 1326 (1994).

[17] Buck, B., Merchant, A.C., Perez, S.M. and Tripe, P., *Phys. Rev.* **C47**, 1307 (1993).

[18] Buck, B., Merchant, A.C., Perez, S.M. and Tripe, P., *J. Phys. G* **20**, 351 (1994).

[19] Buck, B., Merchant, A.C. and Perez, S.M., *Phys. Rev.* **C51**, 559 (1995).

[20] Buck, B., Johnston, J.C., Merchant, A.C. and Perez, S.M., *Phys. Rev.* **C52**, 1840 (1995).

[21] Buck, B., Johnston, J.C., Merchant, A.C. and Perez, S.M., *Phys. Rev.* **C53**, 2841 (1996).

[22] Buck, B., Merchant, A.C. and Perez, S.M., *Phys. Rev. Lett.* **76**, 380 (1996).

[23] Buck, B., Merchant, A.C., Perez, S.M. and Seals, H.E., *J. Phys. G.* **31**, 1499 (2005).

[24] Zettili, N. *Quantum Mechanics: Concepts and Applications* (John Wiley and Sons, 2001).

[25] Griffiths, D.J., *Introduction to Quantum Mechanics* (Prentice Hall, 1995).

[26] Ibrahim, T.T., Ph.D. Thesis, Stellenbosch University, 2009 (unpublished).

[27] Wong, S.M., *Introductory Nuclear Physics* (Prentice Hall, 1990).

[28] Alder, K. and Steffen, R.M., *The Electromagnetic Interaction in Nuclear Spectroscopy*, ed. Hamilton, W.D. (North-Holland, 1975).

[29] Buck, B., Merchant, A.C., Horner, M.J. and Perez, S.M., *Phys. Rev.* **C61**, 024314 (2000).

[30] Zare, R.N., *Angular Momentum: Understanding Spatial Aspects in Chemistry and Physics* (John Wiley and Sons, 1988).

[31] Brink, D.M. and Satchler, G.R., *Angular Momentum* 2^{nd} *ed.* (Clarendon Press, 1968).

[32] Gamow, G., *Z. Phys.* **51**, 204 (1928).

[33] Gurvitz, S.A., *Phys. Rev.* **A38**, 1747 (1988).

[34] Gurvitz, S.A. and Kalbermann, G., *Phys. Rev. Lett.* **59**, 262 (1987).

[35] Goldberger, M.L. and Watson, K.M., *Collision Theory* (John Wiley and Sons, 1964).

[36] Buck, B., Merchant, A.C. and Perez, S.M., *Phys. Rev.* **C58**, 2049 (1998).

[37] Buck, B., Merchant, A.C. and Perez, S.M., *Phys. Rev.* **C59**, 750 (1999).

[38] Buck, B., Merchant, A.C. and Perez, S.M., *Nucl. Phys.* **A617**, 195 (1997).

[39] Buck, B., Merchant, A.C. and Perez, S.M., *Few-Body Systems* **29**, 53 (2000).

[40] Takada, K., *Internet Seminar: Microscopic World -3-, The World of the Atomic Nucleus*, Website: http://www.kutl.kyushu-u.ac.jp

[41] Martin, B.R., *Nuclear and Particle Physics: An Introduction* (John Wiley and Sons, 2006)

[42] Akovali, Y.A., *Nucl. Data Sheets* **77**, 271 (1996).

[43] Artna-Cohen, A., *Nucl. Data Sheets* **80**, 227 (1997).

[44] Audi, G., Bersillon, O., Blachet, J. and Wapstro, A.H., *Nucl. Phys.* **A729**, 3 (2003).

[45] Akovali, Y.A., *Nucl. Data Sheets* **77**, 433 (1996).

[46] Artna-Cohen, A., *Nucl. Data Sheets* **80**, 723 (1997).

[47] Browne, E. and Tuli, J.K., *Nucl. Data Sheets* **113**, 2113 (2012).

[48] Browne, E., *Nucl. Data Sheets* **107**, 2579 (2006).

[49] Browne, E. and Tuli, J.K., *Nucl. Data Sheets* **108**, 681 (2007).

[50] Browne, E. and Tuli, J.K., *Nucl. Data Sheets* **107**, 2649 (2006).

[51] Chukreev, F.E., Makarenko, V.E. and Martin, M.J., *Nucl. Data Sheets* **97**, 129 (2002).

[52] Singh, B., Browne, E., *Nucl. Data Sheets* **109**, 2439 (2008).